

ABSTRACT

Pion, Kaon, Proton and Antiproton Spectra in d+Au and p+p Collisions
at $\sqrt{s_{NN}} = 200\text{GeV}$ at the Relativistic Heavy Ion Collider

Lijuan Ruan

University of Science and Technology of China

Jan. 2005

Identified mid-rapidity particle spectra of π^\pm , K^\pm , and $p(\bar{p})$ from 200 GeV p+p and d+Au collisions are reported. The d+Au collisions were divided into 3 centralities. This data were taken in 2003 run from the Solenoidal Tracker at RHIC (STAR) experiment. A time-of-flight detector based on multi-gap resistive plate chamber (MRPC) technology is used for particle identification. This is the first time that MRPC detector was installed to take data as a time-of-flight detector in the collider experiment.

The calibration method was set up in the STAR experiment for the first time, which will be described in the analysis chapter in detail and has been applied to the experimental data successfully. The intrinsic timing resolution 85 ps was achieved after the calibration. In 2003 run, the pion/kaon can be separated up to transverse momentum (p_T) 1.6 GeV/c while proton can be identified up to 3.0 GeV/c. Thus the identified particle spectra can be extended to intermediate p_T in STAR. This proved that MRPC as a time-of-flight detector works in the heavy ion collider experiment.

We observe that the spectra of π^\pm , K^\pm , p and \bar{p} are considerably harder in d+Au than those in p+p collisions. In $\sqrt{s_{NN}} = 200$ GeV d+Au collisions, the nuclear modification factor R_{dAu} of protons rise faster than those of pions and kaons. The R_{dAu} of proton is larger than 1 at intermediate p_T while the proton production follows binary scaling at the same p_T range in 200 GeV Au+Au collisions. These results further prove that the suppression observed in Au+Au collisions at intermediate and high p_T is due to final state interactions in a dense and dissipative medium produced

during the collision and not due to the initial state wave function of the Au nucleus. Since the initial state in d+Au collisions is similar to that in Au+Au collisions, and, it's believed that the quark-gluon plasma doesn't exist in d+Au collisions, these results from d+Au collisions are very important for us to judge whether the quark-gluon plasma exists in Au+Au collisions or not and to understand the property of the dense matter created in Au+Au collisions. Besides, the particle-species dependence of the Cronin effect is observed to be significantly smaller than that at lower energies. The ratio of the nuclear modification factor (R_{dAu}) between $(p + \bar{p})$ and charged hadrons (h) in the transverse momentum range $1.2 < p_T < 3.0$ GeV/c is measured to be $1.19 \pm 0.05(\text{stat}) \pm 0.03(\text{syst})$ in minimum-bias collisions and shows little centrality dependence. The yield ratio of $(p + \bar{p})/h$ in minimum-bias d+Au collisions is found to be a factor of 2 lower than that in Au+Au collisions, indicating that the relative baryon enhancement observed in heavy ion collisions at RHIC is due to the final state effects in Au+Au collisions.

The mechanism for Cronin effect is also discussed in this thesis by comparison with the recombination model [92] and with the initial multiple parton scattering model [30], which will be described in the discussion chapter in detail. Usually the Cronin effect has been explained to be the initial state effect only [30]. However, from the comparisons, we conclude that the Cronin effect in $\sqrt{s_{NN}} = 200$ GeV d+Au collisions is not initial state effect only, and that final state effect plays an important role.

These physics results has been at e-Print Archives (nu-ex/0309012) and submitted for publication. The excellent particle identification from the prototype MRPC tray and the important physics from it have provided a solid basis for the STAR full-time-of-flight-system proposal.

Pion, Kaon, Proton and Antiproton Spectra in d+Au and
p+p Collisions
at $\sqrt{s_{NN}}=200\text{GeV}$ at the Relativistic Heavy Ion Collider

A Dissertation
Presented to the Faculty of the Graduate School
of
University of Science and Technology of China
in Candidacy for the Degree of
Doctor of Philosophy

By
Lijuan Ruan

Dissertation Director: Prof. Hongfang Chen
Off-campus Co-adviser: Dr. Zhangbu Xu

Jan. 2005

© Copyright 2018

by

Lijuan Ruan

All Rights Reserved

Acknowledgments

I would like to thank my adviser, Prof. Hongfang Chen. She has been my adviser since I was an undergraduate student. Her enormous physics knowledge and serious attitude on science give me a deep impression. Her enthusiasm on the research sets an example for me. I also thank her for giving me a chance to stay in BNL to do my research on STAR physics. I would like to thank Dr. Zhangbu Xu, the co-adviser of my PhD research. He guided me through all the detailed analysis in my research. He also gave me a lot of help on life when I stayed at BNL.

Special thanks to Xin Dong, my classmate and my friend, a great partner of the research. He gave me a lot of help and encouragement. I would like to thank Dr. Nu Xu and Prof. Huanzhong Huang for many helpful and inspiring discussion on my research. I'd like to thank Prof. Jian Wu for taking care of me and encouraging me when he stayed in BNL. I thank Dr. Haibin Zhang to give me a lot of help on life when I just arrived at BNL. He also guided me through the K^* analysis.

I'd like to thank the high energy group in USTC for their hardwork on the MRPC detector construction. Spectra thanks to Prof. Cheng Li, and Dr. Ming Shao.

I'd like to thank my parents for their sacrifice and support. Without the sacrifice, I will be only the body without spirit. I'd like to thank my husband, Dr. Shengli Huang for his encouragement and support.

I'd like to thank all my friends for their support. Without you, the life is meaningless.

I thank every member of the STAR collaboration for their hard work to make the experiment run smoothly and successfully, to construct the detector and develop the software.

Contents

Acknowledgments	iii
1 Physics	1
1.1 Deconfinement and phase diagram	1
1.2 Relativistic Heavy Ion Collisions	3
1.3 The experimental results at RHIC	4
1.3.1 Flow	4
1.3.2 High p_T suppression and di-hadron azimuthal correlation . . .	6
1.3.3 Particle composition in Au+Au at intermediate p_T	9
1.3.4 Summary	13
1.4 Cronin effect	13
1.4.1 Why we need d+Au run at RHIC	13
1.4.2 Lower energy	14
1.4.3 Predictions: RHIC energy	15
2 The STAR Experiment	17
2.1 The RHIC Accelerator	17
2.2 The STAR Detector	19
2.2.1 The Time Projection Chamber	22
2.2.2 The time-of-flight tray based on MRPC technology	26
3 Analysis Methods	33
3.1 Trigger	33
3.1.1 Centrality tagging	34

3.1.2	Trigger bias study	34
3.2	Track selection and calibration	36
3.2.1	Calibration	37
3.3	Raw yield	41
3.3.1	π raw yield extraction	41
3.3.2	K raw yield extraction	42
3.3.3	p and \bar{p} raw yield extraction	43
3.4	Efficiency and acceptance correction	44
3.5	Background correction	46
3.6	Energy loss correction	47
3.7	Normalization	47
4	Results	58
4.1	π, K, p and \bar{p} spectra in d+Au and p+p collisions at mid-rapidity . .	58
4.1.1	Systematic uncertainty	59
4.2	Cronin effect	59
4.3	$p + \bar{p}/h$ ratio in d+Au and p+p collisions at middle pseudo-rapidity .	61
4.4	$K/\pi, p/\pi$ and anti-particle to particle ratios	63
4.5	$dN/dy, \langle p_T \rangle$, and model fits	65
4.6	System comparison	66
5	Discussion	74
5.1	Cronin effect	74
5.1.1	Model comparison: initial state effect?	75
5.1.2	Model comparison: recombination	76
5.1.3	Integral yield R_{dAu} : shadowing effect?	80
5.1.4	Initial or final state effect: Drell-Yan process	81
5.2	Baryon excess in Au+Au collisions	82
5.2.1	\bar{p}/p ratio vs p_T	83
5.2.2	Baryon production at RHIC: multi-gluon dynamics?	84

6	Conclusion and Outlook	86
6.1	Conclusion	86
6.2	Outlook	88
6.2.1	Cronin effect at 200 GeV: Mass dependent or baryon/meson dependent?	88
6.2.2	Electron PID from MRPC-TOFr	89
6.2.3	Full-TOF Physics	90
6.2.4	63 GeV Au+Au collisions at RHIC	91
A	Tables of the Invariant Yields	92
B	How to make MRPC	99
B.1	Preparations	99
B.1.1	Glass	99
B.1.2	Graphite Layer	99
B.1.3	Mylar layer	100
B.1.4	Honeycomb board	100
B.1.5	The printed circuit board (PCB)	100
B.1.6	Lucite cylinder	100
B.1.7	Other stuff	101
B.2	Installation	101
B.2.1	The outer glass and mylar and PCB	101
B.2.2	Inner glass and fish-line coiling	101
C	List of Publications	103
D	STAR Collaboration	107
	Bibliography	110

List of Figures

1.1	Phase diagram of hadronic and partonic matter. Figure is taken from [3].	2
1.2	A recent Lattice QCD calculation [4] of the pressure, $P(T)/T^4$, and a measure of the deviation from conformality.	
1.3	The minimum-bias (0–80% of the collision cross section) $v_2(p_T)$ for K_S^0 , $\Lambda + \bar{\Lambda}$ and h^\pm . The figure is taken from [5].	
1.4	$R_{AA}(p_T)$ of inclusive charged hadron for various centrality bins. Figure is taken from [6].	
1.5	(a) Azimuthal distribution of particles with respect to a trigger particle for p+p collisions.	
1.6	(left) The π , K, p spectra in 0%-5% and 60%-92% Au+Au 200 GeV collisions from [14].	
1.7	The ratio R_{CP} for identified mesons and baryons at mid-rapidity calculated using centrality dependent v_2 from [15].	
1.8	(left) The power alpha of A dependence from 300 GeV incident proton-fixed target experiment.	
1.9	R_{AB} for minimum bias and central d+Au collisions, and central Au+Au collisions [8]. The figure is taken from [7].	
2.1	A diagram of the Brookhaven National Laboratory collider complex including the accelerators and the collision region.	
2.2	Perspective view of the STAR detector, with a cutaway for viewing inner detector systems.	
2.3	Cutaway side view of the STAR detector as configured in 2001. Figure is taken from [43].	
2.4	The STAR TPC surrounds a beam-beam interaction region at RHIC. The collisions take place at the center of the detector.	
2.5	Beam’s eye view of a central Au+Au collision event in the STAR Time Projection Chamber.	
2.6	The energy loss distribution for primary and secondary particles in the STAR TPC as a function of pseudorapidity.	
2.7	Tray structure. Figure is taken from [74].	26
2.8	Two side views of MRPC. The upper (lower) is for long (short) side view. The two plots show the distribution of read-out strips.	
2.9	The shape of the 6 read-out strips for each MRPC.	28
2.10	Simulated 1st effective Townsend coefficient curve and normalized charge distribution for MRPC.	
2.11	Simulated results of a 6 gap MRPC.	31
3.1	The p_T dependence plot of the trigger bias.	35
3.2	The enhancement factor and $\langle N_{ch} \rangle$ bias in minimum-bias and centrality selected d+Au collisions.	

3.3	pVPD slewing correction.	38
3.4	dE/dx vs p plot from d+Au collisions. The line represents that $dE/dx = 0.028 \times 10^{-4}$ GeV/cm.	39
3.5	The slewing correction.	40
3.6	The z position correction.	41
3.7	The overall timing resolution after the calibration.	42
3.8	$1/\beta$ vs. momentum for π^\pm , K^\pm , and $p(\bar{p})$ from 200 GeV d+Au collisions. Separations between π^\pm and K^\pm	43
3.9	the ratio of \bar{p} at $dca < 1.0$ cm over \bar{p} at $dca < 3.0$ cm.	44
3.10	TPC reconstruction efficiency of π^\pm , K^\pm , p and \bar{p} as a function of p_T . The left plot for charged pions and the right plot for kaons and protons.	45
3.11	Matching efficiency from TOFr to TPC of π^\pm , K^\pm , p and \bar{p} as a function of p_T , including the p and \bar{p} scattering effect.	46
3.12	The TOFr response efficiency as a function of p_T	47
3.13	π background contribution as a function of p_T . The circled symbols represent the total π background.	48
3.14	The p scattering effect contribution when we cut $dca < 1.0$ cm.	48
3.15	(left) p energy loss correction of different particle species as a function of p . p_{rec} is the reconstructed p	49
3.16	π^+ raw yields versus mass squared distribution. The histograms are our data. The curves are fits.	50
3.17	π^- raw yields versus mass squared distribution. The histograms are our data. The curves are fits.	51
3.18	K^+ raw yields versus mass squared distribution. The histograms are our data. The curves are fits.	52
3.19	K^- raw yields versus mass squared distribution. The histograms are our data. The curves are fits.	53
3.20	p raw yields versus mass squared distribution. The histograms are our data. The curves are fits.	54
3.21	\bar{p} raw yields versus mass squared distribution. The histograms are our data. The curves are fits.	55
4.1	The invariant yields of pions (filled circles), kaons (open squares), protons (filled triangles) and antiprotons (open circles) as a function of p_T in minimum-bias, centrality selected d+Au collisions and p+p collisions.	56
4.2	The identified particle R_{dAu} for minimum-bias and top 20% d+Au collisions. The filled triangles are pions, open squares are kaons, filled circles are protons and open circles are antiprotons.	57
4.3	Minimum-bias ratios of $(p + \bar{p})$ over charged hadrons at $-0.5 < \eta < 0.0$ from $\sqrt{s_{NN}} = 200$ GeV d+Au collisions.	58
4.4	Minimum-bias ratios of $(p + \bar{p})$ over charged hadrons at $-0.5 < \eta < 0.0$ from $\sqrt{s_{NN}} = 200$ GeV p+p collisions.	59
4.5	π^-/π^+ , K^-/K^+ and \bar{p}/p ratios as a function of p_T in d+Au and p+p minimum-bias collisions.	60
4.6	K/π ratios as a function of p_T in d+Au and p+p minimum-bias collisions. The open symbols are for pions and the filled symbols are for kaons.	61
4.7	$p(\bar{p})/\pi$ ratios as a function of p_T in d+Au and p+p minimum-bias collisions. The open symbols are for pions and the filled symbols are for protons and antiprotons.	62
4.8	The re-scaled π^+ and π^- spectra in minimum-bias, centrality selected d+Au collisions and p+p collisions.	63
4.9	The re-scaled K^+ and K^- spectra in minimum-bias, centrality selected d+Au collisions and p+p collisions.	64
4.10	The re-scaled p and \bar{p} spectra in minimum-bias, centrality selected d+Au collisions and p+p collisions.	65
4.11	The spectra of π^- , π^+ , K^- , K^+ , \bar{p} and p in d+Au and p+p minimum-bias collisions. The open symbols are for pions and the filled symbols are for kaons, protons and antiprotons.	66

- 4.12 The spectra of π^- , π^+ , K^- , K^+ , \bar{p} and p in three centrality selected d+Au collisions. The
- 4.13 $\langle p_T \rangle$ as a function of $dN/d\eta$. The squared, circled and triangled symbols are from [35] in
- 4.14 K^-/π^- and \bar{p}/π^- as a function of $dN/d\eta$. The circled and triangled symbols are from [35]
- 4.15 The kinetic freeze out temperature T_{kin} (left) and flow velocity $\langle \beta \rangle$ (right) from thermal f
- 5.1 (left) The Cronin effect at different rapidity as a function of p_T . The different curve in ea
- 5.2 (left) The invariant yield for π^+ at 0%-20% d+Au collisions as a function of p_T . The open
- 5.3 (left) The invariant yield for p at 0%-20% d+Au collisions as a function of p_T . The open
- 5.4 Integral yield R_{dAu} as a function of $dN/d\eta$ in minimum-bias and centrality selected d+Au
- 5.5 Integral yield Cronin ratio as a function of atomic weight in p+A fixed target experiment
- 5.6 \bar{p}/p ratio as a function of p_T in d+Au and p+p minimum-bias collisions. The open square
- 5.7 Minimum-bias ratios of $(p + \bar{p})$ over charged hadrons at $-0.5 < \eta < 0.0$ from $\sqrt{s_{NN}} = 200$ C
- 6.1 dE/dx in TPC versus p without(the upper panel) or with (the lower pannel) the TOFr ve

List of Tables

- 3.1 Centrality definitions for different uncorrected FTPC east reference multiplicity ranges. U
- 3.2 Trigger bias study. The $\langle N_{ch} \rangle$ bias and enhancement factor in minimum-bias, centrality se
- 3.3 π^+ raw signal table in minimum-bias, centrality selected d+Au collisions and minimum-bi
- 3.4 π^- raw signal table in minimum-bias, centrality selected d+Au collisions and minimum-bi
- 3.5 K^+ raw signal table in minimum-bias, centrality selected d+Au collisions and minimum-b
- 3.6 K^- raw signal table in minimum-bias, centrality selected d+Au collisions and minimum-b
- 3.7 p raw signal table in minimum-bias, centrality selected d+Au collisions and minimum-bia
- 3.8 \bar{p} raw signal table in minimum-bias, centrality selected d+Au collisions and minimum-bia

- 4.1 $\langle N_{bin} \rangle$ from a Glauber model calculation, $(p + \bar{p})/h$ averaged over the bins within $1.2 < p_T$
- 4.2 π^-/π^+ , K^-/K^+ and \bar{p}/p ratios in p+p and d+Au minimum-bias collisions. Also shows in
- 4.3 $\langle p_T \rangle$ of π^- , π^+ , K^- , K^+ , \bar{p} and p from power law fit in minimum-bias, centrality selected
- 4.4 dN/dy of π^- , π^+ , K^- , K^+ , \bar{p} and p from power law fit in minimum-bias, centrality selecte
- 4.5 The final $\langle p_T \rangle$ of π^- , π^+ , K^- , K^+ , \bar{p} and p in minimum-bias, centrality selected d+Au co
- 4.6 The final dN/dy of π^- , π^+ , K^- , K^+ , \bar{p} and p in minimum-bias, centrality selected d+Au

- A.1 π^+ spectra in minimum-bias and 0-20% d+Au collisions. The unit of p_T and p_T width is c
- A.2 π^+ spectra in 20-40% and 40-100% d+Au collisions. The unit of p_T and p_T width is GeV/c
- A.3 π^+ spectra in p+p collisions. The unit of p_T and p_T width is GeV/c . . 93
- A.4 π^- spectra in minimum-bias and 0-20% d+Au collisions. The unit of p_T and p_T width is c
- A.5 π^- spectra in 20-40% and 40-100% d+Au collisions. The unit of p_T and p_T width is GeV/c
- A.6 π^- spectra in p+p collisions. The unit of p_T and p_T width is GeV/c . . 94
- A.7 K^+ spectra in minimum-bias and 0-20% d+Au collisions. The unit of p_T and p_T width is
- A.8 K^+ spectra in 20-40% and 40-100% d+Au collisions. The unit of p_T and p_T width is GeV/c

- A.9 K^+ spectra in p+p collisions. The unit of p_T and p_T width is GeV/c . 95
- A.10 K^- spectra in minimum-bias and 0-20% d+Au collisions. The unit of p_T and p_T width is GeV/c .
- A.11 K^- spectra in 20-40% and 40-100% d+Au collisions. The unit of p_T and p_T width is GeV/c .
- A.12 K^- spectra in p+p collisions. The unit of p_T and p_T width is GeV/c . 96
- A.13 p spectra in minimum-bias and 0-20% d+Au collisions. The unit of p_T and p_T width is GeV/c .
- A.14 p spectra in 20-40% and 40-100% d+Au collisions. The unit of p_T and p_T width is GeV/c .
- A.15 p spectra in p+p collisions. The unit of p_T and p_T width is GeV/c . . 97
- A.16 \bar{p} spectra in minimum-bias and 0-20% d+Au collisions. The unit of p_T and p_T width is GeV/c .
- A.17 \bar{p} spectra in 20-40% and 40-100% d+Au collisions. The unit of p_T and p_T width is GeV/c .
- A.18 \bar{p} spectra in p+p collisions. The unit of p_T and p_T width is GeV/c . . 98
- B.1 The material for 1 MRPC model. VR is the volume resistivity and SR is the surface resistivity.

Chapter 1

Physics

1.1 Deconfinement and phase diagram

The theory which describes the interaction of the color charges of quarks and gluons is called Quantum Chromodynamics (QCD). In phenomenological quark models, mesons can be described as quark-antiquark bound states, while baryons can be considered as three quark bound states. Up to now, it's found that all the hadron states which can be observed in isolation is colorless singlet states. Experimentally, no single quark, which is described by a color-triplet state, has ever been isolated. The absence of the observation of a single quark in isolation suggests that the interaction between quarks and gluons must be strong on large distance scale. In the other extreme, much insight into the nature of the interaction between quarks and gluons on short distance scales was provided by deep inelastic scattering experiments. In these experiments, the incident electron interacts with a quark within a hadron and is accompanied by the momentum transfer from the electron to the quark. The measurement of the electron momentum before and after the interaction allows a probe of the momentum distribution of the parton inside the nucleon. It was found that with very large momentum transfer, the quarks inside the hadron behave as if they were almost free [1]. The strong coupling between quarks and gluons at large distances and asymptotic freedom are the two remarkable features of QCD. When the energy density is high enough either due to the high temperature or high baryon density,

the quark or gluon may be deconfined from a hadron. The thermalized quark gluon system is what we called quark-gluon plasma. Lattice QCD calculations, considering two light quark flavors, predict a phase transition from a confined phase, hadronic matter, to a deconfined phase, or quark-gluon plasma (QGP), at a temperature of approximately 160 MeV [2]. Figure 1.1 shows the phase diagram of the hadronic and

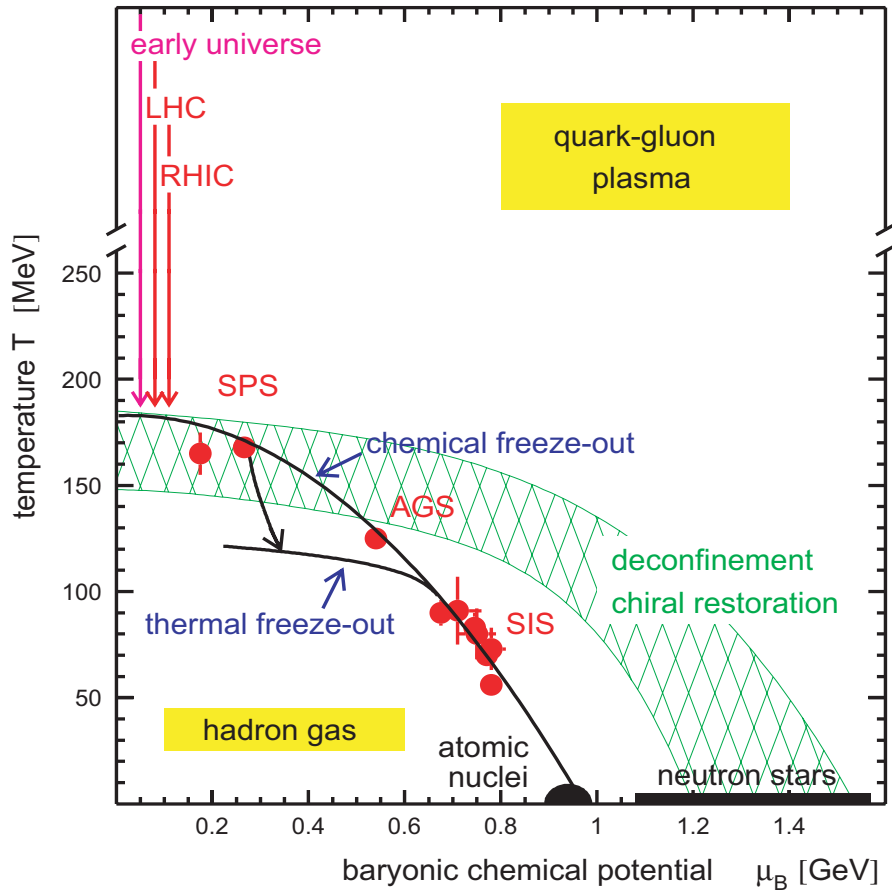


Figure 1.1: Phase diagram of hadronic and partonic matter. Figure is taken from [3].

partonic matter. A phase transition from the confined hadronic matter to the deconfined QGP matter is expected to happen at either high temperature or large baryon chemical potential μ_B . Recent Lattice QCD calculations show that the QGP is far from ideal below $3 T_c$. The nonideal nature of this strongly coupled QGP is also seen from the deviation of the pressure, $P(T)$, and energy density $\epsilon(T)$ from the Stefan Boltzmann limit as shown in Figure from [4]. Experiments on relativistic heavy ion

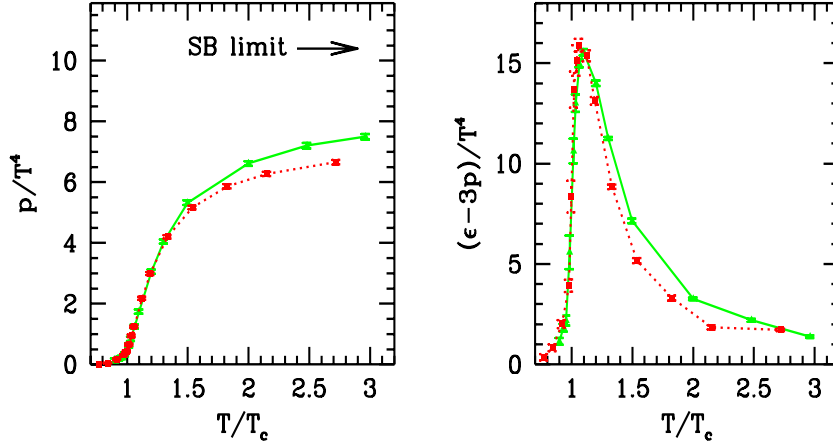


Figure 1.2: A recent Lattice QCD calculation [4] of the pressure, $P(T)/T^4$, and a measure of the deviation from the ideal Stefan-Boltzmann limit $(\epsilon(T) - 3P(T))/T^4$.

collisions are designed to search for and study the deconfined QGP matter.

1.2 Relativistic Heavy Ion Collisions

The experimental programs in relativistic heavy ions started in 1986 using the Alternating Gradient Synchrotron (AGS) at Brookhaven National Lab (BNL) and the Super Proton Synchrotron (SPS) at European laboratory for particle physics (CERN). At BNL, ion beams of silicon and gold, accelerated to momenta of 14 and 11 GeV/c per nucleon, respectively, have been utilized in 10 fixed-target experiments. There have been 15 heavy ion experiments at CERN utilizing beams of oxygen at 60 and 200 GeV/c per nucleon, sulphur at 200 GeV/c per nucleon and Pb at 160 GeV/c per nucleon [2].

The Relativistic Heavy Ion Collider (RHIC) at BNL is designed for head-on Au+Au collisions at $\sqrt{s_{NN}} = 200$ GeV. The first RHIC run was performed in 2000 with Au+Au collisions at $\sqrt{s_{NN}} = 130$ GeV/c in four experiments, STAR, PHENIX, PHOBOS and BRAHMS. The second RHIC run was in 2001 and 2002 with Au+Au and p+p collisions at $\sqrt{s_{NN}} = 200$ GeV. The third RHIC run was in 2002 and 2003 with

d+Au and p+p collisions at $\sqrt{s_{NN}} = 200$ GeV.

The above mentioned relativistic heavy ion collision experiments are designed for the search and study of the possible deconfined high energy density matter, quark-gluon plasma. In head-on relativistic heavy ion collisions, two nuclei can be represented as two thin disks approaching each other at high speed because of the Lorentz contraction effect in the moving direction. During the initial stage of the collisions, the energy density is higher than the critical energy density from the Lattice QCD calculation, so the quarks and gluons will be de-confined from nucleons and form the quarks and gluons system. The large cross section of interaction may lead to the thermalization of the quarks and gluons system. That's what we called the formation of quark-gluon plasma (QGP). In this stage, the high transverse momentum (p_T) jets and $c\bar{c}$ pair will be produced due to the large momentum transfer. After that, the QGP will expand and cool down and enter into the mixed-phase expansion. The chemical freeze out point will be formed after the inelastic interactions stop. That means that the particle yields and ratios will not change. After the chemical freeze out, the elastic interactions between hadrons will change the p_T distribution of particles. The particles will freeze out finally from the system after the elastic interactions stop. That's what we called the kinetic freeze out point. In the following the important results from RHIC will be addressed.

1.3 The experimental results at RHIC

1.3.1 Flow

In non-central Au+Au collisions, the spatial space asymmetry will be transferred into the momentum space asymmetry by the azimuthal asymmetry of pressure gradients. The azimuthal particle distributions in momentum space can be expanded in a form of Fourier series

$$E \frac{d^3 N}{d^3 p} = \frac{1}{2\pi} \frac{d^2 N}{p_T dp_T dy} \left(1 + \sum_{n=1}^{\infty} 2v_n \cos[n(\phi - \Psi_r)] \right) \quad (1.1)$$

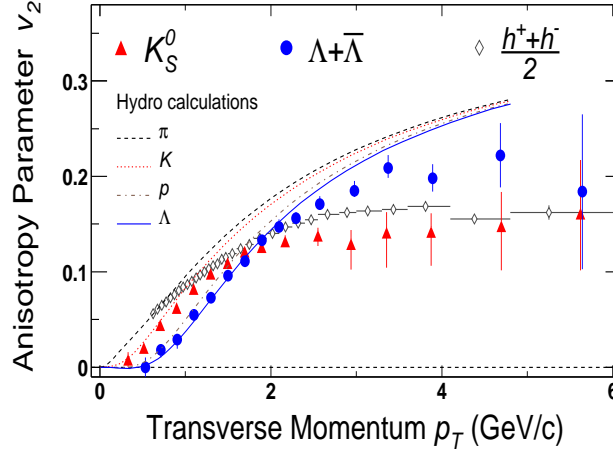


Figure 1.3: The minimum-bias (0–80% of the collision cross section) $v_2(p_T)$ for K_S^0 , $\Lambda + \bar{\Lambda}$ and h^\pm . The error bars shown include statistical and point-to-point systematic uncertainties from the background. The additional non-flow systematic uncertainties are approximately -20%. Hydrodynamical calculations of v_2 for pions, kaons, protons and lambdas are also plotted [5]. Figure is taken from [6].

where Ψ_r denotes the reaction plane angle. The Fourier expansion coefficient v_n stands for the n th harmonic of the event azimuthal anisotropies. v_1 is so called direct flow and v_2 is the elliptic flow. The elliptic flow is generated mainly during the highest density phase of the evolution before the initial geometry asymmetry of the plasma disappears. Hydrodynamical calculations [19] show most of v_2 is produced before 3 fm/c at RHIC.

Figure 1.3 shows that The v_2 of K_S^0 , $\Lambda + \bar{\Lambda}$ and charged hadrons (h^\pm) as a function of p_T for 0–80% of the collision cross section [6]. Also shown are the v_2 of pions, kaons, protons and lambdas from hydrodynamical model [5]. The v_2 from hydrodynamical model shows strong mass dependence, which fits the K_S^0 v_2 up to $p_T \sim 1$ GeV/c and fits the $\Lambda + \bar{\Lambda}$ v_2 up to $p_T \sim 2.5$ GeV/c. Even though the v_2 from hydrodynamical model shows consistency with data at low p_T , however, the v_2 from experimental results show saturation at intermediate p_T while hydrodynamical predictions show rising trend at the same p_T range.

1.3.2 High p_T suppression and di-hadron azimuthal correlation

The v_2 from hydrodynamical models show consistency with data at lower p_T and fail to reproduce data at higher p_T . At high p_T , the suppression for charged hadron production was observed in Au+Au collisions at RHIC energy. The comparison of the spectra in Au+Au collisions through those in p+p collisions, scaled by the number of binary nucleon nucleon collisions is the nuclear modification factor R_{AA} .

$$R_{AA}(p_T) = \frac{d^2 N^{AA}/dp_T d\eta}{T_{AA} d^2 \sigma^{NN}/dp_T d\eta} \quad (1.2)$$

where $T_{AA} = \langle N_{\text{bin}} \rangle / \sigma_{\text{inel}}^{NN}$ accounts for the collision geometry, averaged over the event centrality class. $\langle N_{\text{bin}} \rangle$, the equivalent number of binary NN collisions, is calculated using a Glauber model. The R_{AA} is an experimental variable. The high p_T hadron suppression in central Au+Au collisions can also be investigated by comparing the hadron spectra in central and peripheral Au+Au collisions. That's what we called R_{CP} . R_{CP} is defined as

$$R_{CP} = \frac{\langle N_{\text{bin}}^{\text{peripheral}} \rangle d^2 N^{\text{central}}/dp_T d\eta}{\langle N_{\text{bin}}^{\text{central}} \rangle d^2 N^{\text{peripheral}}/dp_T d\eta}. \quad (1.3)$$

Figure 1.4 shows $R_{AA}(p_T)$ of inclusive charged hadron for various centrality bins in Au+Au collisions at $\sqrt{s_{NN}}=200$ GeV. $R_{AA}(p_T)$ increases monotonically for $p_T < 2$ GeV/c at all centralities and saturates near unity for $p_T > 2$ GeV/c in the most peripheral bins. In contrast, $R_{AA}(p_T)$ for the central bins reaches a maximum and then decreases strongly above $p_T = 2$ GeV/c, showing the suppression of the charged hadron yield relative the NN reference [8].

Suppression of high p_T hadron production in central Au+Au collisions relative to p+p collisions [8, 17] has been interpreted as energy loss of the energetic partons traversing the produced hot and dense medium [9], that's so called jet quenching. If a dense partonic matter is formed during the initial stage of a heavy-ion collision with a large volume and a long life time (relative to the confinement scale $1/\Lambda_{\text{QCD}}$), the

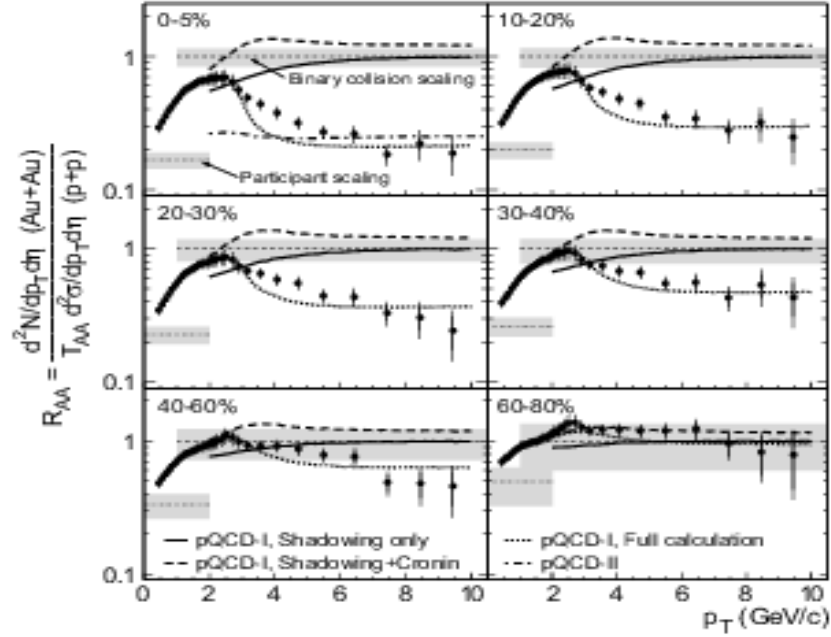


Figure 1.4: $R_{AA}(p_T)$ of inclusive charged hadron for various centrality bins. Figure is taken from [8].

produced large E_T parton will interact with this dense medium and will lose its energy via induced radiation. The energy loss depends on the parton density of the medium. Therefore, the study of parton energy loss can shed light on the properties of the dense matter in the early stage of heavy-ion collisions [9]. At sufficiently high beam energy, gluon saturation is also expected to result in a relative suppression of hadron yield at high p_T in A+A collisions [33]. Also shown in the Figure 1.4 are the results from perturbative QCD (pQCD) calculations. The Full-pQCD calculations include the partonic energy loss, the Cronin enhancement (due to initial multiple scattering) and the nuclear shadowing effect. The suppression is predicted to be p_T independent when p_T is larger than 6 GeV/c, which is consistent with our data. However, the discrepancy at 2-6 GeV/c was observed between the prediction and the experimental data. This discrepancy may be due to different mechanism for particle production at intermediate p_T . The particle production at intermediate p_T will be discussed later in this chapter.

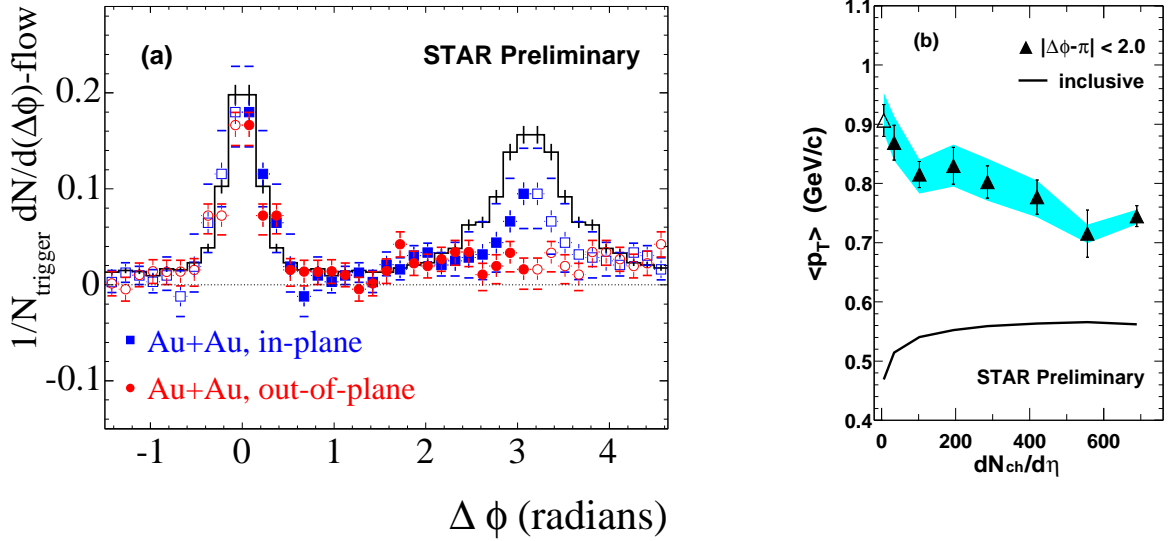


Figure 1.5: (a) Azimuthal distribution of particles with respect to a trigger particle for p+p collisions (solid line), and mid-central Au+Au collisions within the reaction plane (squares) and out-of-plane (circles) at 200 GeV [10]. (b) Mean transverse momentum for particles around the away-side region as a function of number of charged particles [11]. The solid line shows the mean transverse momentum of inclusive hadrons.

A more differential probe of parton energy loss is the measurement of high p_T di-hadron azimuthal correlation relative to the reaction plane orientation. The trigger hadron is in the range $4 < p_T < 6$ GeV/c and the associated particle is at $2 < p_T < 4$ GeV/c. Figure 1.5 (left) shows the high p_T di-hadron correlation when the trigger particle is selected in the azimuthal quadrants centered either in the reaction plane (in plane) or orthogonal to it (out of plane). The near side di-hadron azimuthal correlations in both cases were observed to be the same as that in p+p collisions, while the suppression of back to back correlation shows strong dependence on the relative angle between the triggered high p_T hadron and the reaction plane. This systematic dependence is consistent with the picture of parton energy loss: the path length for a dijet oriented out of plane is longer than that for a dijet oriented in plane, leading to a stronger suppression of parton energy loss in the out of plane. The dependence of parton energy loss on the path length is predicted to be substantially larger than linear [9].

The energy lost by away side partons traversing the collision matter must in the form

of the excess of softer emerging particles due to the transverse momentum conservation. An analysis of azimuthal correlations between soft and hard particles has been performed for both 200 GeV p+p and Au+Au collisions [11] at STAR as a first of attempt to trace the degree of the degradation on the away side. With triggered hadron still in the range $4 < p_T^{trig} < 6$ GeV/c, but the associated hadrons now sought over $0.15 < p_T < 4$ GeV/c, combinatorial coincidences dominate this correlation and they must be subtracted carefully by mixed-event technique and also the elliptic flow effect was also subtracted by hand [11]. The results demonstrate that, in comparison with the p+p and peripheral Au+Au collisions, the momentum-balancing hadrons opposite to the high p_T triggered particle in central Au+Au are greater in number, much more widely dispersed in azimuthal angle, and significantly softer in momentum. Figure 1.5 (right) shows the $\langle p_T \rangle$ of the momentum-balancing hadrons opposite to the high p_T trigger as a function of centrality. The $\langle p_T \rangle$ were observed to decrease from peripheral to central Au+Au collisions. Also shown in the Figure 1.5 (right) is the $\langle p_T \rangle$ of the inclusive hadrons as a function of centrality. This study will be extended to higher p_T trigger particle. The results may suggest that the moderately hard parton traversing a significant path length through the collision matter makes substantial progress toward equilibrium with the bulk. The rapid attainment of thermalization via multitude of softer parton-parton interactions in the earliest collision stages would then not be so surprising [13].

1.3.3 Particle composition in Au+Au at intermediate p_T

As we have mentioned above, for R_{AA} , the pQCD model including the parton energy loss, Cronin enhancement and nuclear shadowing can qualitatively fit the trend of data at $2 < p_T < 6$ GeV/c, however, the quantitative discrepancy between the model and the data is also obvious. In the intermediate p_T , the mechanism for particle production may be different from that at high p_T .

Figure 1.6 (left) shows the π , K, p spectra in 0%-5% and 60%-92% Au+Au 200 GeV collisions from [14]. It shows that the shapes of the spectra show clear mass dependence. And in central collisions, the π , K, p yields are close to each other at $p_T > 2$

GeV/c while it's not the case in peripheral collisions. Figure 1.6 (right) shows proton/pion (top) and anti-proton/pion (bottom) ratios for central 0–10%, mid-central 20–30% and peripheral 60–92% in Au+Au collisions at 200 GeV [14]. It shows that the $p(\bar{p})/\pi$ ratios increase fast from peripheral to central collisions. In the 0-10% centrality bin, the proton yield is even larger than pion yield at intermediate p_T . Figure 1.7 shows the ratio R_{CP} for identified mesons and baryons at mid-rapidity calculated using centrality intervals, 0–5% vs. 40–60% of the collision cross section from STAR measurement [12]. It seems that for meson, the R_{CP} follows a common trend and for baryon, the R_{CP} also follows a common trend, which is different from that for mesons. The R_{CP} for baryons is observed to be larger than that for mesons.

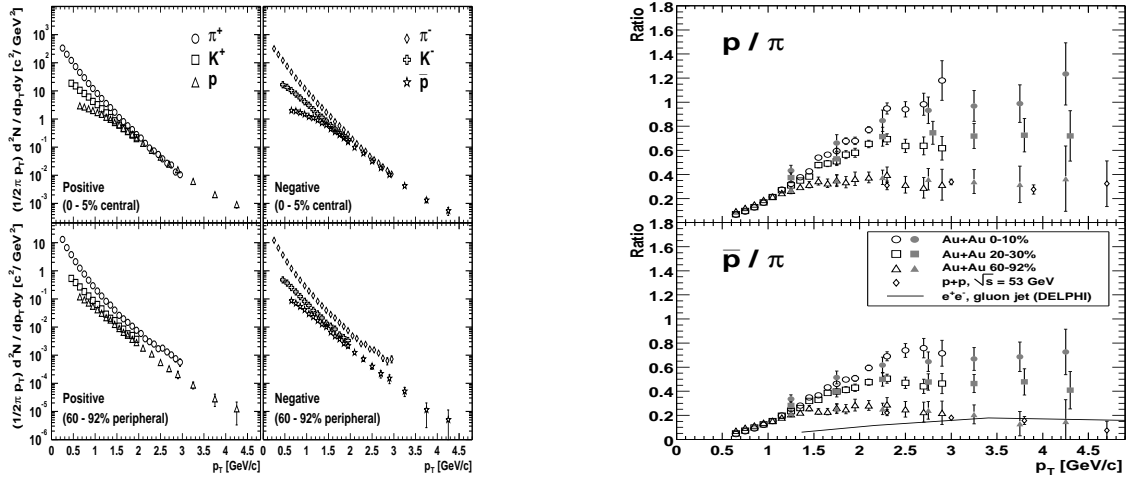


Figure 1.6: (left) The π , K , p spectra in 0%–5% and 60%–92% Au+Au 200 GeV collisions from [14]. (right) Proton/pion (top) and anti-proton/pion (bottom) ratios for central 0–10%, mid-central 20–30% and peripheral 60–92% in Au+Au collisions at 200 GeV. Open (filled) points are for charged (neutral) pions. The data at $\sqrt{s} = 53$ GeV p+p collisions [15] are also shown. The solid line is the $(\bar{p} + p)/(\pi^+ + \pi^-)$ ratio measured in gluon jets [16]. This figure is from [14].

These experimental results suggest that the degree of suppression depends on particle species (baryon/meson) at intermediate p_T . The spectra of baryons (protons and lambdas) are less suppressed than those of mesons (pions, kaons) [6, 18] in the

p_T range $2 < p_T < 5$ GeV/c. The baryon content in the hadrons at intermediate p_T depends strongly on the impact parameter (centrality) of the Au+Au collisions with about 40% of the hadrons being baryons in the minimum-bias collisions and 20% in very peripheral collisions [6, 18]. Hydrodynamics [19, 20], parton coalescence at hadronization [21, 22, 23] and gluon junctions [24] have been suggested as explanations for the observed particle-species dependence.

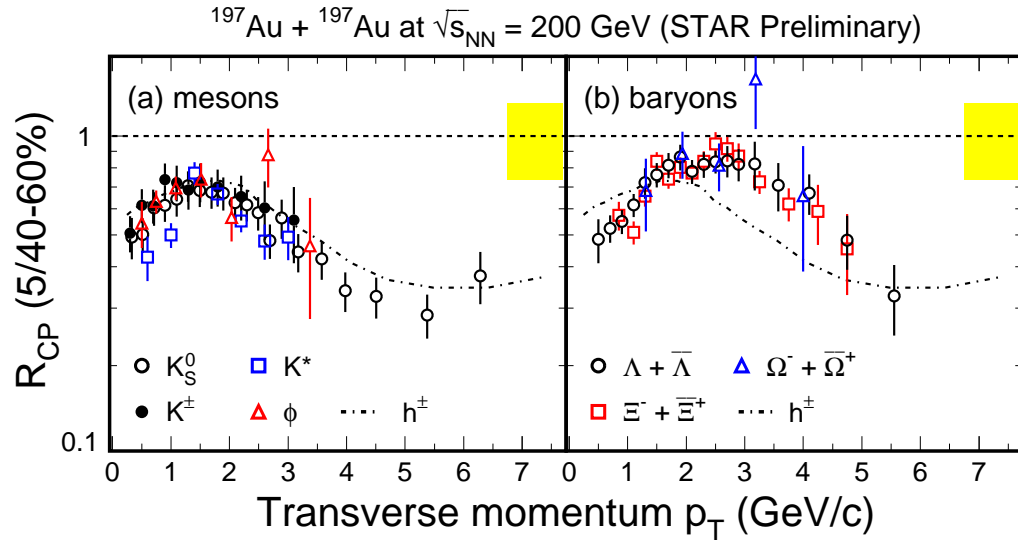


Figure 1.7: The ratio R_{CP} for identified mesons and baryons at mid-rapidity calculated using centrality intervals, 0–5% vs. 40–60% of the collision cross section. The bands represent the uncertainties in the model calculations of N_{bin} . We also show the charged hadron R_{CP} measured by STAR for $\sqrt{s_{NN}} = 200$ GeV [8]. This figure is from [12].

In these models, recombination/coalescence models successfully reproduce R_{AA} of baryons and mesons at intermediate p_T , as well as showing consistency with the v_2 measurement in the same p_T range.

Recombination model

The concept of quark recombination was introduced to describe hadron production at forward rapidity in p+p collisions [25]. At forward rapidity, this mechanism allows a fast quark resulting from a hard parton scattering to recombine with a slow anti-quark, which could be one in the original sea in the incident hadron, or one incited by a gluon [25]. If a QGP is formed in the relativistic heavy ion collisions, then one might expect coalescence of the abundant thermal partons to provide another important hadron production mechanism, active over a wide range of rapidity and transverse momentum [26]. In particular, at moderate p_T values (above the realm of hydrodynamics applicability), the hadron production from recombination of lower p_T partons from thermal bath [21, 22, 23] has been predicted to be competitive with the production from fragmentation of higher p_T scattered partons. It has been suggested [27] that the need for substantial recombination to explain the observed hadron yield and flow may be taken as a signature of QGP formation.

In order to explain the features of RHIC collisions, the recombination models [26, 21, 22, 23] make the central assumption that coalescence proceeds via constituent quarks, whose number in a hadron determines its production rate. The constituent quarks are presumed to follow a thermal (exponential) momentum spectrum and to carry a collective transverse velocity distributions. This picture leads to clear predicted effects on baryon and meson production rates, with the former depending on the spectrum of thermal constituent quarks and antiquarks at roughly one-third the baryon p_T , and the latter determined by the spectrum at roughly one-half the meson p_T . Indeed, the recombination model was recently was re-introduced at RHIC context, precisely to explain the abnormal abundance of baryon vs meson observed at intermediate p_T [21, 22, 23]. If the observed saturated elliptic flow values of hadrons in this momentum range result from coalescence of collectively flowing constituent quarks, then one expect a similarly simple baryon vs meson relationship [21, 22, 23]: the baryon (meson) flow would be 3 (2) times the quark flow at roughly one-third (one-half) the baryon (meson) p_T [13].

1.3.4 Summary

In summary, the several important results from RHIC have been introduced. The elliptic flow v_2 can be reproduced by hydrodynamics at low p_T . At intermediate p_T , v_2 from data show saturation and deviate from hydrodynamical model predictions. At the same time, v_2 from data show baryon or meson species dependence. High p_T suppression can be reproduced by pQCD model and gluon saturation model. The gluon saturation model is also called color glass condensate model (CGC). The production rate dependence on baryon or meson species has been observed at intermediate p_T , which can be reproduced by the recombination model.

1.4 Cronin effect

1.4.1 Why we need d+Au run at RHIC

In order to see the intermediate and high p_T suppression is due to the final-state effect or initial state effect, the measurements from d+Au collisions will provide the essential proof. Since the initial state in d+Au collisions is similar to that in Au+Au collisions, and, it's believed that the quark-gluon plasma doesn't exist in d+Au collisions, the results from d+Au collisions will be very important for us to judge whether the quark-gluon plasma exists in Au+Au collisions or not and to understand the property of the dense matter created in Au+Au collisions. Besides, if the identified particle spectra in d+Au and p+p collisions are measured, they will not only provide the reference for those in Au+Au collisions at 200 GeV, but also provide a chance to see the mechanism of the Cronin effect itself clearly at 200 GeV. Cronin effect was observed 30 years ago experimentally and the study of this effect was only limited to lower energy fixed target experiments. Before we go to the d+Au collisions, let's look back on the p+A collisions at lower energy fixed target experiment.

1.4.2 Lower energy

The hadron p_T spectra have been observed to depend on the target atomic weight (A) and the produced particle species in lower energy p+A collisions [28]. This is known as the ‘‘Cronin Effect’’, a generic term for the experimentally observed broadening of the transverse momentum distributions at intermediate p_T in p+A collisions as compared to those in p+p collisions [28, 29, 30]. The effect can be characterized as a dependence of the yield on the target atomic weight as A^α . At energies of $\sqrt{s} \simeq 30$ GeV, α depends on p_T and is greater than unity at high p_T [28], indicating an enhancement of the production cross section. As shown in Figure 1.8, the α is larger than 1 in the intermediate p_T and shows strong particle-species dependence. The α for proton and antiproton are larger than those for kaon and pion. And α for kaon is larger than that for pion. This effect has been interpreted as partonic scatterings at the initial impact [29, 30]. Besides, the lower energy data suggest the power α

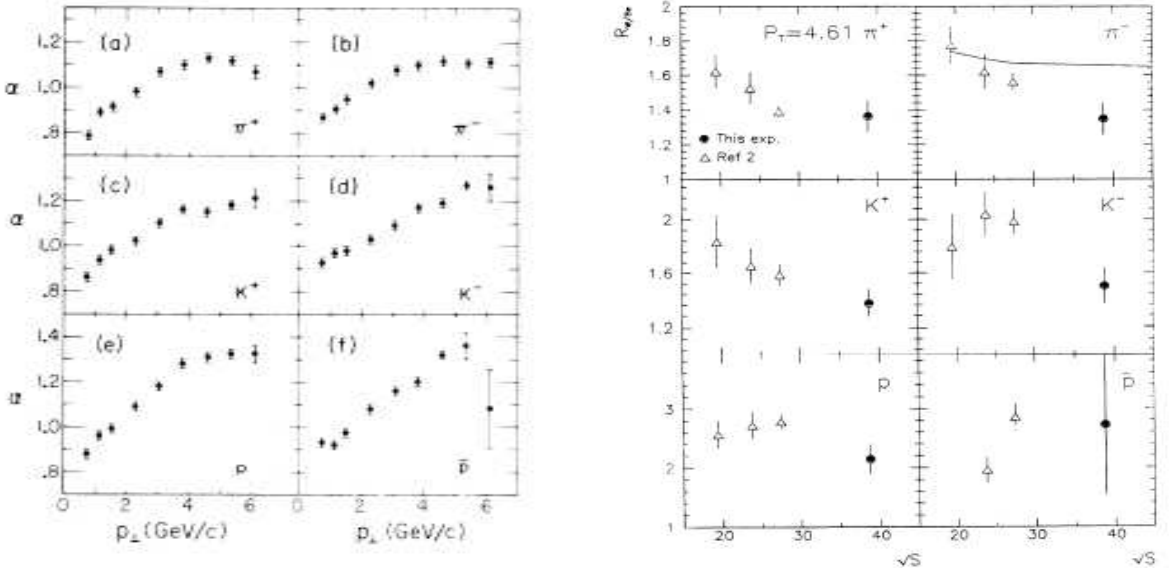


Figure 1.8: (left) The power α of A dependence from 300 GeV incident proton-fixed target experiment. This figure is from [28]. (right) The Cronin ratio R_{W/B_e} at $p_T = 4.61$ GeV/c versus energy. This plot is from [28].

decreases with energy, as shown in Figure 1.8. However, the energy dependence study of Cronin effect is limited to fixed target experiment at lower energy. What's

the extrapolation of Cronin effect at higher energy such as RHIC energy 200 GeV. At higher energies, multiple parton collisions are possible even in p+p collisions [32]. This combined with the hardening of the spectra with increasing beam energy would reduce the Cronin effect [30]. There are several models which give different predictions of Cronin effect at 200 GeV.

1.4.3 Predictions: RHIC energy

One of the models is the initial multiple parton scattering model. In this model, the transverse momentum of the parton inside the proton will be broadened when the proton traverses the Au nucleus due to the multiple scattering between the proton and the nucleons inside the Au nucleus. In these models, the Cronin ratio will increase to a maximum value between 1 and 2 at $2.5 < p_T < 4.5$ GeV/c and then decreases with p_T increasing [30]. The Cronin effect is predicted to be larger in central d+Au collisions than in d+Au peripheral collisions [31]. Another model is the gluon saturation model. At sufficiently high beam energy, gluon saturation is expected to result in a relative suppression of hadron yield at high p_T in both p+A and A+A collisions and in a substantial decrease and finally in the disappearance of the Cronin effect [33]. Figure 1.9 shows the R_{dAu} of charged hadron vs p_T from STAR. We can see that the Cronin ratio increases to a maximum value around 1.5 at $3 < p_T < 4$ GeV/c and then decreases again [36]. This is consistent with the initial multiple parton scattering model [30]. These results on inclusive hadron production from d+Au collisions indicate that hadron suppression at intermediate and high p_T in Au+Au collisions is due to final state interactions in a dense and dissipative medium produced during the collision and not due to the initial state wave function of the Au nucleus [36, 37].

Now we know that the hadron suppression at intermediate p_T in Au+Au collisions is due to final-state effects [36, 37]. What's the effect on particle composition at the same p_T range in Au+Au collisions? Another question is whether there is any Cronin effect dependence on particle-species in d+Au collisions or not. In order to further understand the mechanisms responsible for the particle dependence of p_T spectra in

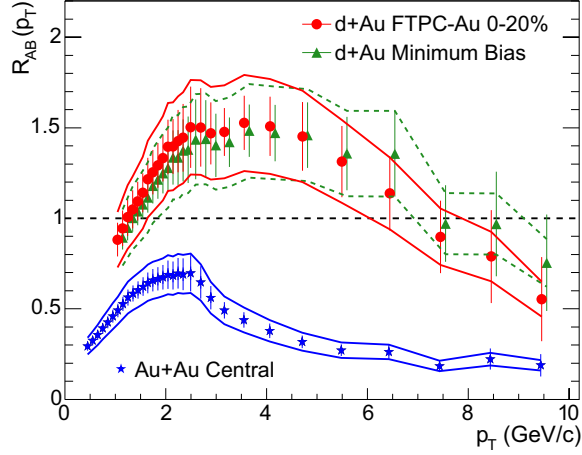


Figure 1.9: R_{AB} for minimum bias and central d+Au collisions, and central Au+Au collisions [8]. The minimum bias d+Au data are displaced 100 MeV/c to the right for clarity. The bands show the normalization uncertainties, which are highly correlated point-to-point and between the two d+Au distributions. This Figure is from [36].

heavy ion collisions, and to separate the effects of initial and final partonic rescatterings, we measured the p_T distributions of π^\pm , K^\pm , p and \bar{p} from 200 GeV d+Au and p+p collisions. In this thesis, we discuss the dependence of particle production on p_T , collision energy, and target atomic weight. And we compare the Cronin effect of π^\pm , K^\pm , p and \bar{p} with models to address the mechanism for Cronin effect in d+Au collisions at $\sqrt{s_{NN}} = 200$ GeV.

Chapter 2

The STAR Experiment

2.1 The RHIC Accelerator

The Relativistic Heavy Ion Collider (RHIC) at Brookhaven National Lab (BNL) is the first hadron accelerator and collider consisting of two independent rings. It is designed to operate at high collision luminosity over a wide range of beam energies and particle species ranging from polarized proton to heavy ion [41, 42], where the top energy of the colliding center-of-mass energy per nucleon-nucleon pair is $\sqrt{s_{NN}} = 200$ GeV. The RHIC facility consists of two super-conducting magnets, each with a circumference of 3.8 km, which focus and guide the beams.

Figure 2.1 shows the BNL accelerator complex including the accelerators used to bring the gold ions up to RHIC injection energy. In the first, gold ions are accelerated to 15 MeV/nucleon in the Tandem Van de Graaff facility. Then the beam is transferred to the Booster Synchrotron and accelerated to 95 MeV/nucleon through the Tandem-to-Booster line. Then the gold ions are transferred to the Alternating Gradient Synchrotron (AGS) and accelerated to 10.8 GeV/nucleon. Finally they are injected to RHIC and accelerated to the collision energy 100 GeV/nucleon.

RHIC's 3.8 km ring has six intersection points where its two rings of accelerating magnets cross, allowing the particle beams to collide. The collisions produce the fleeting signals that, when captured by one of RHIC's experimental detectors, provide physicists with information about the most fundamental workings of nature. If

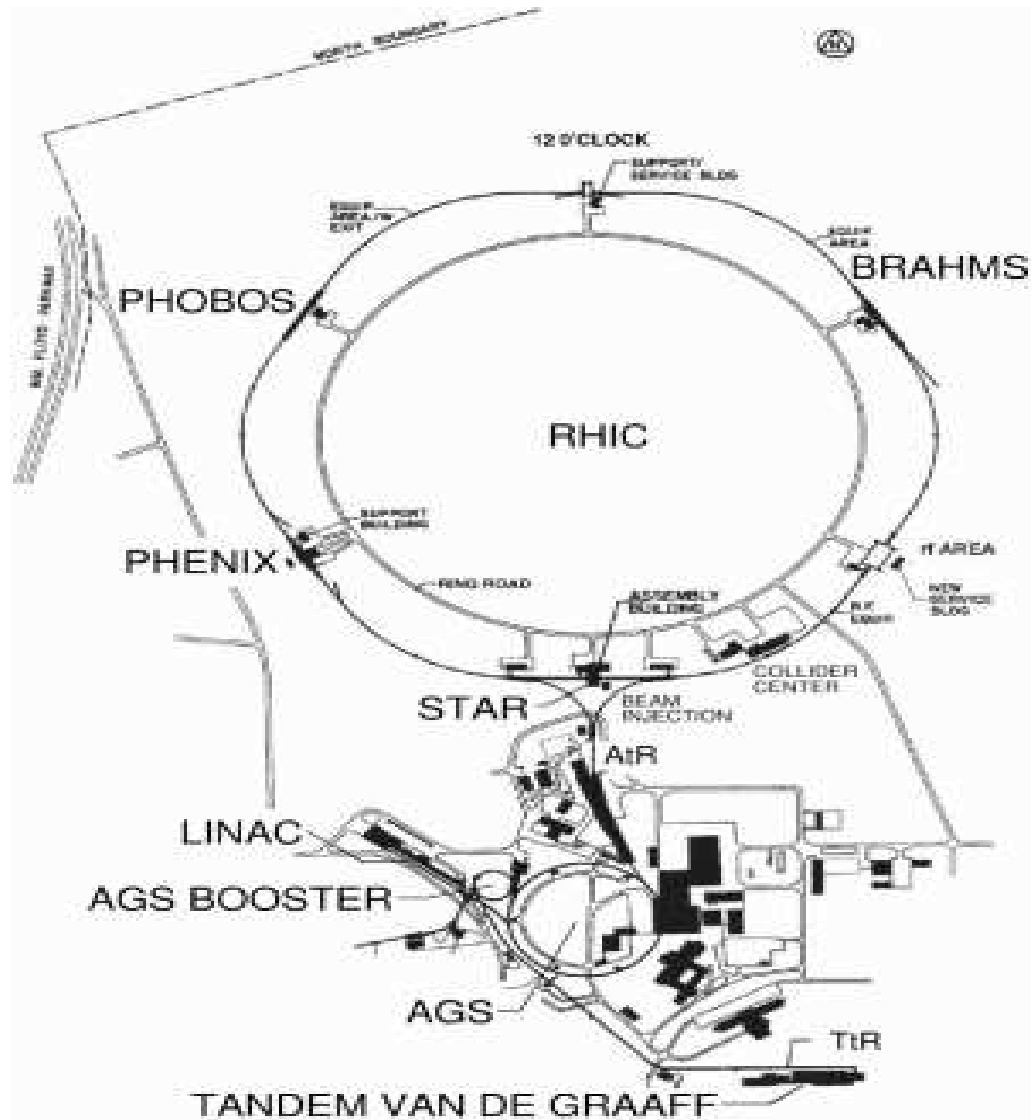


Figure 2.1: A diagram of the Brookhaven National Laboratory collider complex including the accelerators that bring the nuclear ions up to RHIC injection energy (10.8 GeV/nucleon for ^{197}Au). Figure is taken from [40, 81].

RHIC's ring is thought of as a clock face, the four current experiments are at 6 o'clock (STAR), 8 o'clock (PHENIX), 10 o'clock (PHOBOS) and 2 o'clock (BRAHMS). There are two additional intersection points at 12 and 4 o'clock where future experiments may be placed [41].

2.2 The STAR Detector

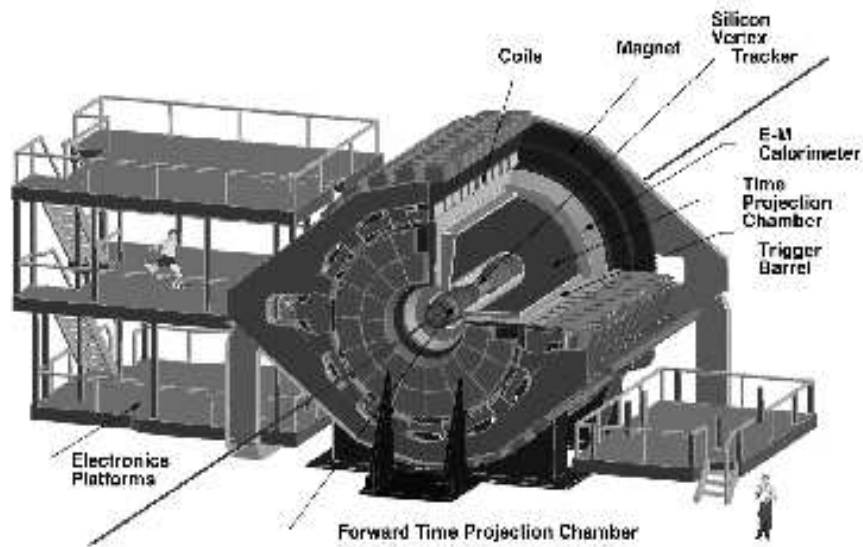


Figure 2.2: Perspective view of the STAR detector, with a cutaway for viewing inner detector systems. Figure is taken from [43].

The Solenoidal Tracker at RHIC (STAR) is one of the two large detector systems constructed at the Relativistic Heavy Ion Collider (RHIC) at Brookhaven National Laboratory. STAR was constructed to investigate the behavior of strongly interacting matter at high energy density and to search for signatures of quark-gluon plasma (QGP) formation. Key features of the nuclear environment at RHIC are a large number of produced particles (up to approximately one thousand per unit pseudorapidity) and high momentum particles from hard parton-parton scattering. STAR can measure many observables simultaneously to study signatures of a possible QGP phase transition and to understand the space-time evolution of the collision process

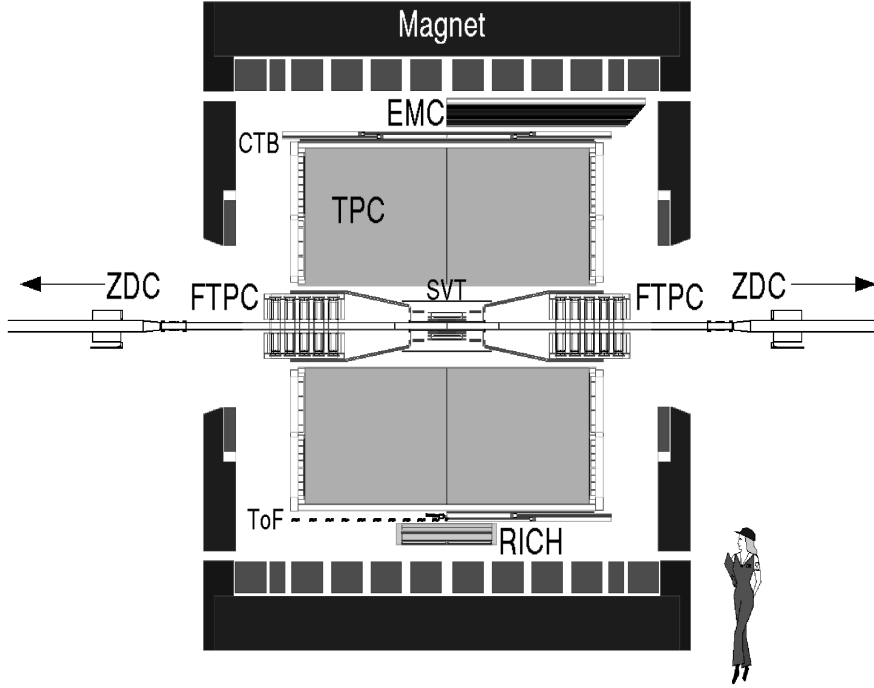


Figure 2.3: Cutaway side view of the STAR detector as configured in 2001. Figure is taken from [43].

in ultra-relativistic heavy ion collisions. The goal is to obtain a fundamental understanding of the microscopic structure of these hadronic interactions at high energy densities. In order to accomplish this, STAR was designed primarily for measurements of hadron production over a large solid angle, featuring detector systems for high precision tracking, momentum analysis, and particle identification at the center of mass (c.m.) rapidity. The large acceptance of STAR makes it particularly well suited for event-by-event characterizations of heavy ion collisions and for the detection of hadron jets [43].

The layout of the STAR experiment [44] is shown in Figure 2.2. A cutaway side view of the STAR detector as configured for the RHIC 2001 run is displayed in Figure 2.3. A room temperature solenoidal magnet [45] with a maximum magnetic field of 0.5 T provides a uniform magnetic field for charged particle momentum analysis. Charged particle tracking close to the interaction region is accomplished by a Silicon Vertex Tracker [46] (SVT). The Silicon Drift Detectors [47] (SDD) installed after 2001 is also

for the inner tracking. The silicon detectors cover a pseudo-rapidity range $|\eta| \leq 1$ with complete azimuthal symmetry ($\Delta\phi = 2\pi$). Silicon tracking close to the interaction allows precision localization of the primary interaction vertex and identification of secondary vertices from weak decays of, for example, Λ , Ξ , and Ω . A large volume Time Projection Chamber [48, 38] (TPC) for charged particle tracking and particle identification is located at a radial distance from 50 to 200 cm from the beam axis. The TPC is 4 meters long and it covers a pseudo-rapidity range $|\eta| \leq 1.8$ for tracking with complete azimuthal symmetry ($\Delta\phi = 2\pi$). Both the SVT and TPC contribute to particle identification using ionization energy loss, with an anticipated combined energy loss resolution (dE/dx) of 7 % (σ). The momentum resolution of the SVT and TPC reach a value of $\delta p/p = 0.02$ for a majority of the tracks in the TPC. The $\delta p/p$ resolution improves as the number of hit points along the track increases and as the particle's momentum decreases, as expected [43].

To extend the tracking to the forward region, a radial-drift TPC (FTPC) [50] is installed covering $2.5 < |\eta| < 4$, also with complete azimuthal coverage and symmetry. To extend the particle identification in STAR to larger momenta over a small solid angle for identified single-particle spectra at mid-rapidity, a ring imaging Cherenkov detector [51] covering $|\eta| < 0.3$ and $\Delta\phi = 0.11\pi$, and a time-of-flight patch (TOFp) [73] covering $-1 < \eta < 0$ and $\Delta\phi = 0.04\pi$ (as shown in Figure 2.3) was installed at STAR in 2001 [43]. In 2003, a time-of-flight tray (TOFr) based on multi-gap resistive plate chamber (MRPC) technology [39] was installed in STAR detector, covering $-1 < \eta < 0$ and $\Delta\phi = \pi/30$. For the time-of-flight system, the Pseudo-Vertex Position Detectors (pVPD) was installed as the start-timing detector, which was 5.4 m away from TPC center and covers $4.4 < |\eta| < 4.9$ with the azimuthal coverage 19% [73] in 2003.

The fast detectors that provide input to the trigger system are a central trigger barrel (CTB) at $|\eta| < 1$ and two zero-degree calorimeters (ZDC) located in the forward directions at $\theta < 2$ mrad. The CTB surrounds the outer cylinder of the TPC, and triggers on the flux of charged particles in the mid-rapidity region. The ZDCs are used for determining the energy in neutral particles remaining in the forward directions [43]. A minimum bias trigger was obtained by selecting events with a pulse

height larger than that of one neutron in each of the forward ZDCs, which corresponds to 95 percent of the geometrical cross section [43].

2.2.1 The Time Projection Chamber

The STAR detector [44] uses the TPC as its primary tracking device. The TPC records the tracks of particles, measures their momenta, and identifies the particles by measuring their ionization energy loss (dE/dx). Particles are identified over a momentum range from 100 MeV/c to greater than 1 GeV/c and momenta are measured over a range of 100 MeV/c to 30 GeV/c [38].

The STAR TPC is shown schematically in Figure 2.4. It is a volume of gas in a well defined uniform electric field of ≈ 135 V/cm. The working gas of TPC is P10 gas (10% methane, 90% argon) regulated at 2 mbar above atmospheric pressure[54]. This gas has long been used in TPCs. Its primary attribute is a fast drift velocity which peaks at a low electric field. Operating on the peak of the velocity curve makes the drift velocity stable and insensitive to small variations in temperature and pressure [38]. The paths of primary ionizing particles passing through the gas volume are reconstructed with high precision from the released secondary electrons which drift to the readout end caps at the ends of the chamber. The drift velocity of electrons is 5.45 cm/ μ s. The uniform electric field which is required to drift the electrons is defined by a thin conductive Central Membrane (CM) at the center of the TPC, concentric field cage cylinders and the read out end caps [38]. The readout system is based on Multi Wire Proportional Chambers (MWPC) with readout pads. The drifting electrons avalanche in the high fields at the 20 μ m anode wires providing an amplification of 1000 to 3000. The induced charge from an avalanche is shared over several adjacent pads, so the original track position can be reconstructed to a small fraction of a pad width. There are a total of 136,608 pads in the readout system [38], which give x - y coordinate information. The z position information is provided by 512 time buckets.

At the Data Acquisition (DAQ) stage, raw events containing millions of ADC values and TDC values were recorded. Raw data were then reconstructed into hits, tracks,

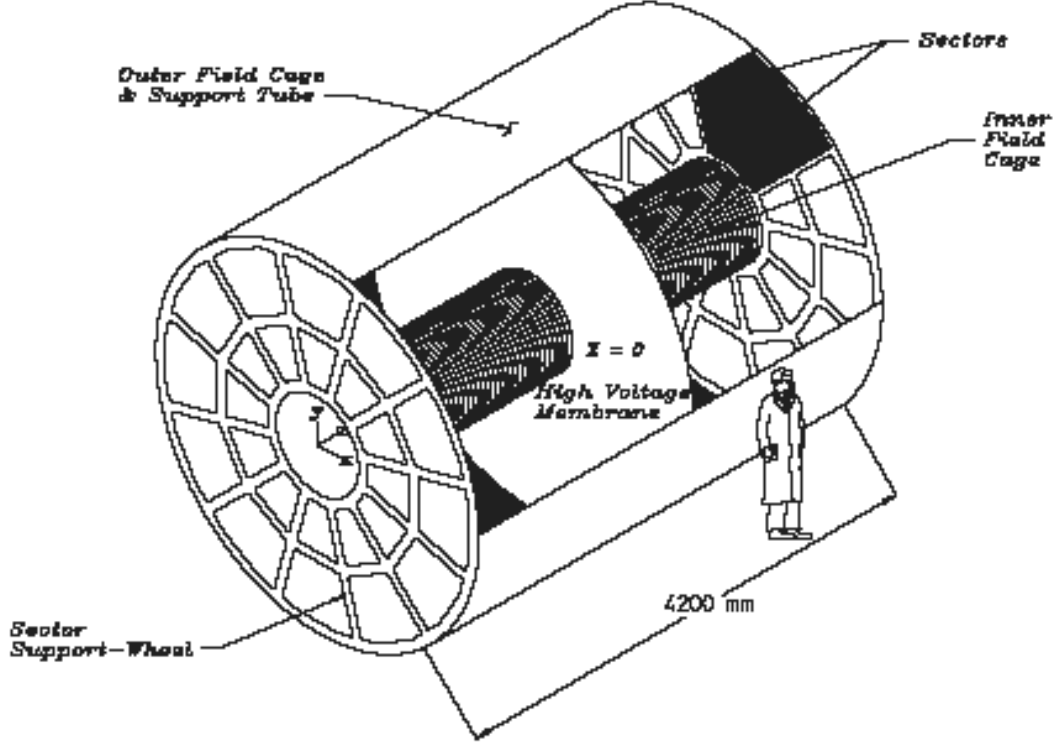


Figure 2.4: The STAR TPC surrounds a beam-beam interaction region at RHIC. The collisions take place near the center of the TPC.

vertices, and the collision vertex through the reconstruction chain of TPC [55] by Kalman method. The collision vertex are called the primary vertex. The tracks are called the global tracks. If the 3-dimensional distance of closest approach (DCA/dca) of the global track to the primary vertex is less than 3 cm, this track will be chosen for a re-fit by forcing a new track helix ending at the primary vertex. These newly reconstructed helices are called primary tracks [81]. As expected, the vertex resolution decreases as the square root of the number of tracks used in the calculation. The vertex resolution is $350 \mu\text{m}$ when there are more than 1,000 tracks [38]. Figure 2.5 shows the beam's eye view of a central Au+Au collision event in the STAR TPC.

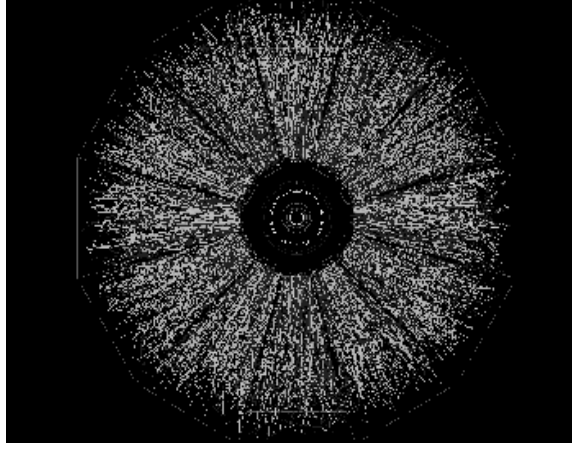


Figure 2.5: Beam's eye view of a central Au+Au collision event in the STAR Time Projection Chamber. This event was drawn by the STAR online display. Figure is taken from [43].

Particle Identification (PID) of TPC by dE/dx

Energy lost in the TPC gas is a valuable tool for identifying particle species. It works especially well for low momentum particles but as the particle energy rises, the energy loss becomes less mass-dependent and it is hard to separate particles with velocities $v > 0.7c$ [38]. For a particle with charge z (in units of e) and speed $\beta = v/c$ passing through a medium with density ρ , the mean energy loss it suffers can be described by the Bethe-Bloch formula

$$\left\langle \frac{dE}{dx} \right\rangle = 2\pi N_0 r_e^2 m_e c^2 \rho \frac{Z z^2}{A \beta^2} \left[\ln \frac{2m_e \gamma^2 v^2 E_M}{I^2} - 2\beta^2 \right] \quad (2.1)$$

where N_0 is Avogadro's number, m_e is the electron mass, $r_e (= e^2/m_e)$ is the classical electron radius, c is the speed of light, Z is the atomic number of the absorber, A is the atomic weight of the absorber, $\gamma = 1/\sqrt{1-\beta^2}$, I is the mean excitation energy, and $E_M (= 2m_e c^2 \beta^2 / (1-\beta^2))$ is the maximum transferable energy in a single collision [83, 81]. From the above equation, we can see that different charged particles (electron, muon, pion, kaon, proton or deuteron) with the same momentum p passing through the TPC gas can result in different energy loss. Figure 2.6 shows the energy loss for particles in the TPC as a function of the particle momentum, which includes both primary and secondary particles. We can see that charged pions and kaons

can be identified up to about transverse momentum 0.75 GeV/c and protons and anti-protons can be identified to 1.1 GeV/c.

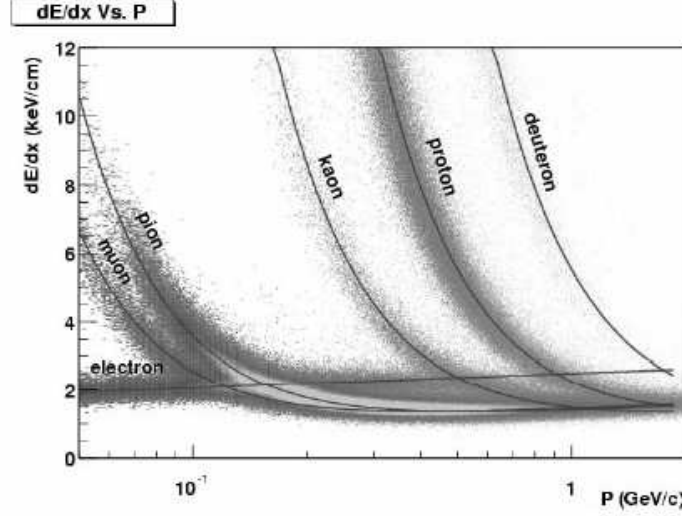


Figure 2.6: The energy loss distribution for primary and secondary particles in the STAR TPC as a function of the p_T of the primary particle. This figure is taken from [38].

In order to quantitatively describe the particle identification, we define the variable $N_{\sigma\pi}$ (in the case of charged pion identification) as

$$N_{\sigma\pi} = \left[\frac{dE}{dx}_{meas.} - \langle \frac{dE}{dx} \rangle_{\pi} \right] / \left[\frac{0.55}{\sqrt{N}} \frac{dE}{dx}_{meas.} \right] \quad (2.2)$$

in which N is the number of hits for a track in the TPC, $\frac{dE}{dx}_{meas.}$ is the measured energy loss of a track and $\langle \frac{dE}{dx} \rangle_{\pi}$ is the mean energy loss for charged pions. In order to identify charged kaons, protons and anti-protons, we can have similar definition of $N_{\sigma K}$ and $N_{\sigma p}$. Thus we can cut on the variables $N_{\sigma\pi}$, $N_{\sigma K}$ and $N_{\sigma p}$ to select different particle species [81].

A specific part of the particle identification is the topological identification of neutral particles, such as the K_S^0 and Λ . These neutral particles can be reconstructed by identifying the secondary vertex, commonly called V0 vertex, of their charged daughter decay modes, $K_S^0 \rightarrow \pi^+\pi^-$ and $\Lambda \rightarrow p\pi^-$ [81].

2.2.2 The time-of-flight tray based on MRPC technology

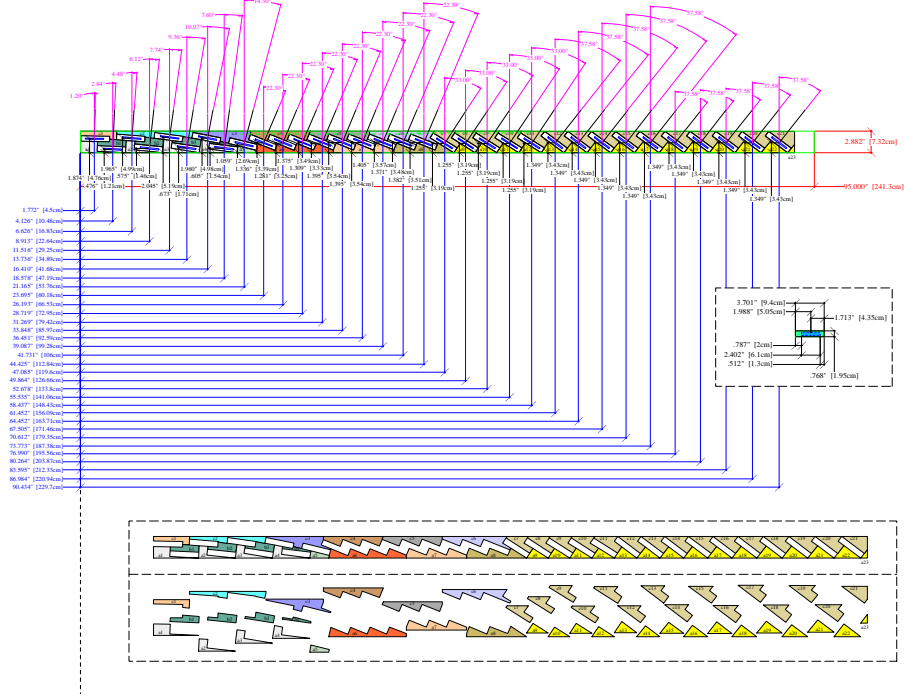


Figure 2.7: Tray structure. Figure is taken from [74].

In 2003, the time-of-flight tray (TOFr) based on multi-gap resistive plate chamber (MRPC) technology [39] was installed in STAR detector. It extends particle identification up to $p_T \sim 3$ GeV/c for p and \bar{p} . This tray was installed on the Au beam outgoing direction. MRPC technology was first developed by the CERN ALICE group [56] to provide a cost-effective solution for large-area time-of-flight coverage. For full time-of-flight coverage at STAR, there will be 120 trays, with 60 on east side and 60 on west side. For each tray, there will be 33 MRPCs. For each MRPC, there are 6 read-out channels. Figure 2.7 shows the tray which indicates the position of each MRPC module. The MRPCs are tilted differently so that each MRPC is most projective to the average primary vertex location at $Z=0$. In 2003 d+Au and p+p run, only 28 MRPCs were installed in the tray and 12 out of 28 were instrumented with the electronics, representing 0.3% of TPC coverage. If we number the

33 MRPCs in the tray from 1 to 33, with 1 close to TPC center and 33 far from TPC center, the numbers of 12 modules instrumented with the electronics in 2003 are 3,4,5,7,9,10,11,12,13,14,26 and 32.

The introduction of MRPC

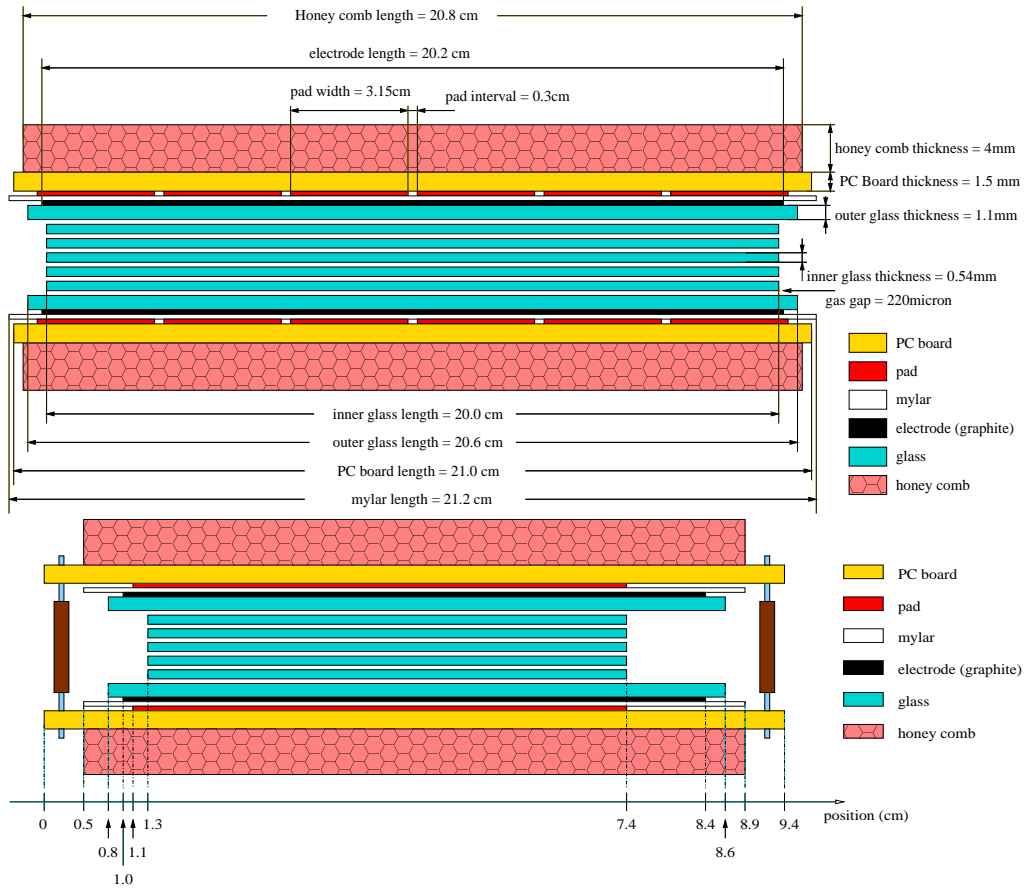


Figure 2.8: Two side views of MRPC. The upper (lower) is for long (short) side view. The two plots are not at the same scale. Figure is taken from [74].

Resistive Plate Chambers (RPCs) were developed in 1980s [57], and were originally operated in streamer mode. This operation mode allows us to get high detection efficiency ($>95\%$) and time resolution (1 ns), with low fluxes of incident particles. At higher fluxes ($>200 \text{ Hz/cm}^2$), RPCs begin to lose their efficiency. A way to overcome this problem is to operate RPCs in avalanche mode. The Multi-gap Resistive Plate

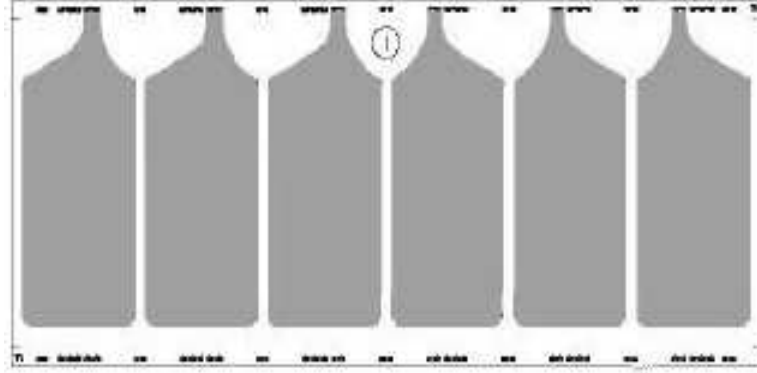


Figure 2.9: The shape of the 6 read-out strips for each MRPC.

Chamber (MRPC) was developed less than 10 years ago [58]. It consists of a stack of resistive plates, spaced one from the other with equal sized spacers creating a series of gas gaps. Electrodes are connected to the outer surfaces of the stack of resistive plates while all the internal plates are left electrically floating. Initially the voltage on these internal plates is given by electrostatics, but they are kept at the correct voltage due to the flow of electrons and ions created in the avalanches. Figure 2.8 shows the structure of MRPC detector. For each MRPC, there are 6 read-out strips. Figure 2.9 shows the shape of the read-out strip. The detailed production process can be found at Appendix B.

MRPC, as a new kind of detector for time of flight system, operated in avalanche mode with a non flammable gas mixture of 90% F134A, 5% isobutane, 5% SF₆, can fulfill all these requirements: high efficiency ($>95\%$), excellent intrinsic time resolution (<100 ps) [69, 39, 70, 71, 72], high rate capability (500 Hz/cm^2), high modularity and simplicity for construction, good uniformity of response, high granularity/low occupancy, and large acceptance.

Simulation: the work principle of this chamber

A detailed description of the model used in the simulation was reported in these papers [59, 60, 61, 62], here just the main items will be repeated. The program starts from considering an ionizing particle which crosses the gas gaps and generates a certain number of clusters of ion-electron pairs. The electrons contained in the clusters

drift towards the anode and, if the electric field is sufficiently high, give rise to the avalanche processes.

The primary cluster numbers and the avalanche growth are assumed to follow, respectively, simple Poisson statistics and the usual exponential law. Avalanche gain fluctuations have been taken into account using a Polya distribution [63]. After the simulation of the drifting avalanches, the program computes, by means of Ramo [64] theorem, the charge q_{ind} induced on the external pick-up electrodes (strips or pads) by the avalanche motion. Under certain approximations, this is given by the formula

$$q_{ind} = \frac{q_e}{\eta d} \Delta V_w \sum_{j=1}^{n_{cl}} n_j M(e^{\eta(d-x_j)} - 1) \quad (2.3)$$

where q_e is the electron charge, η 1st effective Townsend coefficient $\eta = \alpha - \beta$, α is the Townsend coefficient, β is the attachment coefficient, x_j the j_{th} cluster initial distances from the anode, d the gap width, n_j the number of initial electrons in the considered j_{th} cluster, M the avalanche gain fluctuations factor, and $\Delta V_w/d = E_w$ is the normalized weighting field. In addition to q_{ind} , the current $i_{ind}(t)$ induced on the same electrodes by the drifting charge $q_d(t)$ may be computed as

$$i_{ind}(t) = \Delta V_w \frac{v_d}{d} q_d(t) M e^{\eta v_d t} \quad (2.4)$$

, where v_d is the electron drift velocity. The computation of i_{ind} allows us to reproduce the whole information coming out from MRPC, such as time distribution.

Charge Spectrum Simulation: The almost Gaussian charge distribution obtained with the MRPC is a key ingredient to its performance. If the avalanches grew following Townsend's formula the charge distribution would be exponential in shape. Thus the space charge effects must be considered in the simulation.

The input parameters for the simulation program are: the Townsend coefficient α , the attachment coefficient β , the average distance between clusters λ and the probability distribution of the number of electrons per cluster. These pieces of information can be obtained, for a given gas mixture and given conditions (pressure and temperature) and electric field, by the programs HEED [65] and MAGBOLTZ [66, 67]. In addition, a maximum number of electrons in an avalanche (cutoff value) is specified.

In a given gap, we generate a number of clusters with distances exponentially distributed with average distance λ . For each cluster, we then generate a certain number of electrons, according to the distribution obtained by the program HEED. Each electron from the primary cluster will give rise to a number of electrons, generated according to an exponential probability law.

For each cluster, the avalanche growth is stopped when the total charge reaches

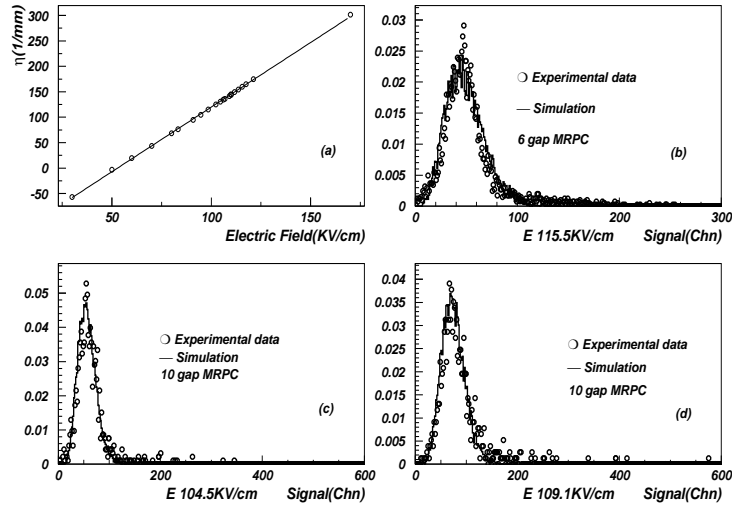


Figure 2.10: Simulated 1st effective Townsend coefficient curve and normalized charge distribution for a 6 and 10 gap MRPC.

a certain cutoff value, as originally suggested in ref. [68] to take into account space charge effects in the avalanche development. This cutoff value has been set to be 1.6×10^7 electrons.

In Figure 2.10 we show the results of simulations, Figure 2.10(a) is the simulated curve of the 1st effective Townsend coefficient η versus the electric field, which is generated by Magboltz. The curve shows that the correlation between η and the electric field is almost linear when MRPC is operated at high electric field for the gas mixture. Figure 2.10(b) is the charge spectrum for a 6 gap chamber and (c) (d) for a 10 gap chamber compared to experimental data [69, 39], and the number under each plot shows the electric field E in the gas gap for MRPC. In both cases the gap size

is $220 \mu m$. The gas mixture was 90% F134A, 5% isobutane and 5% SF6 in normal conditions of pressure and temperature. The value of λ used was $0.1 mm$, derived from HEED program.

The charge distribution has an almost Gaussian form, especially for the 10 gap MRPC. The left side of the distribution (very few events at values near zero) is due to the fact that the MRPC operates at high gain $\eta \times d \sim 30$. This means that avalanches starting in the middle of the gap width, which only avalanche over half the distance, give a detectable signal. The charge distribution is the superposition of several probability distributions which, according to the central limit theorem, will tend to a Gaussian form. The right side of the charge distribution (the fact that the tails are not very long) indicates that indeed the space charge effects stop the development of the avalanche.

Time Distribution Simulation: We then proceed to simulate the time distribu-

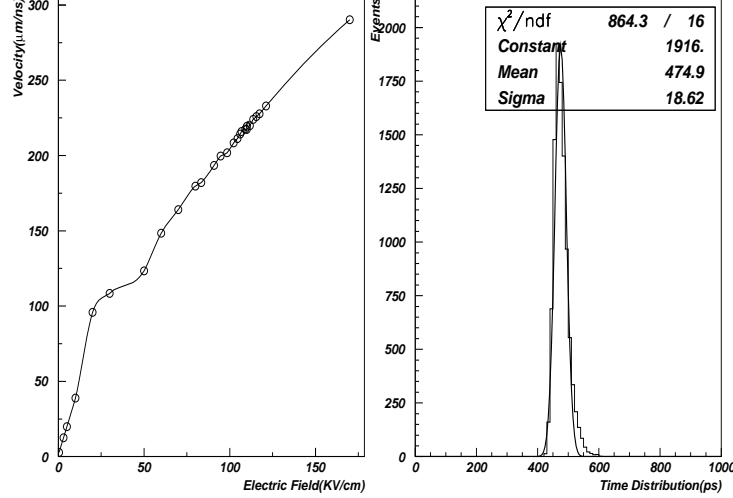


Figure 2.11: Simulated results of a 6 gap MRPC.

tion of these same chambers. The electron drift velocity can be obtained from HEED. When the total induced charge signal is over threshold, the time is recorded. In this paper, the threshold is 13 fc for the 6 gap MRPC and 26 fc for the 10 gap MRPC. Figure 2 is the simulated results for a 6 gap chamber. Figure 2.11 (a) is the simulated

curve of the electron drift velocity versus the electric field, which is generated by Magboltz. Figure 2.11 (b) is the time distribution of a 6 gap MRPC. The intrinsic time resolution is only 19 ps or so. If we consider other contributions, such as front-end electronics 30 ps, TDC resolution 25 ps, fanout start signal 10 ps, beam size (1cm) 15 ps, we can get the MRPC resolution is $\sqrt{20^2 + 30^2 + 25^2 + 10^2 + 15^2} = 47$ ps. This value is similar to the experimental result [69, 39]. For a 10 gap MRPC, the intrinsic time resolution is about 15 ps.

From the simulation, we can get the bottom line of MRPC time resolution ~ 20 ps. And we need to keep control of all these contributions to ensure best time resolution.

MRPC for this tray installed in 2003

In 2003, for the MRPCs in the TOFr, the inner glass thickness is 0.54 mm, the outer glass is 1.1 mm. The gas gap is 0.22 mm. Both the volume resistivity ($10^{12-13} \text{ ohm.cm}$) of the glass plates and the surface resistivity (2M ohm per square) of carbon layer at room temperature are presented in [75]. It is found the volume resistivity of the plate decreases with the temperature increasing. And the radiation will decrease the volume resistivity of the plate [75]. In order not to pollute the working gas of TPC, SF6 is not used as part of the working gas of TOFr. The working gas of MRPC-TOFr at STAR is 95% freon and 5% iso-butane at normal atmospheric pressure. The high voltage applied to the electrodes is 14.0 kV.

Chapter 3

Analysis Methods

3.1 Trigger

The detector used for these studies was the Solenoidal Tracker at RHIC (STAR). The main tracking device is the Time Projection Chamber (TPC) which provides momentum information and particle identification for charged particles up to $p_T \sim 1.1$ GeV/c by measuring their ionization energy loss (dE/dx) [38]. Detailed descriptions of the TPC and d+Au run conditions have been presented in Ref. [36, 38]. A prototype time-of-flight detector (TOFr) based on multi-gap resistive plate chambers (MRPC) [39] was installed in STAR for the d+Au and p+p runs. It extends particle identification up to $p_T \sim 3$ GeV/c for p and \bar{p} .

TOFr covers $\pi/30$ in azimuth and $-1 < \eta < 0$ in pseudorapidity at a radius of ~ 220 cm. It contains 28 MRPC modules which were partially instrumented during the 2003 run. Since the acceptance of TOFr is small, a special trigger selected events with a valid pVPD coincidence and at least one TOFr hit. A total of 1.89 million and 1.08 million events were used for the analysis from TOFr triggered d+Au and non-singly diffractive (NSD) p+p collisions, representing an integrated luminosity of about $40 \mu\text{b}^{-1}$ and 30nb^{-1} , respectively. Minimum-bias d+Au and p+p collisions that did not require pVPD and TOFr hits were also used to study the trigger bias and enhancement, and the TOFr efficiency and acceptance. The d+Au minimum-bias trigger required an equivalent energy deposition of about 15 GeV in the Zero Degree

Calorimeter in the Au beam direction [36]. The trigger efficiency was determined to be $95 \pm 3\%$. Minimum-bias p+p events were triggered by the coincidence of two beam-beam counters (BBC) covering $3.3 < |\eta| < 5.0$ [8]. The NSD cross section was measured to be 30.0 ± 3.5 mb by a van der Meer scan and PYTHIA [76] simulation of the BBC acceptance [8].

3.1.1 Centrality tagging

Centrality tagging of d+Au collisions was based on the charged particle multiplicity in $-3.8 < \eta < -2.8$, measured by the Forward Time Projection Chamber in the Au beam direction [36, 78]. The TOFr triggered d+Au events were divided into three centralities: most central 20%, 20 – 40% and 40– \sim 100% of the hadronic cross section. The average number of binary collisions $\langle N_{bin} \rangle$ for each centrality class and for the combined minimum-bias event sample is derived from Glauber model calculations and listed in Table 3.1.

Table 3.1 also lists the uncorrected FTPC east reference multiplicity ranges for centrality definitions.

Centrality Bin	Uncorr. FTPCRefMult Range	Uncorr. N_{charge}	N_{bin}
M.B.		10.2	7.5 ± 0.4
0%-20%	$\text{FTPCRefMult} \geq 17$	17.58	15.0 ± 1.1
20%-40%	$10 \leq \text{FTPCRefMult} < 17$	12.55	10.2 ± 1.0
40%-100%	$0 \leq \text{FTPCRefMult} < 10$	6.17	4.0 ± 0.3

Table 3.1: Centrality definitions for different uncorrected FTPC east reference multiplicity ranges. Uncorrected N_{charge} stands for the average value of uncorrected reference multiplicity in certain centrality bin. The fourth column represents the number of binary collisions $\langle N_{bin} \rangle$ calculated from Glauber model.

3.1.2 Trigger bias study

Since we set up a special trigger which selected events with a valid pVPD coincidence and at least one TOFr hit, the study of p_T dependence of trigger bias is necessary. Figure 3.1 shows there is negligible trigger bias on p_T dependence at $p_T > 0.3$

GeV/c from simulation. In this figure, pVPD means that pVPD is required to fire in minimum-bias collisions. TOF means that TOFr is required to fire in minimum-bias collisions, and pVPD & TOF means that pVPD and TOFr are required to fire in minimum-bias collisions. From this figure, if we required pVPD and TOFr to fire, we can see the ratio is flat with p_T when p_T is larger than 0.3 GeV/c by comparison through the p_T distribution in minimum-bias collisions. That means the trigger bias for p_T distribution is negligible at $p_T > 0.3$ GeV/c.

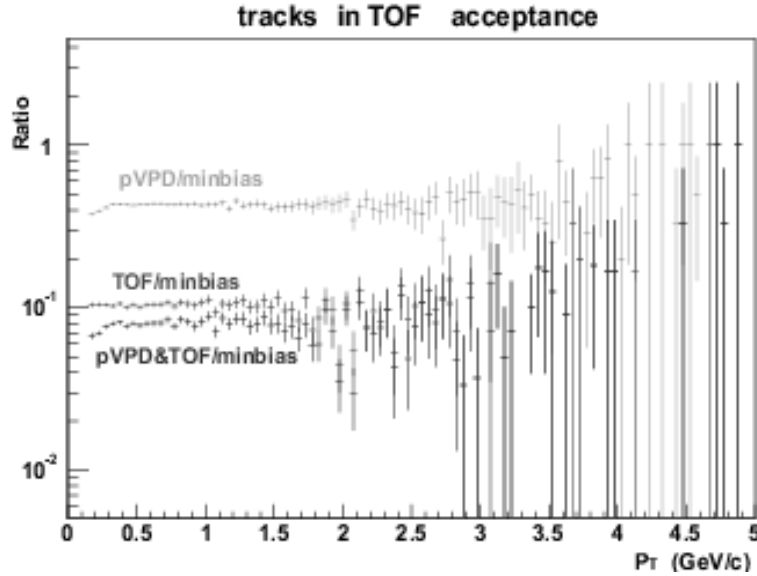


Figure 3.1: The p_T dependence plot of the trigger bias.

Minimum-bias d+Au and p+p collisions are used to study the trigger bias and enhancement. Figure 3.2 shows the trigger bias and enhancement in d+Au minimum-bias collisions and three centrality bins. In this figure, TOFr means that TOFr is required to fire in minimum-bias events. pVPD means that TOFr and pVPD are required to fire in minimum-bias events. Minbias means the minimum-bias triggered events. For enhancement study, TOFr/pVPD is the ratio of the number of events in which TOFr is required to fire over the number of events in which TOFr and pVPD are required to fire, and Minbias/pVPD is the ratio of the number of minimum-bias triggered events over the number of events in which TOFr and pVPD are required to

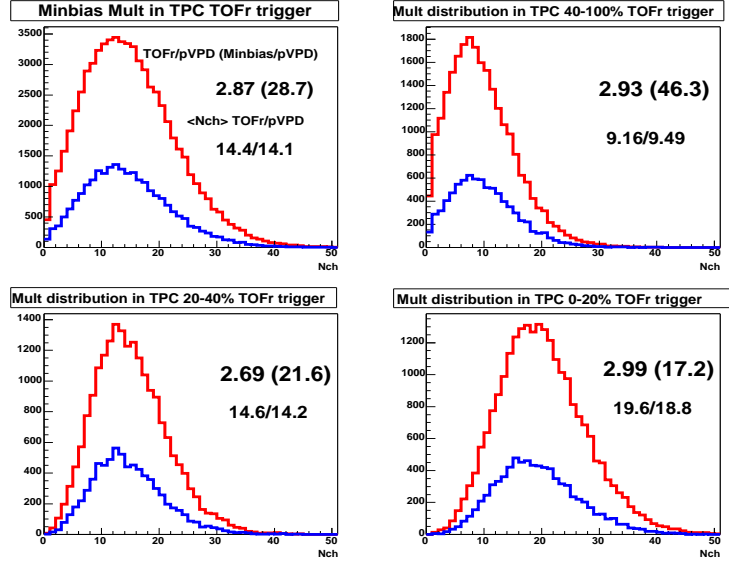


Figure 3.2: The enhancement factor and $\langle N_{ch} \rangle$ bias in minimum-bias and centrality selected d+Au collisions.

fire. The enhancement factor for TOFr is $(\text{Minbias}/\text{pVPD})/(\text{TOFr}/\text{pVPD})$. For example, in minimum-bias collision, Minbias/pVPD is equal to 28.7, while TOFr/pVPD is 2.87, so in minimum-bias collisions, the enhancement of TOFr trigger is 10. For $\langle N_{ch} \rangle$ bias study, TOFr/pVPD is the ratio of $\langle N_{ch} \rangle$ in the events where TOFr is required to fire over the $\langle N_{ch} \rangle$ in the events where TOFr and pVPD are required to fire. Since in our triggered events, TOFr and pVPD are required to fire, TOFr/pVPD is our $\langle N_{ch} \rangle$ bias factor. The curves in this figure show the charged particle multiplicity at mid-rapidity in TOFr events and in TOFr and pVPD events individually. Table 3.2 lists the enhancement factor and trigger bias in minimum-bias, centrality selected d+Au collisions and minimum-bias p+p collisions.

3.2 Track selection and calibration

The TPC and TOFr are two independent systems. In the analysis, hits from particles traversing the TPC were reconstructed as tracks with well defined geometry, momentum, and dE/dx [38]. The particle trajectory was then extended outward to

Centrality Bin	TOFr triggered events	enhancement factor	$\langle N_{ch} \rangle$ bias
0%-100%	1.80 M	10.0	1.02
0%-20%	0.523 M	5.75	1.04
20%-40%	0.500 M	8.03	1.03
40%-100%	0.479 M	15.8	0.965
p+p	0.995 M	37.4	1.19

Table 3.2: Trigger bias study. The $\langle N_{ch} \rangle$ bias and enhancement factor in minimum-bias, centrality selected d+Au collisions and minimum-bias p+p collisions.

the TOFr detector plane. The pad with the largest signal within one pad distance to the projected point was associated with the track for further time-of-flight and velocity (β) calculations.

3.2.1 Calibration

pVPD calibration

For TOFr, we use pVPD as our start-timing detector. In d+Au and p+p collisions, at least one east pVPD and one west pVPD were required to fire. In d+Au collisions, to calibrate east pVPD, we required 3 east pVPD to fire; to calibrate west pVPD, we required 3 west pVPD to fire. In p+p collisions, to calibrate east pVPD, we required 2 east pVPD to fire; to calibrate west pVPD, we required 2 west pVPD to fire. Let's take the east pVPD calibration in d+Au collisions as an example. The label for 3 pVPD are pVPD1, pVPD2, pVPD3, the adc and tdc value for pVPD1 are $a1$, $t1$, and the slewing correction function is $f1$; the adc and tdc value for pVPD2 are $a2$, $t2$, and the slewing correction function is $f2$; the adc and tdc value for pVPD3 are $a3$, $t3$, and the slewing correction function is $f3$. We use $t1 - ((t2 - f2) + (t3 - f3))/2$ vs $a1$ to get the slewing correction for pVPD1; use $t2 - ((t3 - f3) + (t1 - f1))/2$ vs $a2$ to get the slewing correction for pVPD2; use $t3 - ((t1 - f1) + (t2 - f2))/2$ vs $a3$ to get the slewing correction for pVPD3. At the beginning, $f1 = f2 = f3 = 0$, we got 3 curves of $t1 - ((t2 - f2) + (t3 - f3))/2$ vs $a1$, $t2 - ((t3 - f3) + (t1 - f1))/2$ vs $a2$ and $t3 - ((t1 - f1) + (t2 - f2))/2$ vs $a3$. The 3 curves corresponded to the 3 slewing functions $f(a1)$, $f(a2)$, $f(a3)$; For the second step, $f1 = f(a1)$, $f2 = f(a2)$, $f3 = f(a3)$, also

plot $t1 - ((t2 - f2) + (t3 - f3))/2$ vs $a1$, $t2 - ((t3 - f3) + (t1 - f1))/2$ vs $a2$ and $t3 - ((t1 - f1) + (t2 - f2))/2$ vs $a3$. And we got the new three slewing curves $f'(a1), f'(a2), f'(a3)$. For the third step, $f1 = f'(a1), f2 = f'(a2), f3 = f'(a3)$, also plot $t1 - ((t2 - f2) + (t3 - f3))/2$ vs $a1$, $t2 - ((t3 - f3) + (t1 - f1))/2$ vs $a2$ and $t3 - ((t1 - f1) + (t2 - f2))/2$ vs $a3$. And we got another new three slewing curves $f''(a1), f''(a2), f''(a3)$. And so on and so forth till the resolution of $t1 - f1 - ((t2 - f2) + (t3 - f3))/2, t2 - f2 - ((t3 - f3) + (t1 - f1))/2$ and $t3 - f3 - ((t1 - f1) + (t2 - f2))/2$ converged. The looping method is to subtract the correlation of different pVPD tubes in the same direction. The function for the slewing correction we use is $y = par[0] + par[1]/\sqrt{x} + par[2]/x + par[3] \times x$. In Figure 3.3, the left plot shows the pVPD2 slewing plot and the right plot shows that the timing is independent on the ADC value after the slewing correction.

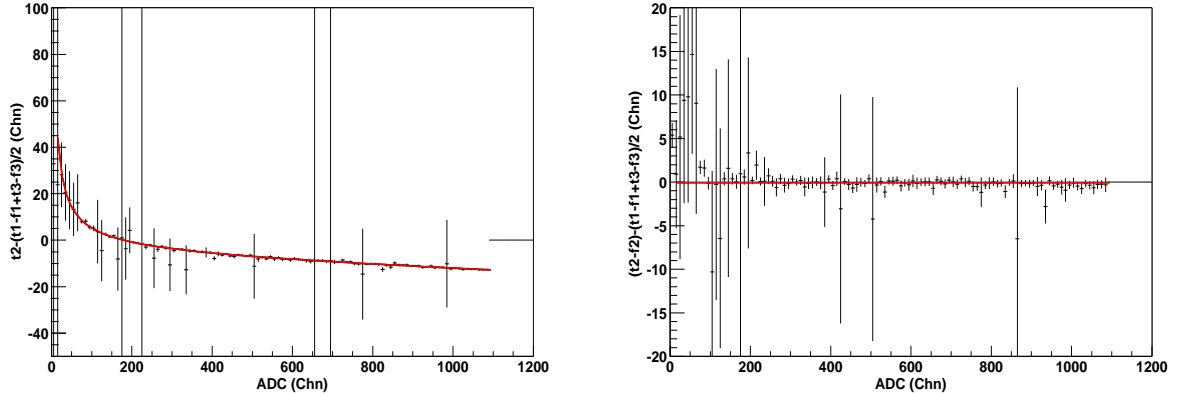


Figure 3.3: pVPD slewing correction.

After the slewing correction, we got the corrected timing of east pVPD and west pVPD. For each side, the timing difference should be shifted to zero. That's to say the mean value in the distribution of $t1 - f1 - (t2 - f2)$ and $t1 - f1 - (t3 - f3)$ were shifted to zero. Also we need to correct for the effect caused by the different numbers of fired pVPD in different events. What we did was shifting the mean value of the distribution of $(\sum te)/Ne - (\sum tw)/Nw - 2 \times Vz/c$ to zero, where the $\sum te$, $\sum tw$ means the sum of the corrected timing of east fired pVPD and west fired pVPD respectively, Ne, Nw means the number of east fired pVPD and west fired pVPD, Vz

is the z value of primary vertex of the event, and c is the light velocity.

TOFr calibration

After the slewing correction for pVPD, we use this variable as our start timing:

$$T_{start} = \frac{\sum_{i=1}^{N_e} te + \sum_{i=1}^{N_w} tw - (N_e - N_w) \times Vz/c}{N_e + N_w} \quad (3.1)$$

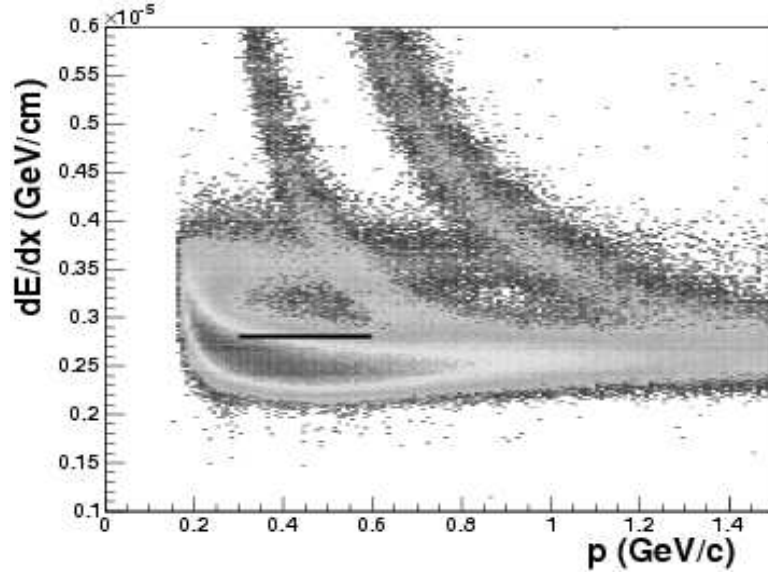


Figure 3.4: dE/dx vs p plot from d+Au collisions. The line represents that $dE/dx = 0.028 \times 10^{-4}$ GeV/cm in this momentum range $0.3 < p < 0.6$ GeV/c.

The difference between TOFr timing T_{tofr} and start timing T_{start} is our time of flight $tof = T_{tofr} - T_{start}$. To calibrate the tof , the pure pion sample was chosen by selecting the particle energy loss dE/dx in TPC at $dE/dx < 0.028 \times 10^{-4}$ GeV/cm in the momentum range $0.3 < p < 0.6$ GeV/c. Figure 3.4 shows dE/dx vs p plot from d+Au collisions. Firstly the so called T_0 correction was done due to the different cable lengths for different read-out channels, which was done by shifting the mean value of the distribution of $tof - T_\pi$ to zero channel by channel, where T_π is the calculation timing assuming the particle was pion particle. Secondly, the slewing correction due to correlation between timing and signal amplitude of the electronics was done by

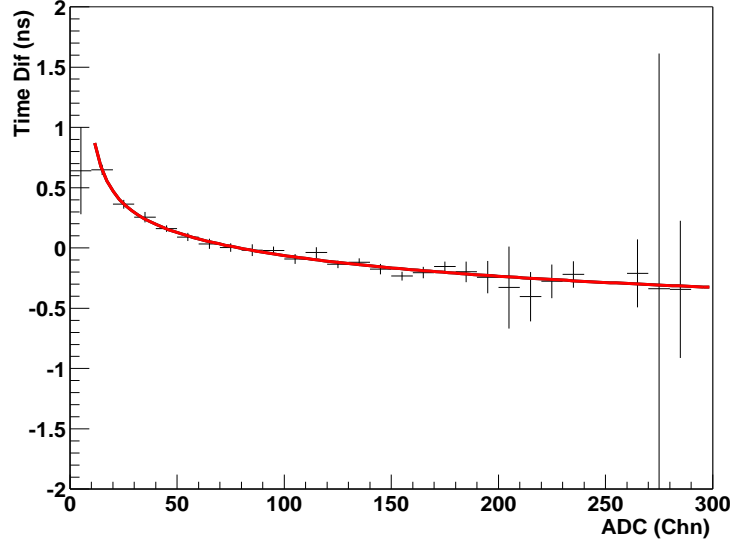


Figure 3.5: The slewing correction.

getting the curve of $tof' - T_\pi$ vs adc for each channel, where the tof' was the time of flight after the T_0 correction and adc was the ADC value of TOFr. The slewing curve is like the plot shown in Figure 3.5. The function of the slewing correction is $y = par[0] + par[1]/\sqrt{x} + par[2]/x + par[3]/\sqrt{x}/x + par[4]/x/x$.

The z position correction was also done since the different hit positions on the read-out strip will generate different transmission timing. This was done by getting the function of $tof'' - T_\pi$ versus Z_{local} , where the tof'' is the time of flight after the T_0 and slewing correction, and Z_{local} is the the hit local z position of the TOFr. The function for the z position correction is $y = \sum_{i=0}^7 (par[i] \times x^i)$. The z position correction for all the channels is shown in Figure 3.6. After the z position was done, the calibration for TOFr was finished. The overall resolution of TOFr was 120 ps and 160 ps in d+Au and p+p collisions respectively, where the effective timing resolution of the pVPDs was 85 ps and 140 ps, respectively. Figure 3.7 shows the overall resolution of TOFr in d+Au and p+p collisions.

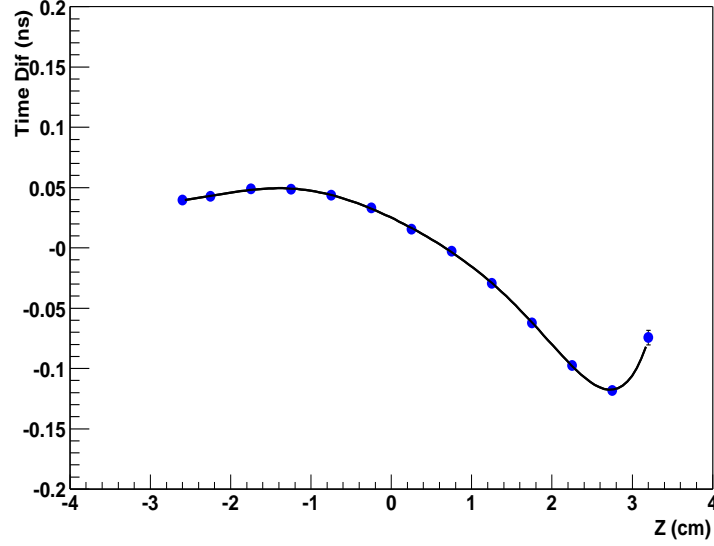


Figure 3.6: The z position correction.

3.3 Raw yield

From the timing information t from TOFr after the calibration and the pathlength L from TPC, the velocity β of the particle can be easily got by $\beta = L/t/c$. Figure 3.8 shows $1/\beta$ from TOFr measurement as a function of momentum (p) calculated from TPC tracking in TOFr triggered d+Au collisions. The raw yields of π^\pm , K^\pm , p and \bar{p} are obtained from Gaussian fits to the distributions in $m^2 = p^2(1/\beta^2 - 1)$ in each p_T bin.

3.3.1 π raw yield extraction

For π^\pm , the rapidity range is $-0.5 < y_\pi < 0.$. After $|N_{\sigma\pi}| < 2$ was required, the mass squared $m^2 = p^2(1/\beta^2 - 1)$ distributions in different p_T bin in d+Au minimum-bias collisions are shown in Figure 3.16 and Figure 3.17. At $p_T < 0.8$ GeV/c, the single Gaussian function was used to fit the distribution of m^2 to get the raw yield. At the same time, the counting result by counting the track number at the range $-0.1 < m^2 < 0.1$ (GeV/c^2)² was also used to compare with the raw yield from the fitting method. The difference between them was found in one sigma range. The raw

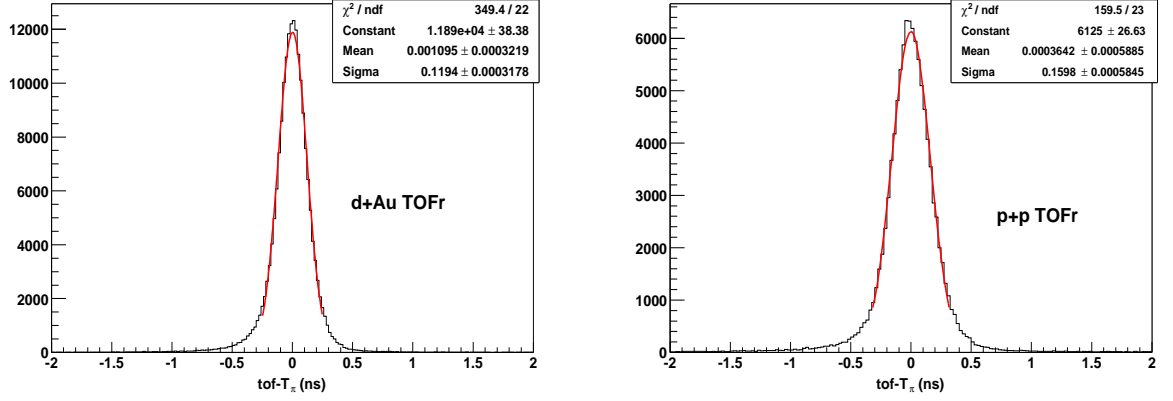


Figure 3.7: The overall timing resolution after the calibration.

yield we quote is from the fitting method. At $p_T > 0.8$ GeV/c, the double Gaussian function was used to extract the raw yield. The raw signals in each P_T bin are shown in Table 3.3 and Table 3.4. Also shown in the tables are those in centrality selected d+Au collisions and minimum-bias p+p collisions.

3.3.2 K raw yield extraction

For K^\pm , the rapidity range is $-0.5 < y_K < 0$. After $|N_{\sigma K}| < 2$ was required, the mass squared $m^2 = p^2(1/\beta^2 - 1)$ distributions in different p_T bin in d+Au minimum-bias collisions are shown in Figure 3.18 and Figure 3.19. At $p_T < 0.8$ GeV/c, the single Gaussian function was used to fit the distribution of m^2 to get the raw yield. At the same time, the counting result by counting the track number at the range $0.16 < m^2 < 0.36$ $(\text{GeV}/c^2)^2$ was also used to compare with the raw yield from the fitting method. The difference between them was found in one sigma range. The raw yield we quote is from the fitting method. At $p_T > 0.8$ GeV/c, the double Gaussian function was used to extract the raw yield. The raw signals in each P_T bin are shown in Table 3.5 and Table 3.6. Also shown in the tables are those in centrality selected d+Au collisions and minimum-bias p+p collisions.

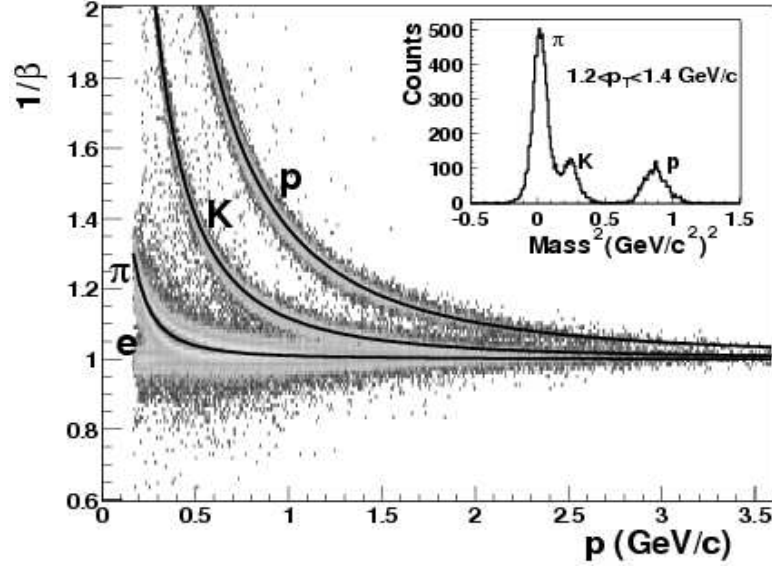


Figure 3.8: $1/\beta$ vs. momentum for π^\pm , K^\pm , and $p(\bar{p})$ from 200 GeV d+Au collisions. Separations between pions and kaons, kaons and protons are achieved up to $p_T \simeq 1.6$ and 3.0 GeV/c, respectively. The insert shows $m^2 = p^2(1/\beta^2 - 1)$ for $1.2 < p_T < 1.4$ GeV/c. Clear separation of π , K and p is seen.

3.3.3 p and \bar{p} raw yield extraction

For \bar{p} , the rapidity range is $-0.5 < y_{\bar{p}} < 0$. After $|N_{\sigma p}| < 2$ was required, the mass squared $m^2 = p^2(1/\beta^2 - 1)$ distributions in different p_T bin in d+Au minimum-bias collisions are shown in Figure 3.21. At $p_T < 1.6$ GeV/c, the single Gaussian function was used to fit the distribution of m^2 to get the raw yield. At the same time, the counting result by counting the track number at the range $0.64 < m^2 < 1.44$ $(\text{GeV}/c^2)^2$ was also used to compare with the raw yield from the fitting method. The difference between them was found in one sigma range. The raw yield we quote is from the fitting method. At $p_T > 1.6$ GeV/c, the double Gaussian function was used to extract the raw yield. The raw signals in each P_T bin are shown in Table 3.8. For the p , the raw yield extraction method is the same as \bar{p} except that at $p_T < 1.6$ GeV/c, we use the method $Np = Np_{dca < 1.0\text{ cm}} \times (N\bar{p}_{dca < 3.0\text{ cm}}/N\bar{p}_{dca < 1.0\text{ cm}})$ to reject the background, where Np and $N\bar{p}$ are the number of the p and \bar{p} tracks individually, and $N\bar{p}_{dca < 1.0\text{ cm}}/N\bar{p}_{dca < 3.0\text{ cm}}$ is the ratio of \bar{p} tracks at $dca < 1.0$ cm over those at $dca < 3.0$

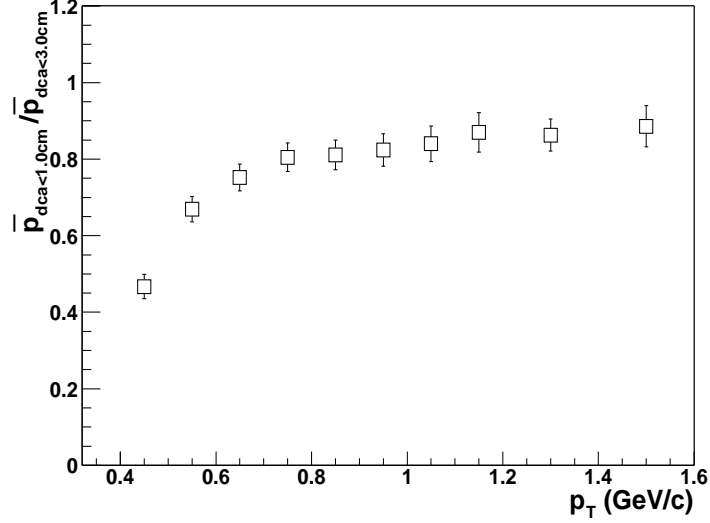


Figure 3.9: the ratio of \bar{p} at $dca < 1.0$ cm over \bar{p} at $dca < 3.0$ cm.

cm. In Figure 3.20, the first 10 p_T bins are for $dca < 1.0$ cm, the last 4 p_T bins are for $dca < 3.0$ cm. Figure 3.9 shows the ratio of \bar{p} tracks at $dca < 1.0$ cm over those at $dca < 3.0$ cm. After this correction of $Np = Np_{dca<1.cm} \times (N\bar{p}_{dca<3.cm}/N\bar{p}_{dca<1.cm})$, the p raw signals in each P_T bin are shown in Table 3.7.

3.4 Efficiency and acceptance correction

Acceptance and efficiency were studied by Monte Carlo simulations and by matching TPC track and TOFr hits in real data. TPC tracking efficiency was studied by Monte Carlo simulations. The simulated π^\pm , K^\pm , p and \bar{p} are generated using a flat p_T and a flat y distribution and pass through GSTAR [82] (the framework software package to run the STAR detector simulation using GEANT [84, 85]) and TRS (the TPC Response Simulator [82]). The simulated π^\pm , K^\pm , p and \bar{p} are then combined with a real raw event and we call this combined event a simulated event. This simulated event is then passed through the standard STAR reconstruction chain and we call this event after reconstruction a reconstructed event. The reconstructed information of those particles in the reconstructed event is then associated with the Monte-Carlo

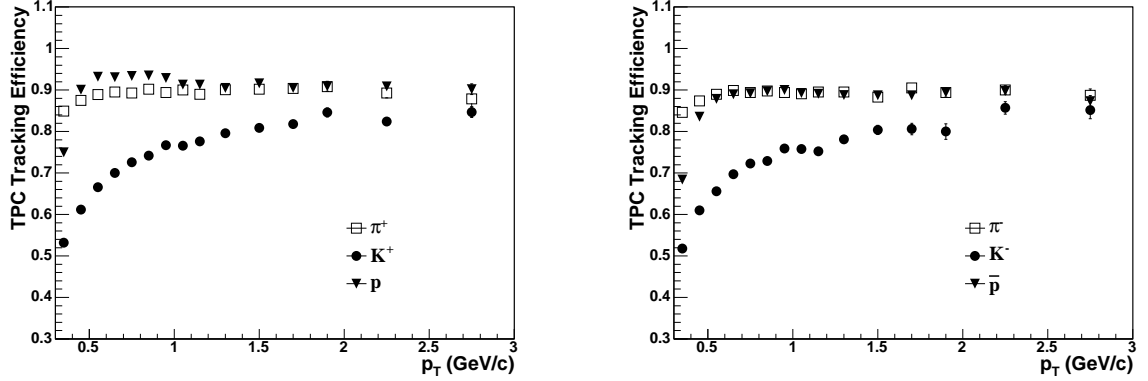


Figure 3.10: TPC reconstruction efficiency of π^\pm , K^\pm , p and \bar{p} as a function of p_T . The left plot for charged plus particle and the right for charged minus particle.

information in the simulated event. And then we get the total number of simulated π^\pm , K^\pm , p and \bar{p} from simulated events in a certain transverse momentum bin. Also we can get the total number of associated tracks in the reconstructed events in this transverse momentum bin [81]. In the end, take the ratio of the number of associated π^\pm , K^\pm , p and \bar{p} over the number of simulated π^\pm , K^\pm , p and \bar{p} and this ratio is the TPC reconstruction efficiency for a certain transverse momentum bin in the mid-rapidity range. Figure 3.10 shows the TPC reconstruction efficiency of π^\pm , K^\pm , p and \bar{p} as a function of p_T .

The Matching Efficiency from TPC to TOFr were studied in real data, and the formula are

$$Eff_{Match} = \frac{TofrMatchedTracks/dAuTOFrEvents}{(MinBiasTracks/MinBiasEvents)_{pVPD} \times factor1 \times factor2} \quad (3.2)$$

where the $TofrMatchedTracks/dAuTOFrEvents$ is the number of TOFr matched tracks per dAuTOFr trigger event, $(MinBiasTracks/MinBiasEvents)_{pVPD}$ is the number of minimum-bias tracks per minimum-bias event by requiring the pVPD to fire, $factor1$ is the enhancement factor of dAuTOFr trigger, and $factor2$ is the other factors such as the TOFr trip factor. The Eff_{Match} includes the detector response efficiency. Figure 3.11 shows the matching efficiency of different particle species including the detector response versus p_T . The detector response efficiency, including the material absorption and scattering effect between TPC and TOFr, as

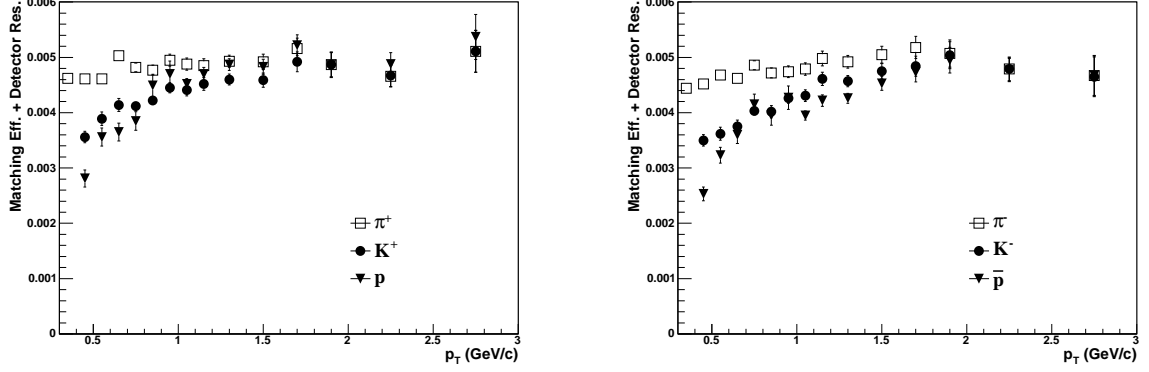


Figure 3.11: Matching efficiency from TOFr to TPC of π^\pm , K^\pm , p and \bar{p} as a function of p_T , including detector response. The left plot for charged plus particle and the right for charged minus particle.

a function of p_T is shown in Figure 3.12, which is around 90% at $p_T > 0.3$ GeV/c. After the material absorption and scattering effect correction, the detector response efficiency is around 95%.

3.5 Background correction

Weak-decay feeddown (e.g. $K_s^0 \rightarrow \pi^+\pi^-$) to pions is $\sim 12\%$ at low p_T and $\sim 5\%$ at high p_T , and was corrected for using PYTHIA [76] and HIJING [77] simulations, as shown in Figure 3.13. For π spectra, the μ misidentification was also corrected for, which is also shown in Figure 3.13.

Inclusive p and \bar{p} production is presented without hyperon feeddown correction. p and \bar{p} from hyperon decays have the same detection efficiency as primary p and \bar{p} [79] and contribute about 20% to the inclusive p and \bar{p} yield, as estimated from the simulation. However, for p , there is still some scattering contribution which comes from the beam pipe interaction after the cut of $dca < 1.0$ cm. Figure 3.14 shows the contribution of scattering effect for proton when we cut $dca < 1.0$ cm. The correction is done at $p_T < 1.1$ GeV/c and negligible at higher p_T .

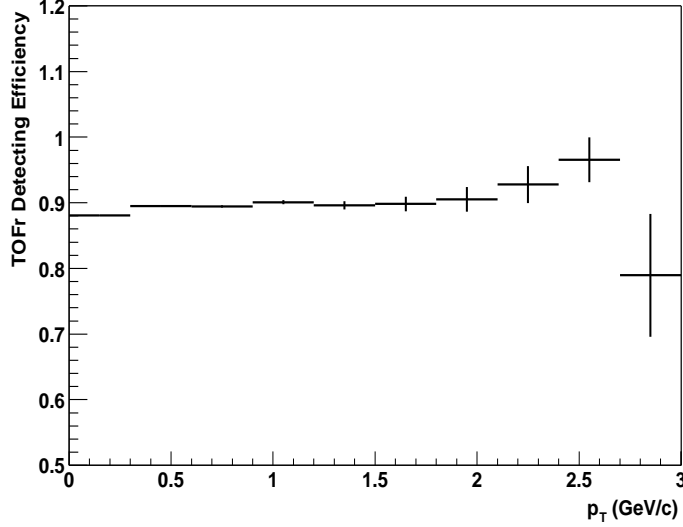


Figure 3.12: The TOFr response efficiency as a function of p_T .

3.6 Energy loss correction

The energy loss effect due to the interaction with the detector material was also corrected for. This was studied by simulation. Figure 3.15 shows the momentum and transverse momentum correction for energy loss effect. At $p_T > 0.35$ GeV/c, for π , the energy loss effect is negligible while for kaon and proton, the energy loss correction is non-negligible at lower p_T and negligible at higher p_T . The correction was done by shifting the position of p_T in the p_T spectra.

3.7 Normalization

The efficiency including vertex efficiency and trigger efficiency is 91% in d+Au minimum-bias collisions and 85% in p+p and 40-100% d+Au collisions. In 0%-20% and 20%-40% d+Au collisions, the efficiency is 100%. Since the statistic of p+p minimum-bias events in run 3 is not good enough for us to get very precise enhancement factor and N_{ch} bias factor. We compare the π spectra in the first 5 p_T bin with those from the paper [35] and get the additional normalization factor for p+p collisions.

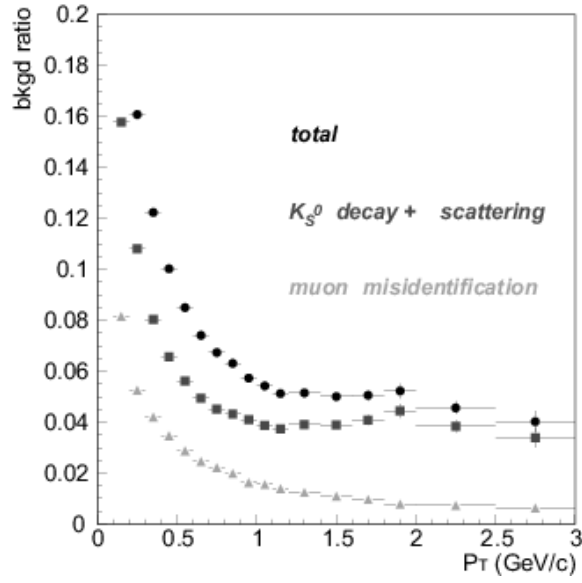


Figure 3.13: π background contribution as a function of p_T . The circled symbols represent the total π background contribution including feed-down and μ misidentification. The squared and triangled symbols represent the week-decay and μ misidentification contributions individually.

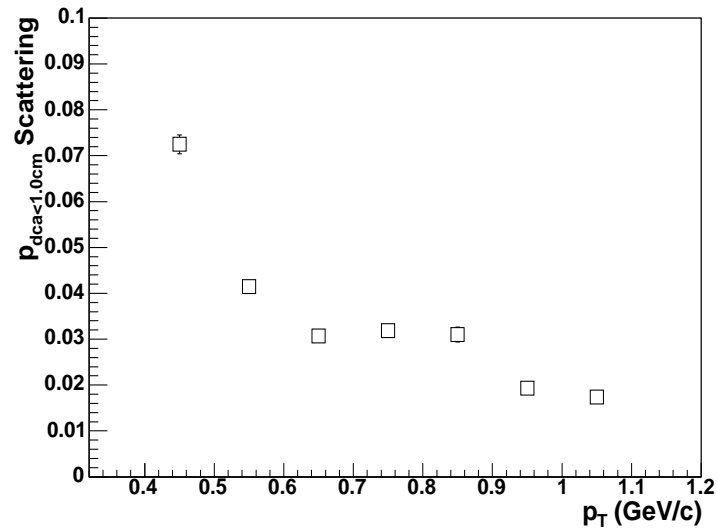


Figure 3.14: The p scattering effect contribution when we cut $dca < 1.0$ cm.

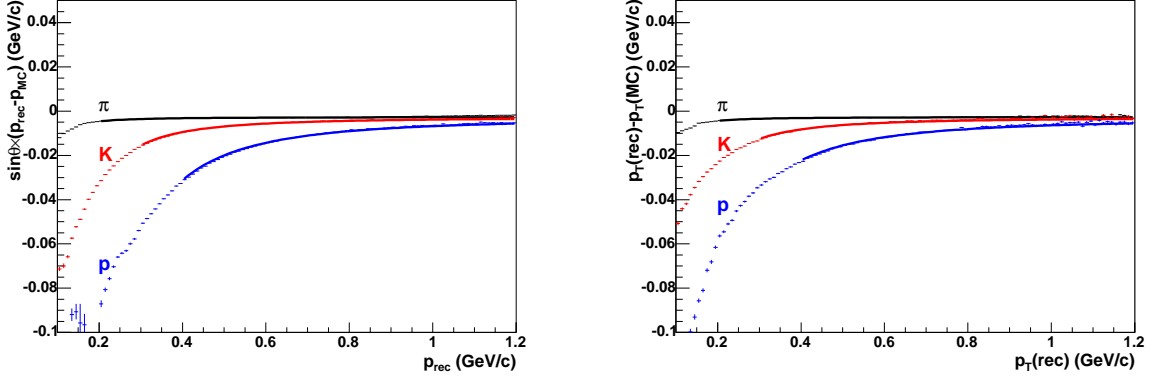


Figure 3.15: (left) p energy loss correction of different particle species as a function of p . p_{rec} is the reconstructed momentum before the energy loss correction, p_{MC} is the momentum after energy loss correction from simulation, θ is the angle between the reconstructed momentum and beam line. (right) p_T energy loss correction of different particle species as a function of p_T . $p_T(rec)$ is the reconstructed transverse momentum before the energy loss correction, $p_T(MC)$ is the transverse momentum after energy loss correction from simulation.

p_T (GeV/c)	d+Au Trigger	0%-20%	20%-40%	40%-100%	p+p
0.3-0.4	$2.929e+04 \pm 171.4$	9219 ± 96.21	8735 ± 93.6	8604 ± 92.84	$1.806e+04 \pm 134.4$
0.4-0.5	$2.185e+04 \pm 147.8$	6894 ± 83.03	6657 ± 81.59	6325 ± 79.53	$1.274e+04 \pm 114.3$
0.5-0.6	$1.592e+04 \pm 126.2$	5162 ± 71.85	4901 ± 70.3	4534 ± 67.34	9180 ± 95.81
0.6-0.7	$1.166e+04 \pm 108$	3832 ± 62.19	3556 ± 59.64	3311 ± 57.54	6531 ± 80.82
0.7-0.8	8556 ± 92.5	2909 ± 53.93	2628 ± 51.26	2368 ± 48.67	4447 ± 66.74
0.8-0.9	6198 ± 78.86	2099 ± 45.85	1936 ± 44.33	1693 ± 41.17	2973 ± 54.57
0.9-1	4520 ± 67.25	1487 ± 38.57	1361 ± 36.9	1276 ± 35.74	2132 ± 46.31
1-1.1	3312 ± 57.61	1147 ± 33.9	1033 ± 32.17	845.9 ± 29.15	1386 ± 37.71
1.1-1.2	2406 ± 49.35	788.6 ± 28.19	752.5 ± 27.58	652.7 ± 25.7	959.2 ± 31.93
1.2-1.4	3227 ± 58.17	1132 ± 34.28	934.4 ± 30.98	831.5 ± 29.82	1183 ± 40.11
1.4-1.6	1756 ± 45.2	573.7 ± 26.2	543.7 ± 24	412.8 ± 21.83	625.5 ± 30.16
1.6-1.8	1046 ± 39	337.9 ± 20.42	309.8 ± 18.62	234 ± 16.58	364.5 ± 32.64

Table 3.3: π^+ raw signal table in minimum-bias, centrality selected d+Au collisions and minimum-bias p+p collisions.

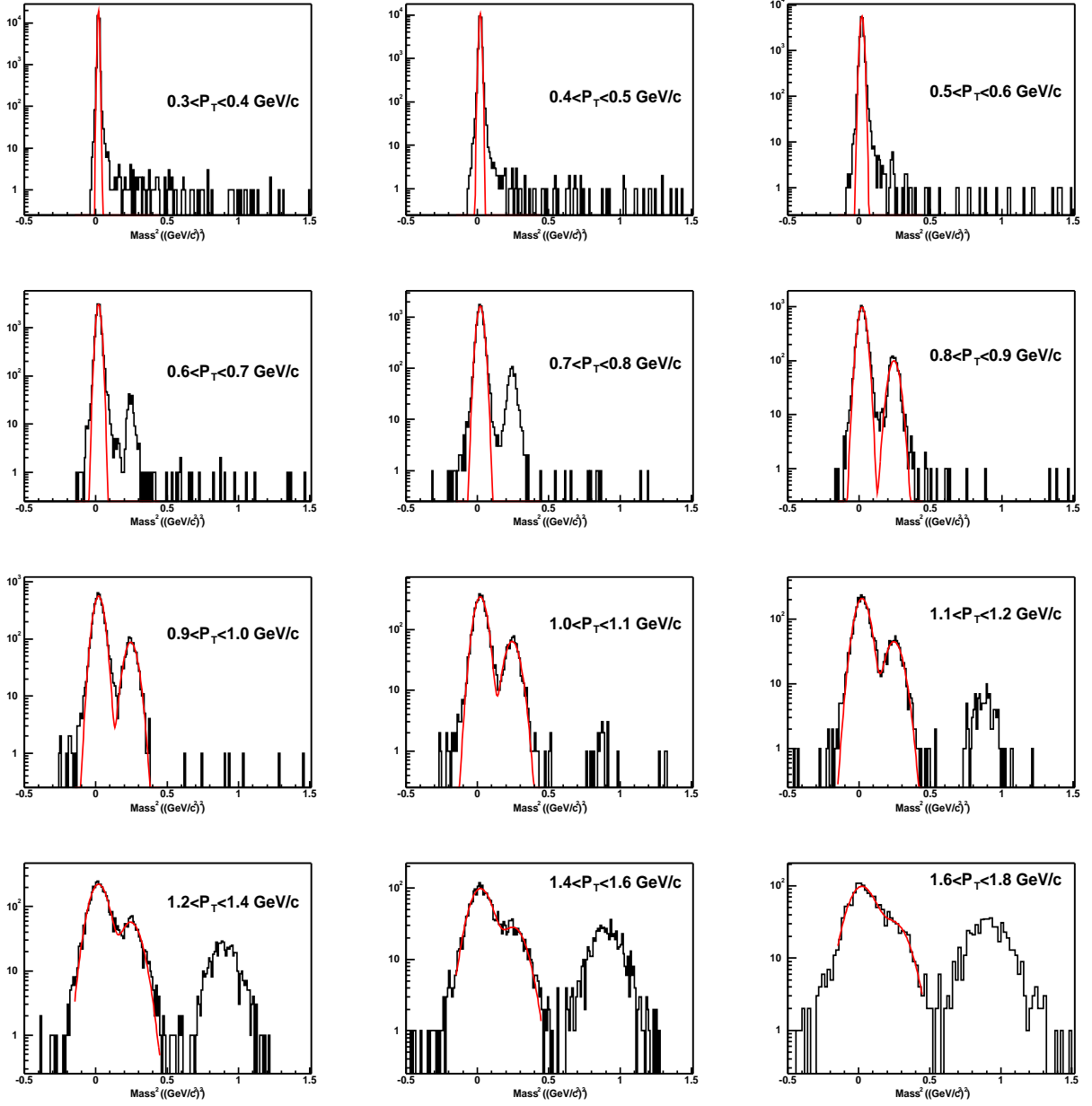


Figure 3.16: π^+ raw yields versus mass squared distribution. The histograms are our data. The curves are Gaussian fits.

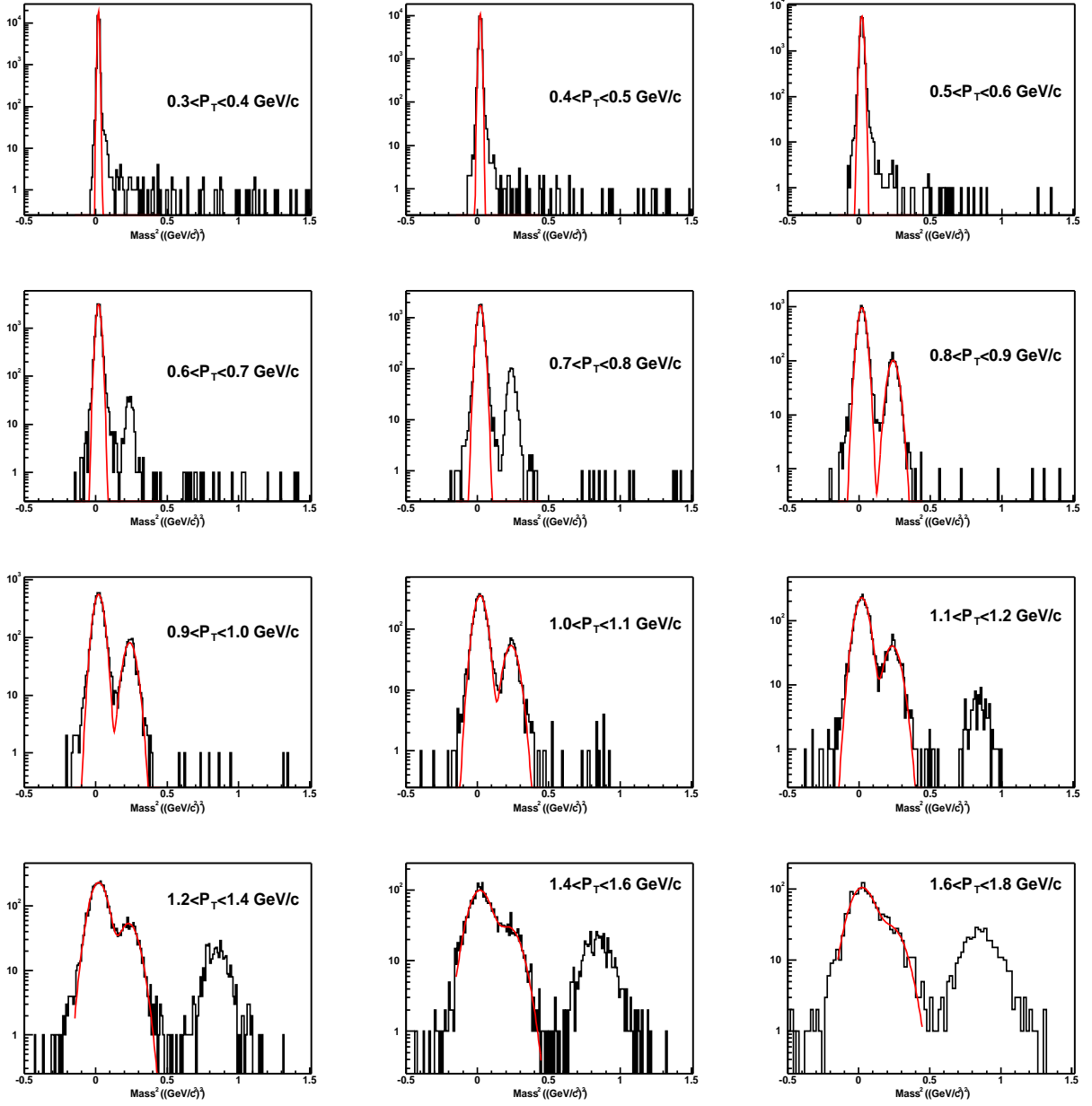


Figure 3.17: π^- raw yields versus mass squared distribution. The histograms are our data. The curves are Gaussian fits.

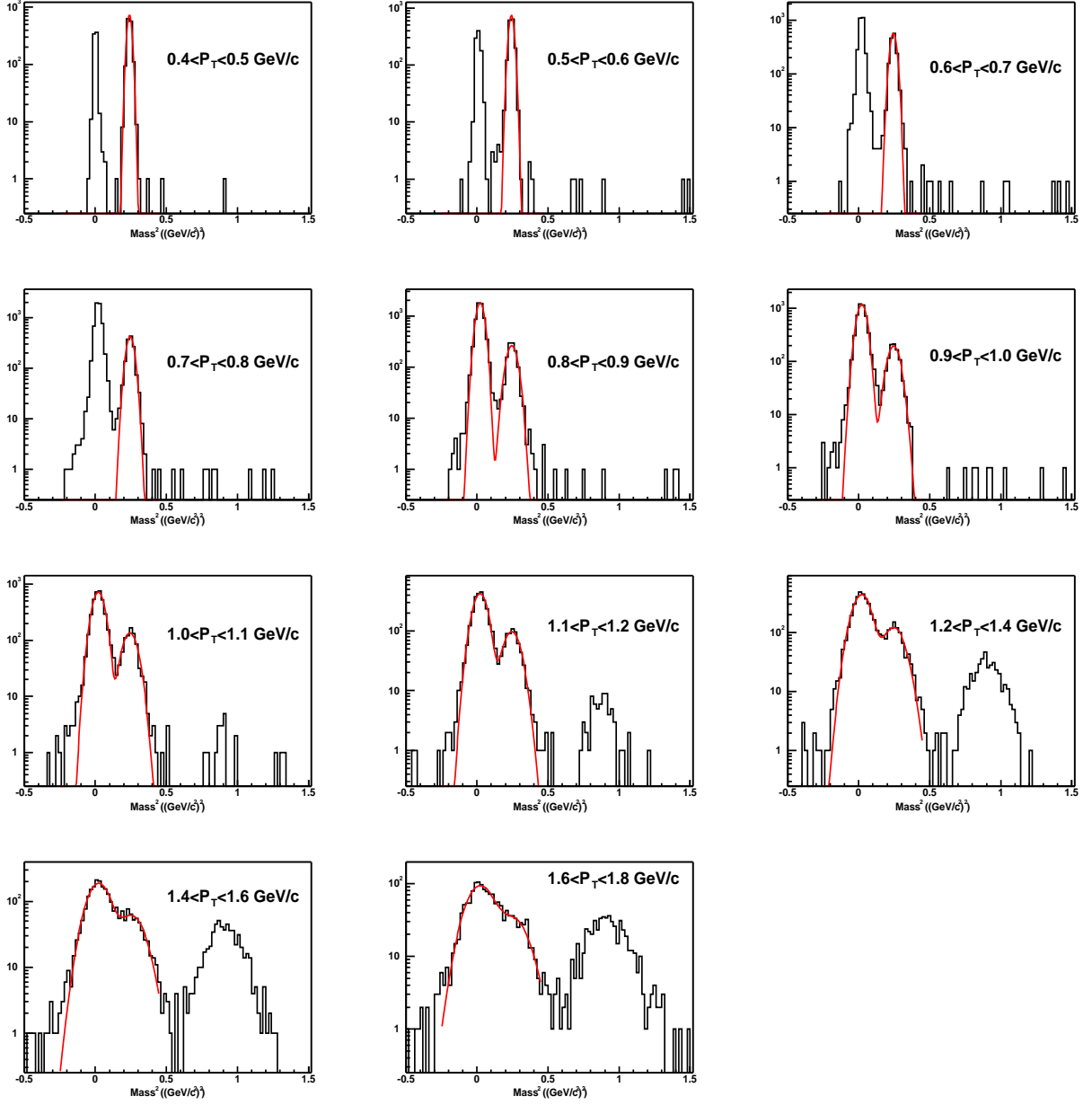


Figure 3.18: K^+ raw yields versus mass squared distribution. The histograms are our data. The curves are Gaussian fits.

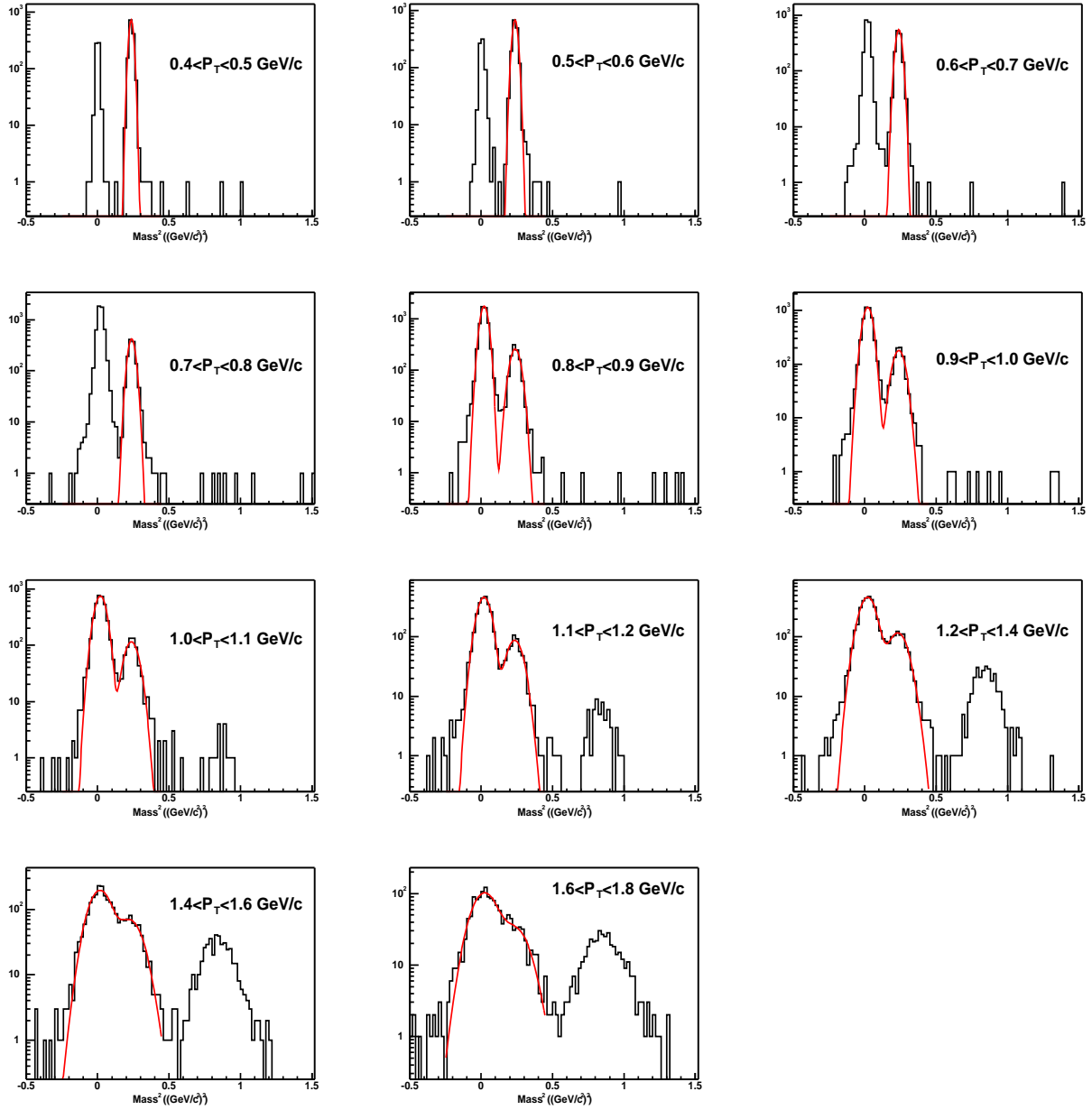


Figure 3.19: K^- raw yields versus mass squared distribution. The histograms are our data. The curves are Gaussian fits.

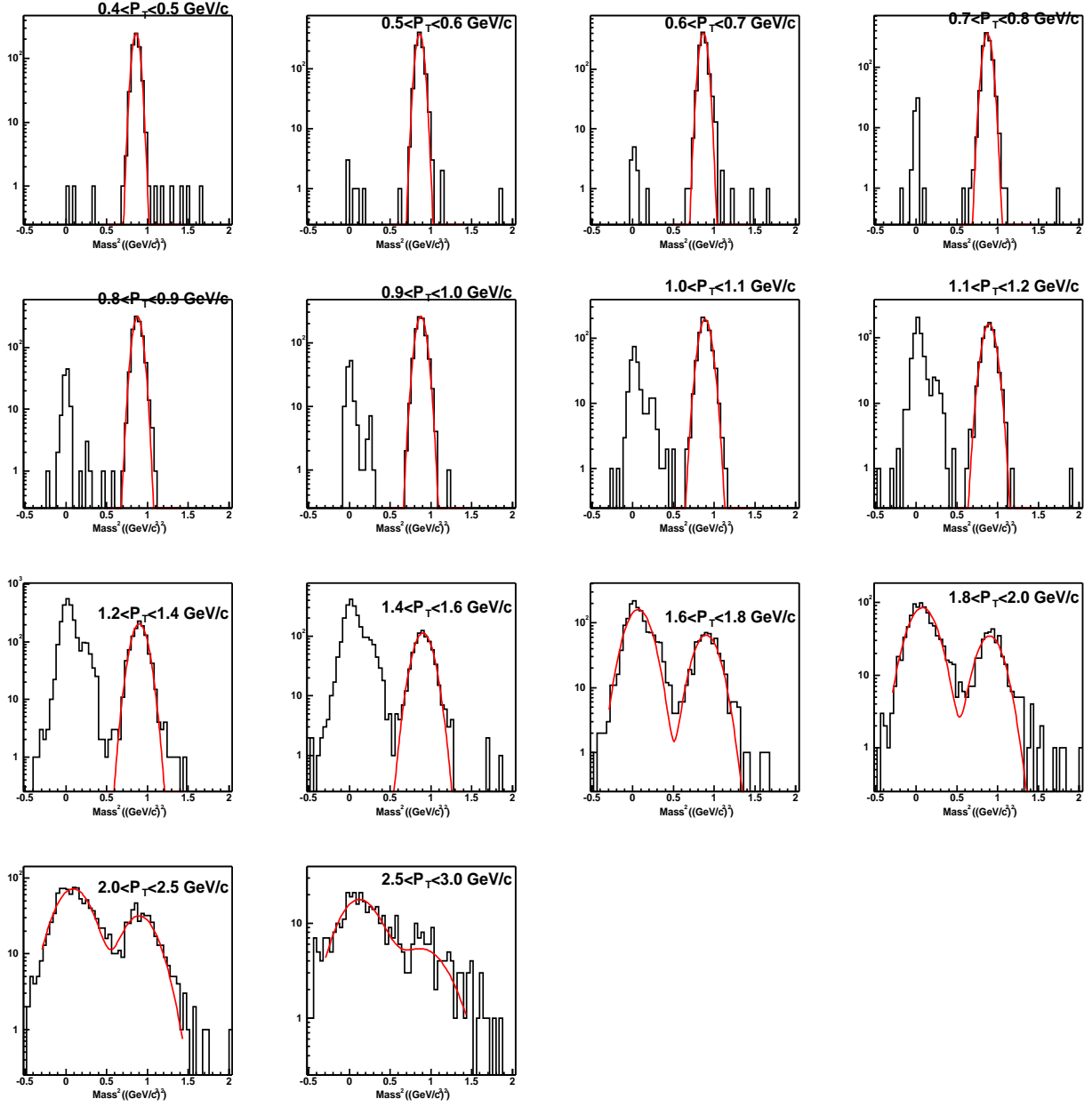


Figure 3.20: p raw yields versus mass squared distribution. The histograms are our data. The curves are Gaussian fits.

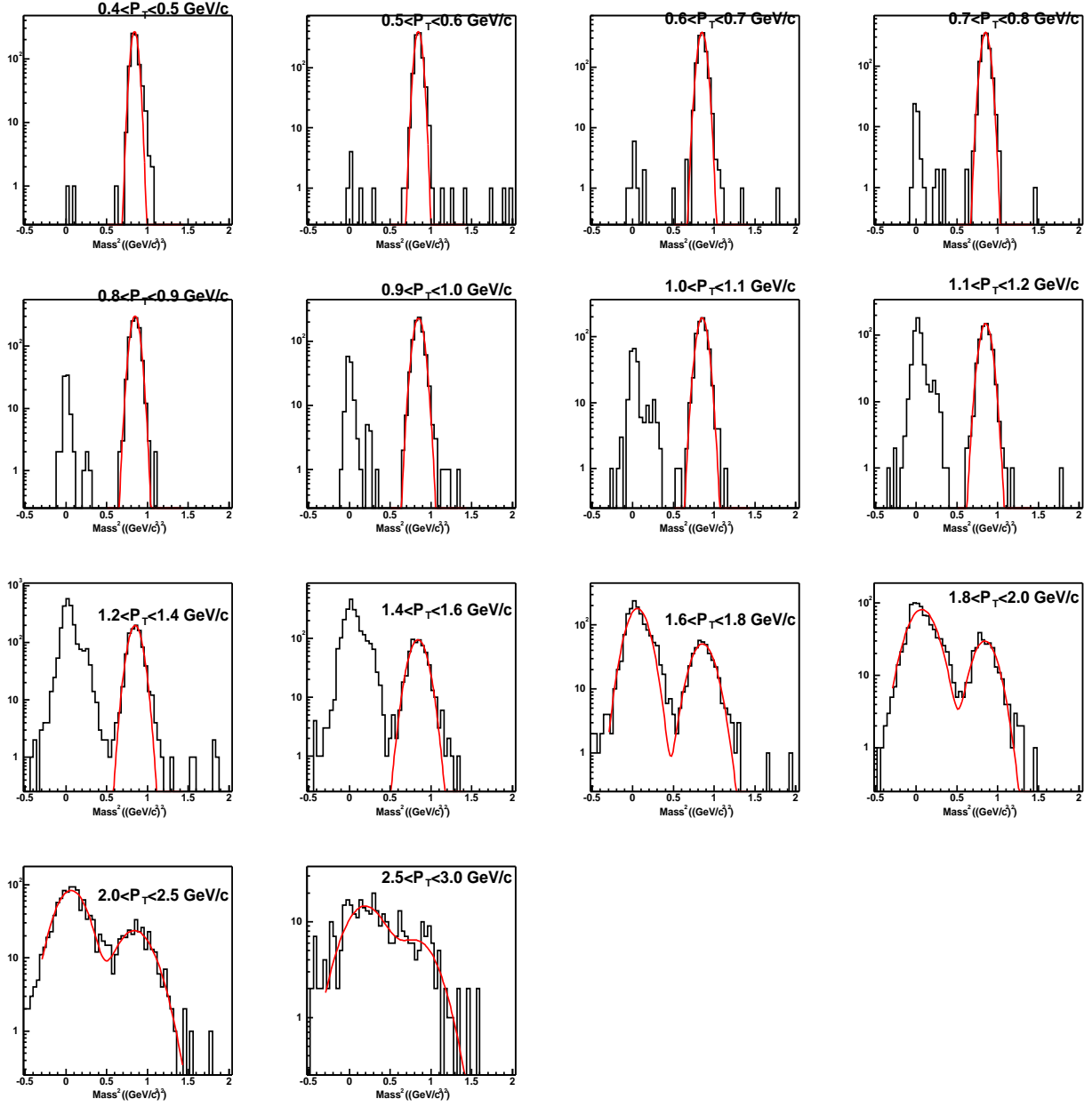


Figure 3.21: \bar{p} raw yields versus mass squared distribution. The histograms are our data. The curves are Gaussian fits.

p_T (GeV/c)	d+Au Trigger	0%-20%	20%-40%	40%-100%	p+p
0.3-0.4	$2.861e + 04 \pm 169.4$	8922 ± 94.66	8507 ± 92.38	8519 ± 92.4	$1.715e + 04 \pm 131$
0.4-0.5	$2.139e + 04 \pm 146.3$	6805 ± 82.49	6458 ± 80.35	6306 ± 79.41	$1.28e + 04 \pm 113.1$
0.5-0.6	$1.611e + 04 \pm 126.9$	5327 ± 72.98	4873 ± 69.8	4605 ± 67.86	9189 ± 95.86
0.6-0.7	$1.166e + 04 \pm 108$	3831 ± 61.9	3550 ± 59.5	3355 ± 57.92	6362 ± 79.69
0.7-0.8	8447 ± 91.91	2837 ± 53.64	2540 ± 50.4	2387 ± 48.86	4154 ± 64.5
0.8-0.9	5950 ± 77.17	2076 ± 45.61	1780 ± 42.2	1646 ± 40.68	2899 ± 53.87
0.9-1	4284 ± 65.46	1446 ± 38.03	1317 ± 36.31	1171 ± 34.29	1924 ± 44.01
1-1.1	3296 ± 57.47	1123 ± 33.55	1014 ± 31.9	897.5 ± 30.02	1372 ± 37.77
1.1-1.2	2464 ± 49.88	812.4 ± 28.58	762.4 ± 27.69	650.8 ± 25.72	1005 ± 33.16
1.2-1.4	3136 ± 57.28	1027 ± 32.54	972.9 ± 31.71	828.8 ± 29.65	1243 ± 39.78
1.4-1.6	1716 ± 45.79	612.5 ± 25.87	539.3 ± 25.67	422.7 ± 24.22	603.8 ± 30.49
1.6-1.8	1033 ± 39.74	375.3 ± 21.21	306.1 ± 19.59	239.9 ± 48.55	337.1 ± 28.82

Table 3.4: π^- raw signal table in minimum-bias, centrality selected d+Au collisions and minimum-bias p+p collisions.

p_T (GeV/c)	d+Au Trigger	0%-20%	20%-40%	40%-100%	p+p
0.4-0.5	1410 ± 37.54	417.2 ± 20.44	420.9 ± 20.52	354.9 ± 18.84	753.2 ± 27.44
0.5-0.6	1588 ± 39.85	486.3 ± 22.06	461 ± 21.48	435 ± 20.87	729.3 ± 27
0.6-0.7	1499 ± 38.71	465.9 ± 21.59	445.5 ± 21.17	395 ± 19.87	710.1 ± 26.65
0.7-0.8	1346 ± 36.69	423.9 ± 20.59	419.8 ± 20.62	335.7 ± 18.32	579 ± 24.06
0.8-0.9	1105 ± 33.59	369.7 ± 19.3	317.9 ± 18.43	282.5 ± 17.03	496.2 ± 22.44
0.9-1	969.1 ± 31.19	283.9 ± 16.86	305.1 ± 17.52	258.7 ± 16.23	381.2 ± 19.87
1-1.1	799.3 ± 28.41	278.6 ± 16.79	224 ± 15.04	192.3 ± 14.04	301.5 ± 18.39
1.1-1.2	656.7 ± 26.24	199.1 ± 14.33	186.2 ± 14	155.7 ± 12.94	267.8 ± 18.71
1.2-1.4	1013 ± 34.43	335 ± 19.51	283.1 ± 17.71	234.1 ± 17.68	421.1 ± 29.14
1.4-1.6	605.9 ± 30.14	191.1 ± 17.77	174.1 ± 14.77	148.8 ± 15.48	238.8 ± 13.97
1.6-1.8	382.9 ± 28.9	---	---	---	---

Table 3.5: K^+ raw signal table in minimum-bias, centrality selected d+Au collisions and minimum-bias p+p collisions.

p_T (GeV/c)	d+Au Trigger	0%-20%	20%-40%	40%-100%	p+p
0.4-0.5	1341 ± 36.62	411.6 ± 20.29	367.6 ± 19.19	378 ± 19.44	682.6 ± 26.13
0.5-0.6	1498 ± 38.7	460 ± 21.45	411.5 ± 20.32	420.5 ± 20.51	740.7 ± 27.21
0.6-0.7	1410 ± 37.55	436.2 ± 20.89	398.4 ± 19.97	361.9 ± 19.02	616.8 ± 24.83
0.7-0.8	1207 ± 34.74	366 ± 19.14	349.7 ± 18.7	350 ± 18.75	557.4 ± 23.61
0.8-0.9	1057 ± 32.66	317.4 ± 18.12	332.4 ± 18.37	268.2 ± 16.66	432.9 ± 20.93
0.9-1	863.7 ± 29.42	256.9 ± 16.09	267.2 ± 16.43	223.8 ± 15.03	368.9 ± 19.59
1-1.1	635.2 ± 25.35	198.2 ± 14.35	183.1 ± 13.61	187.9 ± 13.88	320.4 ± 19.42
1.1-1.2	543 ± 23.92	166.4 ± 13.14	143 ± 12.22	154.1 ± 12.89	248.5 ± 18.84
1.2-1.4	895 ± 32.45	302.1 ± 18.3	258 ± 17.06	206.7 ± 16.17	377.1 ± 26.67
1.4-1.6	645.5 ± 31.61	202.4 ± 16.78	141 ± 15.58	166.6 ± 17.87	237.6 ± 20.52
1.6-1.8	351.3 ± 29.79	---	---	---	---

Table 3.6: K^- raw signal table in minimum-bias, centrality selected d+Au collisions and minimum-bias p+p collisions.

p_T (GeV/c)	d+Au Trigger	0%-20%	20%-40%	40%-100%	p+p
0.4-0.5	1377 ± 107.5	412.6 ± 40.73	403.5 ± 40.11	422.7 ± 41.42	657.5 ± 64.94
0.5-0.6	1527 ± 89.71	492.2 ± 36.58	428.6 ± 33.09	424.8 ± 32.89	752.6 ± 59.91
0.6-0.7	1456 ± 80.28	437.9 ± 31.47	420 ± 30.56	401.3 ± 29.6	704.9 ± 54.1
0.7-0.8	1336 ± 73.68	410.6 ± 29.43	387.9 ± 28.28	385 ± 28.14	670 ± 55.36
0.8-0.9	1278 ± 72.45	387.6 ± 28.57	371.4 ± 27.72	312 ± 24.57	498.8 ± 45.17
0.9-1	1124 ± 68.87	349.1 ± 27.39	322.1 ± 25.87	288.1 ± 23.94	448.3 ± 44.89
1-1.1	954.5 ± 62.39	288.2 ± 24.38	285.3 ± 24.23	265.9 ± 23.11	365 ± 40.02
1.1-1.2	832.1 ± 58.34	257.2 ± 23.06	245.4 ± 22.25	213.3 ± 20.25	273.8 ± 34.08
1.2-1.4	1268 ± 72.57	441.9 ± 31.19	362.6 ± 27.1	320.2 ± 24.77	393.8 ± 41.64
1.4-1.6	806.8 ± 57.58	306.9 ± 26.38	221.5 ± 20.77	190.8 ± 18.71	210.3 ± 31.59
1.6-1.8	540.8 ± 23.27	170.7 ± 13.06	146.2 ± 12.14	116.3 ± 10.81	126 ± 11.31
1.8-2	314.2 ± 17.8	119.2 ± 10.97	81.7 ± 9.764	68.35 ± 9.093	93.98 ± 10.15
2-2.5	388.1 ± 21.21	148.4 ± 12.48	135.7 ± 12.01	89.74 ± 10.02	109 ± 12.33
2.5-3	109.1 ± 12.92	36.33 ± 6.809	34.3 ± 8.488	30.64 ± 7.487	24.22 ± 5.422
3-4	82.18 ± 12.30	— — —	— — —	— — —	— — —

Table 3.7: p raw signal table in minimum-bias, centrality selected d+Au collisions and minimum-bias p+p collisions.

p_T (GeV/c)	d+Au Trigger	0%-20%	20%-40%	40%-100%	p+p
0.4-0.5	692.6 ± 26.33	215.1 ± 14.67	183 ± 13.53	202.8 ± 14.26	421.7 ± 20.56
0.5-0.6	1009 ± 31.76	310.8 ± 17.63	304 ± 17.43	268.5 ± 16.39	526.6 ± 22.95
0.6-0.7	1098 ± 33.17	317.9 ± 17.84	305.6 ± 17.51	327 ± 18.11	561.5 ± 23.71
0.7-0.8	1062 ± 32.59	340.2 ± 18.44	307 ± 17.53	285.5 ± 16.9	435.1 ± 20.86
0.8-0.9	992.2 ± 31.5	315.1 ± 17.81	284.4 ± 16.96	244.4 ± 15.63	376.4 ± 19.4
0.9-1	827.5 ± 28.76	288.9 ± 17	225 ± 15.01	202.6 ± 14.24	310.4 ± 17.62
1-1.1	724 ± 26.91	240.2 ± 15.5	181.5 ± 13.48	192.2 ± 13.87	246.4 ± 15.7
1.1-1.2	608.5 ± 24.67	161.3 ± 12.7	184.3 ± 13.61	149.8 ± 12.25	192 ± 13.87
1.2-1.4	914.9 ± 30.24	301.5 ± 17.36	269.7 ± 16.42	214.1 ± 14.63	269.6 ± 16.42
1.4-1.6	575.8 ± 24	204.9 ± 14.32	160.9 ± 12.71	120.5 ± 10.98	138.6 ± 12.01
1.6-1.8	407.2 ± 20.18	127.3 ± 11.29	108.1 ± 10.43	89.9 ± 9.497	100.6 ± 10.63
1.8-2	257.3 ± 16.26	73.85 ± 8.992	92.22 ± 9.69	46.81 ± 7.802	71.23 ± 8.92
2-2.5	305.6 ± 18.45	114 ± 11.01	83.43 ± 9.464	77.84 ± 9.16	64.02 ± 10.44
2.5-3	111 ± 12.79	28.91 ± 6.26	29.29 ± 8.869	20.55 ± 7.198	25.71 ± 6.856
3-4	67.05 ± 11.87	— — —	— — —	— — —	— — —

Table 3.8: \bar{p} raw signal table in minimum-bias, centrality selected d+Au collisions and minimum-bias p+p collisions.

Chapter 4

Results

4.1 π, K, p and \bar{p} spectra in d+Au and p+p collisions at mid-rapidity

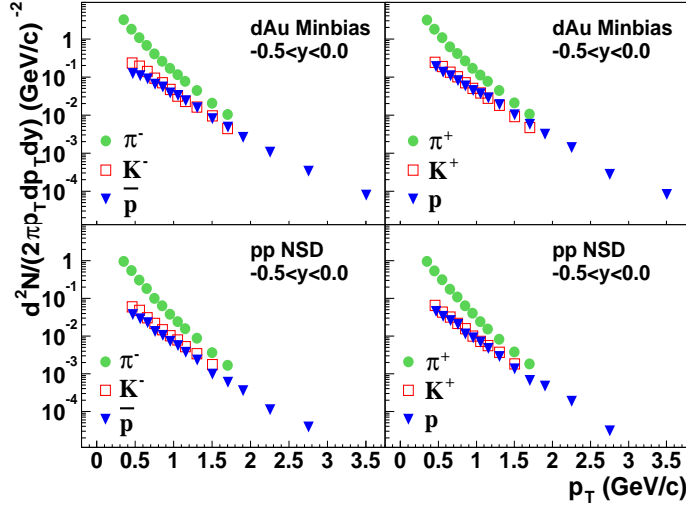


Figure 4.1: The invariant yields of pions (filled circles), kaons (open squares), protons (filled triangles) and their anti-particles as a function of p_T from d+Au and NSD p+p events at 200 GeV. The rapidity range was $-0.5 < y < 0.0$ with the direction of the outgoing Au ions as negative rapidity. Errors are statistical.

The invariant yields $\frac{1}{2\pi p_T} \frac{d^2 N}{dy dp_T}$ of π^\pm , K^\pm , p and \bar{p} from both NSD p+p and minimum-bias d+Au events at mid-rapidity $-0.5 < y < 0$ are shown in Figure 4.1, where N is the corrected signal number per minimum-bias event in each p_T bin. $N = \frac{N_{raw} \times factor3 \times factor4 \times factor5}{N_{total} \times factor1 \times factor2}$, where N_{raw} is the raw signal number in each p_T bin, N_{total} is the total TOFr triggered events, $factor1$ is the enhancement factor of TOFr trigger, $factor2$ is the TPC efficiency times TOFr matching efficiency, $factor3$ is the background correction factor, $factor4$ is the $\langle N_{ch} \rangle$ bias factor, and $factor5$ is the vertex efficiency times trigger efficiency and normalization factor.

4.1.1 Systematic uncertainty

For the invariant yield of π^\pm , K^\pm , p and \bar{p} , the average bin-to-bin systematic uncertainty was estimated to be of the order of 8%. The systematic uncertainty is dominated by the uncertainty in the detector response in Monte Carlo simulations ($\pm 7\%$). Additional factors contributing to the total systematic uncertainty include the background correction ($\pm 3\%$), the small η acceptance of the TOFr ($\pm 2\%$), TOFr response ($\pm 2\%$), the correction for energy loss in the detector ($\lesssim 10 \pm 10\%$ at $p_T < 0.6$ GeV/c for the p and \bar{p} , much smaller for other species and negligible at higher p_T), absorption of \bar{p} in the material ($\pm 3\%$), and the momentum resolution correction ($\simeq 5 \pm 2\%$). The normalization uncertainties in d+Au minimum-bias and p+p NSD collisions are 10% and 14%, respectively [8, 36]. The charged pion yields are consistent with π^0 yields measured by the PHENIX collaboration in the overlapping p_T range [17, 37]. The invariant yields of π^\pm , K^\pm , p and \bar{p} in minimum-bias, centrality selected d+Au and minimum-bias p+p collisions, are listed in the tables in Appendix A with statistical errors and systematic uncertainties.

4.2 Cronin effect

Nuclear effects on hadron production in d+Au collisions are measured through comparison to the p+p spectrum, scaled by the number of underlying nucleon-nucleon

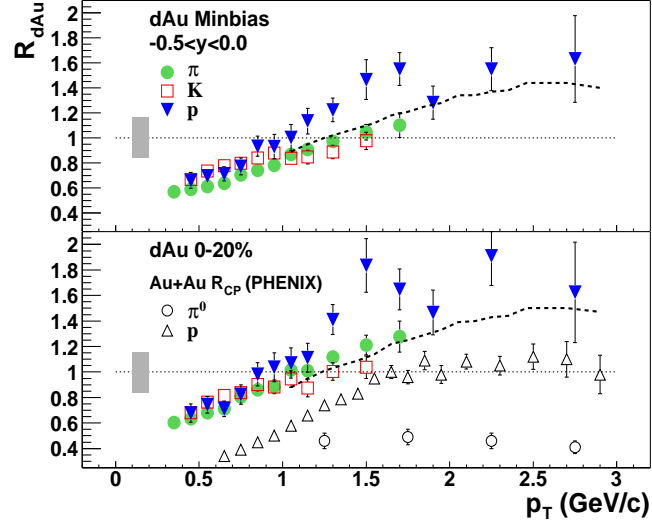


Figure 4.2: The identified particle R_{dAu} for minimum-bias and top 20% d+Au collisions. The filled triangles are for $p + \bar{p}$, the filled circles are for $\pi^+ + \pi^-$ and the open squares are for $K^+ + K^-$. Dashed lines are R_{dAu} of inclusive charged hadrons from [36]. The open triangles and open circles are R_{CP} of $p + \bar{p}$ and π^0 in Au+Au collisions measured by PHENIX [18]. Errors are statistical. The gray band represents the normalization uncertainty of 16%.

inelastic collisions using the ratio

$$R_{dAu} = \frac{d^2 N / (2\pi p_T dp_T dy)}{T_{dAu} d^2 \sigma_{inel}^{pp} / (2\pi p_T dp_T dy)},$$

where $T_{dAu} = \langle N_{bin} \rangle / \sigma_{inel}^{pp}$ describes the nuclear geometry, and $d^2 \sigma_{inel}^{pp} / (2\pi p_T dp_T dy)$ for p+p inelastic collisions is derived from the measured p+p NSD cross section. The difference between NSD and inelastic differential cross sections at mid-rapidity, as estimated from PYTHIA [76], is 5% at low p_T and negligible at $p_T > 1.0$ GeV/c. Figure. 4.2 shows R_{dAu} of $\pi^+ + \pi^-$, $K^+ + K^-$ and $p + \bar{p}$ for minimum-bias and central d+Au collisions. The systematic uncertainties on R_{dAu} are of the order of 16%, dominated by the uncertainty in normalization. The R_{dAu} of the same particle species are similar between minimum-bias and top 20% d+Au collisions. In both cases, the R_{dAu} of protons rise faster than R_{dAu} of pions and kaons. We observe that the spectra of π^\pm , K^\pm , p and \bar{p} are considerably harder in d+Au than those in

p+p collisions. The R_{dAu} of the identified particles has characteristics of the Cronin effect [28, 30] in particle production with R_{dAu} less than unity at low p_T and above unity at $p_T \gtrsim 1.0$ GeV/c.

4.3 $p + \bar{p}/h$ ratio in d+Au and p+p collisions at middle pseudo-rapidity

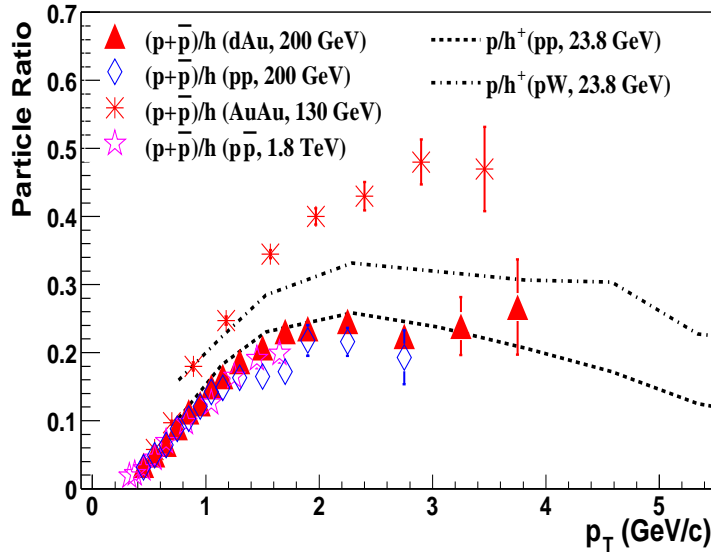


Figure 4.3: Minimum-bias ratios of $(p + \bar{p})$ over charged hadrons at $-0.5 < \eta < 0.0$ from $\sqrt{s_{NN}} = 200$ GeV p+p (open diamonds), d+Au (filled triangles) and $\sqrt{s_{NN}} = 130$ GeV Au+Au [18] (asterisks) collisions. Results of $p + \bar{p}$ collisions at $\sqrt{s_{NN}} = 1.8$ TeV [80] are shown as open stars. Dashed lines are results of p/h^+ ratios from $\sqrt{s_{NN}} = 23.8$ GeV p+p (short-dashed lines) and p+W (dot-dashed) collisions [28]. Errors are statistical.

Figure 4.3 depicts $(p + \bar{p})/h$, the ratio of $p + \bar{p}$ over inclusive charged hadrons as a function of p_T in d+Au and p+p minimum-bias collisions at $\sqrt{s_{NN}} = 200$ GeV, and p/h^+ ratios in p+p and p+W minimum-bias collisions at $\sqrt{s_{NN}} = 23.8$ GeV [28]. Although the relative yields of particles and anti-particles are very different at $\sqrt{s} < 40$ GeV due to the valence quark effects from target and projectile, the Cronin effects are similar. The systematic uncertainties on these ratios were estimated to be of the

order of 10% for $p_T \lesssim 1.0$ GeV/c, decreasing to 3% at higher p_T . At RHIC energies, the anti-particle to particle ratios approach unity ($\bar{p}/p = 0.81 \pm 0.02 \pm 0.04$ in d+Au minimum-bias collisions) and their nuclear modification factors are similar. The difference between R_{dAu} at $\sqrt{s_{NN}} = 200$ GeV for $p + \bar{p}$ and h can be obtained from the $(p + \bar{p})/h$ ratios in d+Au and p+p collisions. Table 4.1 shows $R_{dAu}^{p+\bar{p}}/R_{dAu}^h$ determined by averaging over the bins within $1.2 < p_T < 3.0$ GeV/c. At lower energy, the α parameter in the power law dependence on target atomic weight A^α of identified particle production falls with \sqrt{s} [28]. From the ratios of R_{dAu} between $p + \bar{p}$ and h , we may further derive the $\alpha_p - \alpha_\pi$ for $1.2 < p_T < 3.0$ GeV/c to be $0.041 \pm 0.010(\text{stat}) \pm 0.006(\text{syst})$ under the assumptions that $\alpha_K \simeq \alpha_\pi$ and that $(p + \bar{p})/\pi$ and K/π are between 0.1 and 0.4 in p+p collisions. This result is significantly smaller than the value 0.095 ± 0.004 in the same p_T range found at lower energies [28].

Table 4.1: $\langle N_{bin} \rangle$ from a Glauber model calculation, $(p + \bar{p})/h$ averaged over the bins within $1.2 < p_T < 2.0$ GeV/c (left column) and within $2.0 < p_T < 3.0$ GeV/c (right column) and the R_{dAu} ratios between $p + \bar{p}$ and h averaged over $1.2 < p_T < 3.0$ GeV/c for minimum-bias, centrality selected d+Au collisions and minimum-bias p+p collisions. A p+p inelastic cross section of $\sigma_{inel} = 42$ mb was used in the calculation. For R_{dAu} ratios, only statistical errors are shown and the systematic uncertainties are 0.03 for all centrality bins.

centrality	$\langle N_{bin} \rangle$	$(p + \bar{p})/h$		$R_{dAu}^{p+\bar{p}}/R_{dAu}^h$
min. bias	7.5 ± 0.4	0.21 ± 0.01	0.24 ± 0.01	1.19 ± 0.05
0–20%	15.0 ± 1.1	0.21 ± 0.01	0.24 ± 0.02	1.18 ± 0.06
20–40%	10.2 ± 1.0	0.20 ± 0.01	0.24 ± 0.02	1.16 ± 0.06
40–~100%	$4.0^{+0.8}_{-0.3}$	0.20 ± 0.01	0.23 ± 0.02	1.13 ± 0.06
p+p	1.0	0.17 ± 0.01	0.21 ± 0.02	—

Also shown is $(p + \bar{p})/h$ ratio from the Au+Au minimum-bias collisions at $\sqrt{s_{NN}} = 130$ GeV [18]. The $(p + \bar{p})/h$ ratio from minimum-bias Au+Au collisions [18] at a similar energy is about a factor of 2 higher than that in d+Au and p+p collisions for $p_T \gtrsim 2.0$ GeV/c. This enhancement is most likely due to final-state effects in Au+Au collisions [9, 24, 19, 20, 22, 23]. The ratios show little centrality dependence in d+Au collisions, as shown in Table 4.1 and Figure 4.4. For $p_T < 2.0$ GeV/c, the ratio in

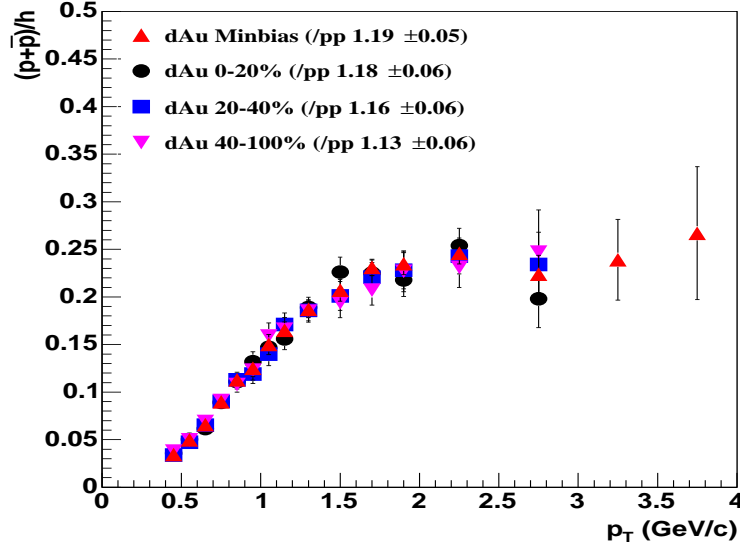


Figure 4.4: Minimum-bias ratios of $(p + \bar{p})$ over charged hadrons at $-0.5 < \eta < 0.0$ from $\sqrt{s_{NN}} = 200$ GeV minimum-bias and centrality selected d+Au collisions. Errors are statistical.

$p + \bar{p}$ collisions at $\sqrt{s_{NN}} = 1.8$ TeV [80] is very similar to those in d+Au and p+p collisions at $\sqrt{s_{NN}} = 200$ GeV.

4.4 K/π , p/π and anti-particle to particle ratios

Centrality Bin	π^-/π^+	X^2/ndf	K^-/K^+	X^2/ndf	\bar{p}/p	X^2/ndf
d+Au M.B.	1.01 ± 0.01	0.88	0.94 ± 0.02	1.78	0.81 ± 0.02	0.85
0%-20%	1.01 ± 0.01	0.80	0.93 ± 0.03	1.43	0.80 ± 0.03	0.70
20%-40%	1.00 ± 0.01	0.98	0.91 ± 0.03	1.19	0.79 ± 0.03	1.14
40%-100%	1.02 ± 0.01	0.81	1.02 ± 0.03	0.45	0.78 ± 0.03	0.70
p+p	1.00 ± 0.01	1.24	0.98 ± 0.02	0.71	0.79 ± 0.03	0.73

Table 4.2: π^-/π^+ , K^-/K^+ and \bar{p}/p ratios in p+p and d+Au minimum-bias collisions. Also shows in the table are the ratios in centrality selected d+Au collisions. Errors are statistical.

Figure 4.5 shows the π^-/π^+ , K^-/K^+ and \bar{p}/p ratios as a function of p_T in d+Au and p+p minimum-bias collisions. It shows the anti-particle to particle ratios are flat with p_T . The zero order polynomial function was used to fit the data and get the anti-particle to particle ratios. The results are list in Table 4.2. In centrality selected

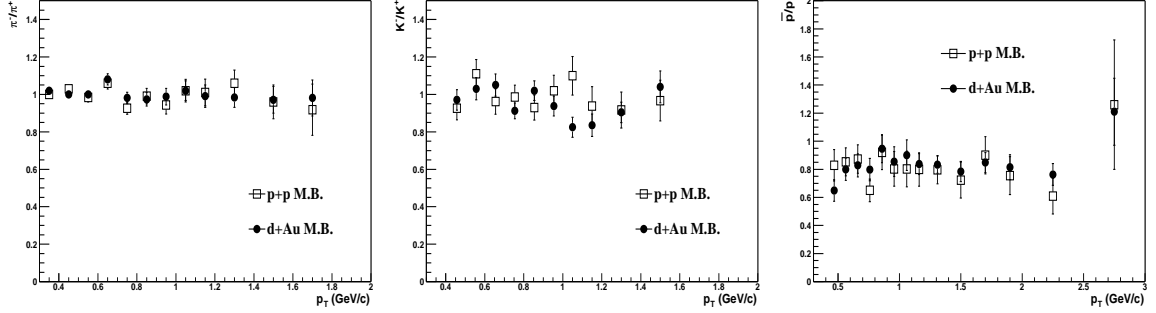


Figure 4.5: π^-/π^+ , K^-/K^+ and \bar{p}/p ratios as a function of p_T in d+Au and p+p minimum-bias collisions. The open symbols are for p+p collisions and the solid symbols for d+Au collisions. Errors are statistical.

d+Au collisions, the anti-particle to particle ratios are also flat with p_T and show little centrality dependence. The results are also shown in the Table 4.2.

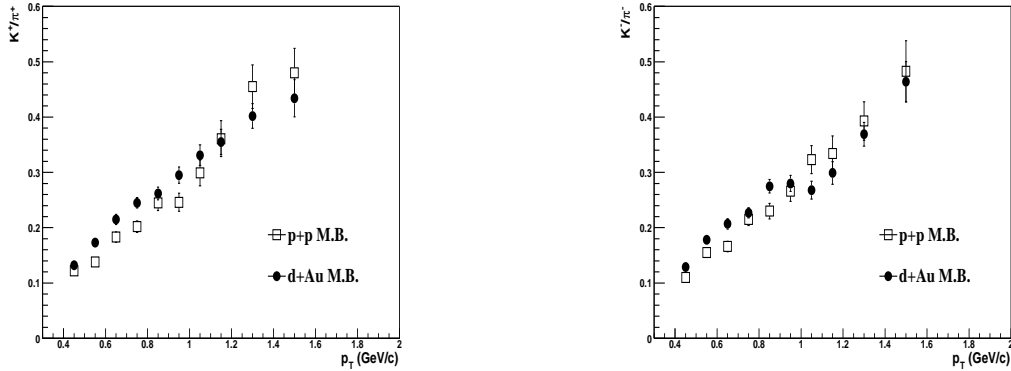


Figure 4.6: K/π ratios as a function of p_T in d+Au and p+p minimum-bias collisions. The open symbols are for p+p collisions and the solid symbols for d+Au collisions. Errors are statistical.

The K/π and p/π ratios are shown in Figure 4.6 and Figure 4.7 individually. From the plots, the K/π ratios increase with p_T in both d+Au and p+p collisions and the increasing trend is the same within our errors. The p/π ratios increase with p_T in both d+Au and p+p collisions and the increasing in d+Au collisions is faster than that in p+p collisions. The trends of the K/π and p/π as a function of p_T show little centrality dependence in d+Au collisions.

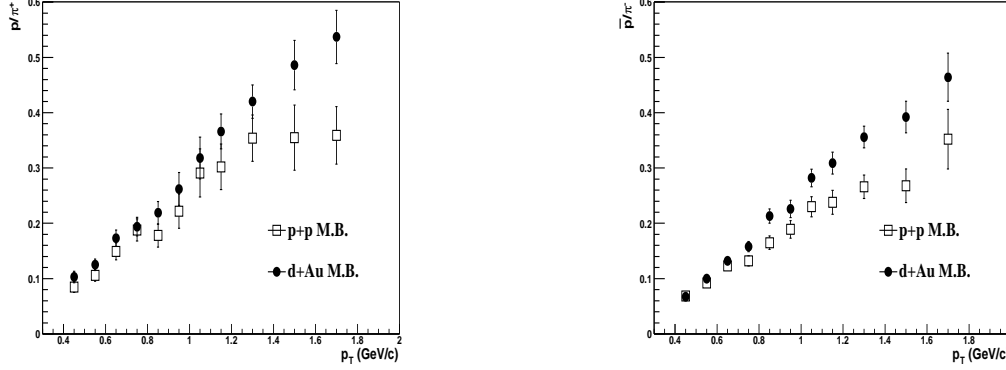


Figure 4.7: $p(\bar{p})/\pi$ ratios as a function of p_T in d+Au and p+p minimum-bias collisions. The open symbols are for p+p collisions and the solid symbols for d+Au collisions. Errors are statistical.

4.5 dN/dy , $\langle p_T \rangle$, and model fits

The spectra in minimum-bias and centrality selected d+Au collisions and also in p+p collisions are shown in Figure 4.8, Figure 4.9 and Figure 4.10. The spectra show little centrality dependence for each particle in d+Au collisions but harder than those in p+p collisions. The power law function was used to fit the spectra and get the dN/dy and $\langle p_T \rangle$. The power law fit function is:

$$\frac{1}{2\pi p_T} \frac{d^2N}{dy dp_T} = a \left(1 + \frac{p_T}{\langle p_T \rangle \frac{n-3}{2}} \right)^{-n} \quad (4.1)$$

Where the parameter a is a constant value proportional to the mid-rapidity yield dN/dy , the parameter n is the order of the power law and $\langle p_T \rangle$ is the mean value of the transverse momentum which is extracted from the fit. Figure 4.11 shows power law fit to the spectra of minimum-bias d+Au and p+p collisions. Figure 4.12 shows power law fit to the spectra of 3 centrality selected d+Au collisions. The power law fit results are listed in Table 4.4 and Table 4.3 individually. The thermal model [34] was also used to fit the spectra. The final dN/dy and $\langle p_T \rangle$ are shown in Table 4.6 and Table 4.5 respectively, which were obtained by averaging the results from the power law fit and thermal fit. Half of the differences in them are taken as the systematic errors due to the extrapolation to low p_T region. The errors in this table include the

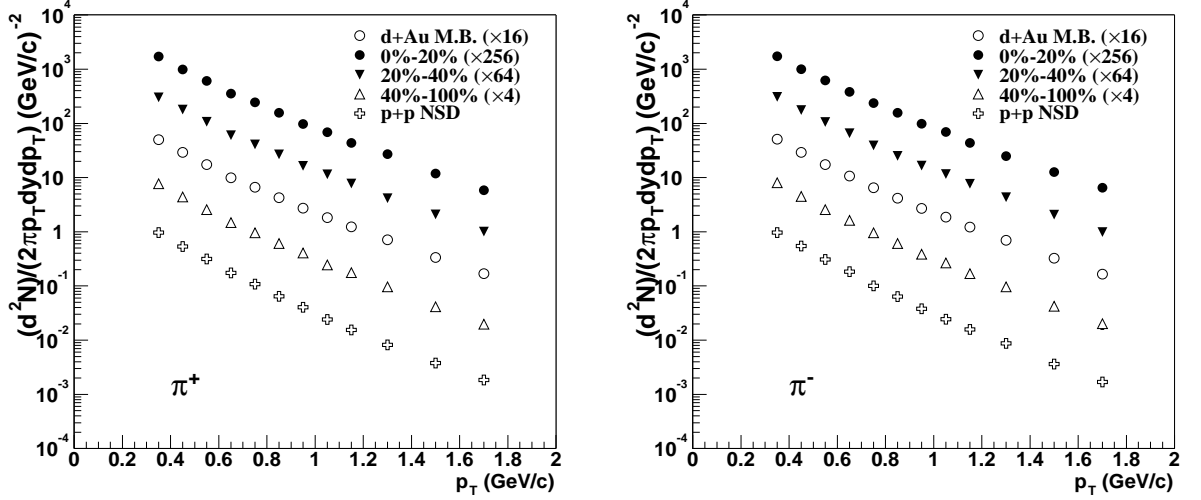


Figure 4.8: The re-scaled π^+ and π^- spectra in minimum-bias, centrality selected d+Au collisions and also in p+p collisions. The errors are statistical.

systematic uncertainties and statistical errors.

Centrality Bin	π^-	π^+	K^-	K^+	\bar{p}	p
d+Au M.B.	0.403 ± 0.004	0.405 ± 0.004	0.609 ± 0.009	0.629 ± 0.009	0.714 ± 0.008	0.677 ± 0.010
0%-20%	0.421 ± 0.004	0.421 ± 0.004	0.626 ± 0.018	0.658 ± 0.016	0.727 ± 0.013	0.705 ± 0.014
20%-40%	0.408 ± 0.004	0.411 ± 0.004	0.604 ± 0.015	0.625 ± 0.015	0.725 ± 0.013	0.691 ± 0.015
40%-100%	0.387 ± 0.005	0.391 ± 0.004	0.589 ± 0.016	0.616 ± 0.016	0.667 ± 0.013	0.646 ± 0.014
p+p	0.357 ± 0.004	0.361 ± 0.004	0.571 ± 0.013	0.571 ± 0.013	0.567 ± 0.010	0.569 ± 0.012

Table 4.3: $\langle p_T \rangle$ of π^- , π^+ , K^- , K^+ , \bar{p} and p from power law fit in minimum-bias, centrality selected d+Au collisions and also in p+p collisions. The errors are from the power law fit. The unit of p_T is GeV/c.

4.6 System comparison

Figure 4.13 shows the $\langle p_T \rangle$ of π^- , K^- and \bar{p} as a function of charged particle multiplicity at mid-rapidity. From p+p to d+Au collisions, the $\langle p_T \rangle$ increase with charged particle multiplicity smoothly. We observed the $\langle p_T \rangle$ in 0%-20% d+Au collisions are larger than those in peripheral Au+Au collisions. The K^-/π^- and \bar{p}/π^- as a function of charged particle multiplicity at mid-rapidity are shown in Figure 4.14. The K^-/π^- and \bar{p}/π^- ratios were derived by taking the ratios of the dN/dy of K^- or \bar{p} over the

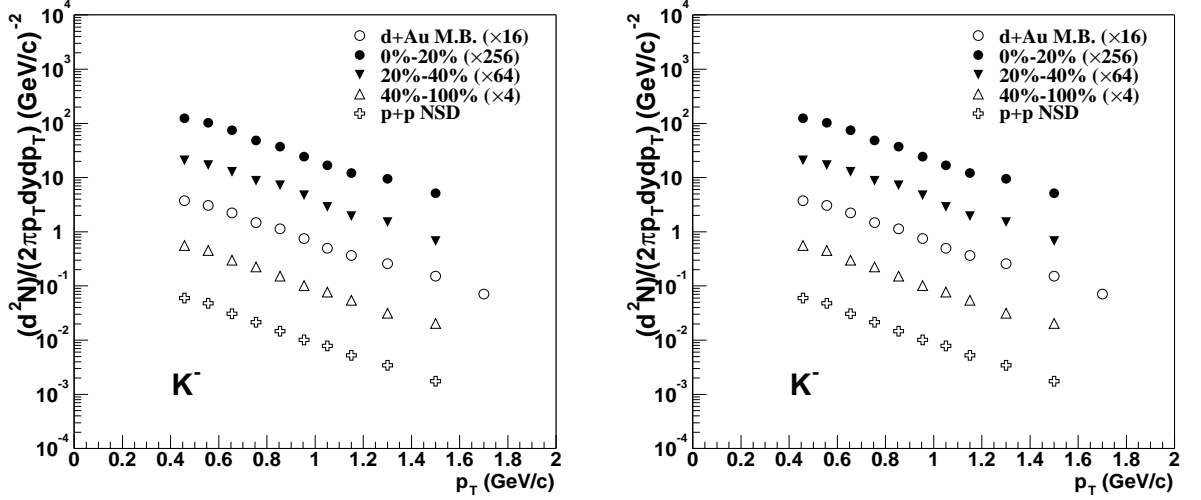


Figure 4.9: The re-scaled K^+ and K^- spectra in minimum-bias, centrality selected d+Au collisions and also in p+p collisions. The errors are statistical.

Centrality Bin	π^-	π^+	K^-	K^+	\bar{p}	p
d+Au M.B.	5.078 ± 0.080	5.032 ± 0.080	0.685 ± 0.013	0.703 ± 0.012	0.466 ± 0.009	0.594 ± 0.019
0%-20%	10.657 ± 0.190	10.521 ± 0.187	1.448 ± 0.085	1.453 ± 0.035	0.972 ± 0.026	1.222 ± 0.045
20%-40%	7.631 ± 0.148	7.515 ± 0.139	0.988 ± 0.028	1.051 ± 0.027	0.651 ± 0.018	0.842 ± 0.033
40%-100%	3.153 ± 0.069	3.024 ± 0.060	0.399 ± 0.012	0.379 ± 0.011	0.261 ± 0.008	0.338 ± 0.014
p+p	1.524 ± 0.027	1.504 ± 0.027	0.166 ± 0.004	0.173 ± 0.009	0.113 ± 0.003	0.137 ± 0.007

Table 4.4: dN/dy of π^- , π^+ , K^- , K^+ , \bar{p} and p from power law fit in minimum-bias, centrality selected d+Au collisions and also in p+p collisions. The errors are from the power law fit.

dN/dy of π^- in table 4.6. These ratios increase with charged particle multiplicity from p+p, d+Au to Au+Au collisions smoothly. The kinetic freeze out temperature T_{kin} and flow velocity $\langle\beta\rangle$ from thermal fit as a function of charged particle multiplicity are shown in Figure 4.15. We can see the T_{kin} is flat from p+p to d+Au and then decreases from d+Au to Au+Au collisions and the $\langle\beta\rangle$ increases from p+p, d+Au to Au+Au collisions.

Centrality Bin	π^-	π^+	K^-	K^+	\bar{p}	p
d+Au M.B.	0.420 ± 0.019	0.422 ± 0.019	0.613 ± 0.025	0.625 ± 0.025	0.761 ± 0.056	0.739 ± 0.069
0%-20%	0.435 ± 0.017	0.436 ± 0.017	0.627 ± 0.025	0.646 ± 0.028	0.774 ± 0.056	0.761 ± 0.063
20%-40%	0.425 ± 0.019	0.427 ± 0.018	0.610 ± 0.025	0.622 ± 0.025	0.766 ± 0.052	0.744 ± 0.061
40%-100%	0.405 ± 0.020	0.408 ± 0.019	0.591 ± 0.024	0.608 ± 0.026	0.715 ± 0.056	0.703 ± 0.063
p+p	0.377 ± 0.021	0.379 ± 0.020	0.565 ± 0.023	0.565 ± 0.023	0.627 ± 0.065	0.634 ± 0.070

Table 4.5: The final $\langle p_T \rangle$ of π^- , π^+ , K^- , K^+ , \bar{p} and p in minimum-bias, centrality selected d+Au collisions and also in p+p collisions. The unit of p_T is GeV/c.

Centrality Bin	π^-	π^+	K^-	K^+	\bar{p}	p
d+Au M.B.	4.731 ± 0.359	4.668 ± 0.356	0.662 ± 0.040	0.684 ± 0.039	0.425 ± 0.044	0.531 ± 0.067
0%-20%	10.063 ± 0.628	9.932 ± 0.621	1.383 ± 0.095	1.418 ± 0.079	0.896 ± 0.084	1.114 ± 0.117
20%-40%	7.137 ± 0.514	7.074 ± 0.464	0.952 ± 0.059	1.020 ± 0.059	0.603 ± 0.054	0.765 ± 0.083
40%-100%	2.925 ± 0.236	2.829 ± 0.203	0.387 ± 0.023	0.371 ± 0.020	0.238 ± 0.025	0.304 ± 0.036
p+p	1.411 ± 0.116	1.400 ± 0.108	0.163 ± 0.009	0.168 ± 0.010	0.099 ± 0.015	0.120 ± 0.018

Table 4.6: The final dN/dy of π^- , π^+ , K^- , K^+ , \bar{p} and p in minimum-bias, centrality selected d+Au collisions and also in p+p collisions.

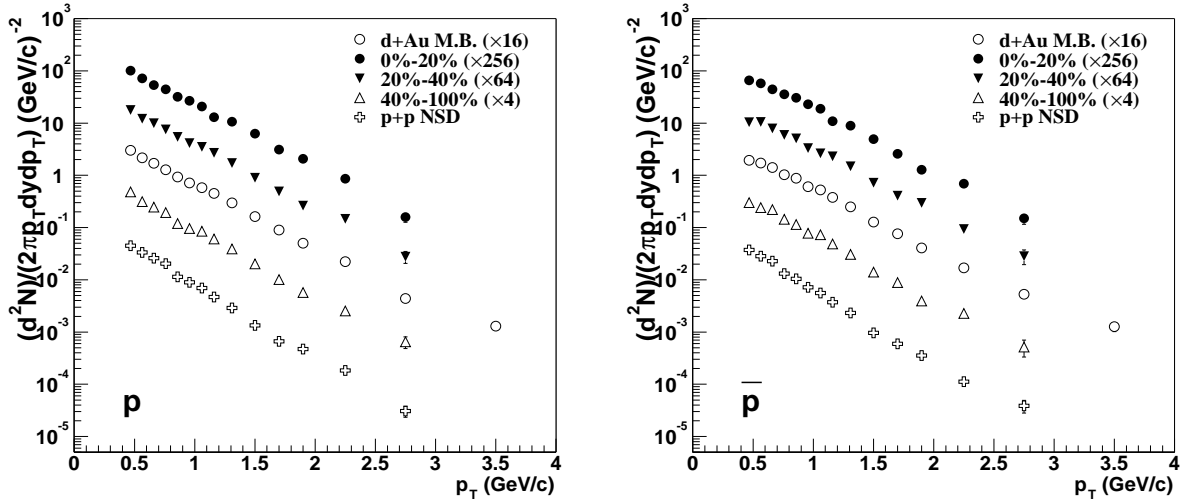


Figure 4.10: The re-scaled p and \bar{p} spectra in minimum-bias, centrality selected d+Au collisions and also in p+p collisions. The errors are statistical.

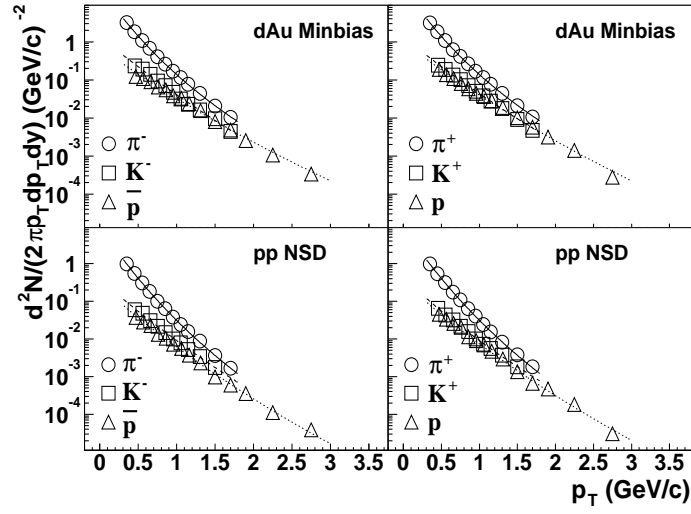


Figure 4.11: The spectra of π^- , π^+ , K^- , K^+ , \bar{p} and p in d+Au and p+p minimum-bias collisions. The curves are from power law fit.

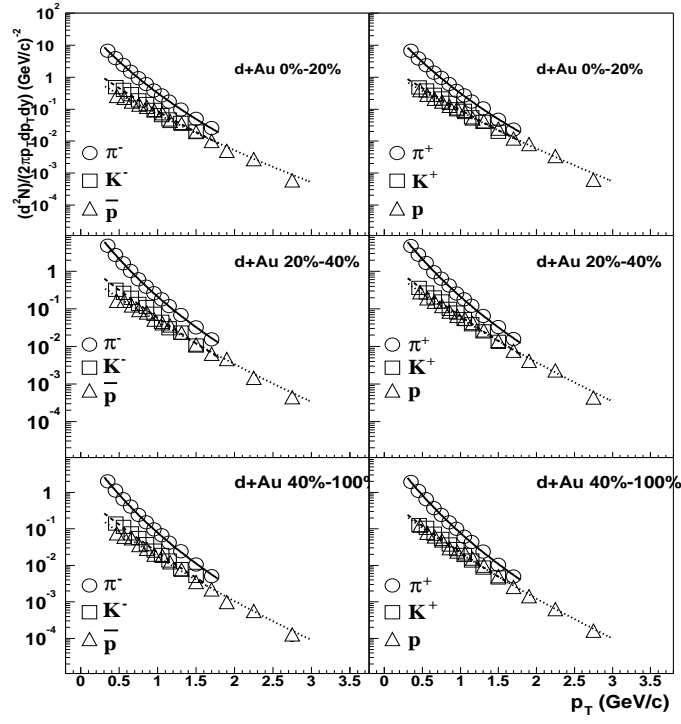


Figure 4.12: The spectra of π^- , π^+ , K^- , K^+ , \bar{p} and p in three centrality selected d+Au collisions. The curves are from power law fit.

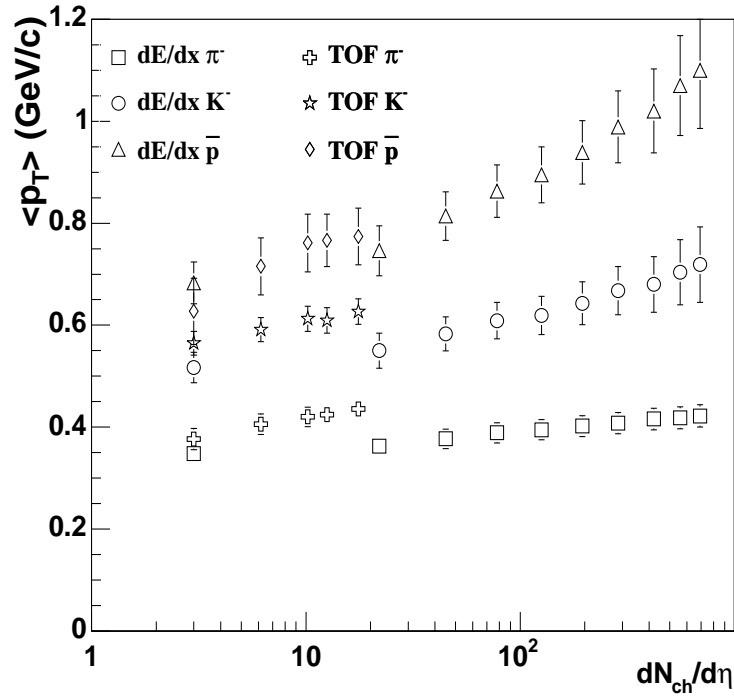


Figure 4.13: $\langle p_T \rangle$ as a function of $dN/d\eta$. The squared, circled and triangled symbols are from [35] in p+p and Au+Au collisions. The cross, star and diamond are our data points in p+p and d+Au collisions. Statistic errors and systematic uncertainties have been added in quadrature.

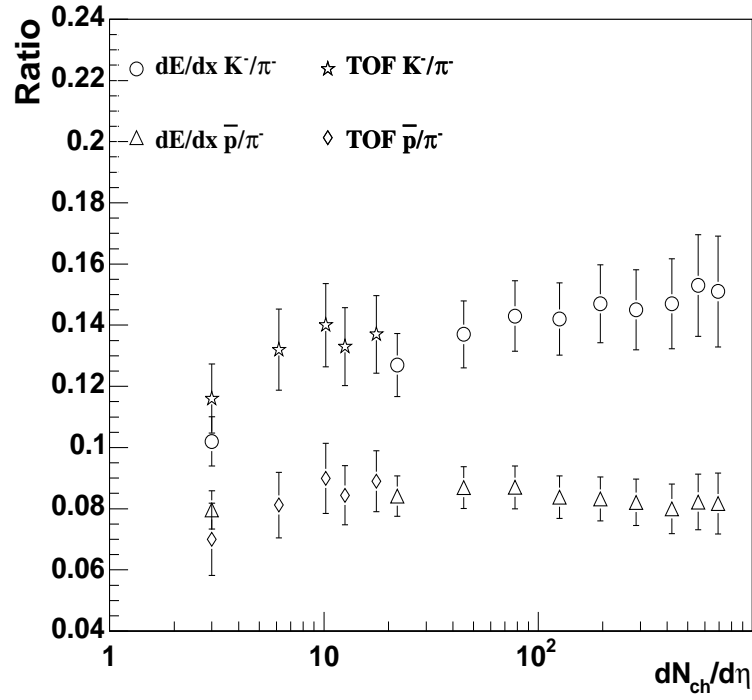


Figure 4.14: K^-/π^- and \bar{p}/π^- as a function of $dN/d\eta$. The circled and triangled symbols are from [35] in p+p and Au+Au collisions. The star and diamond are our data points in p+p and d+Au collisions. Statistic errors and systematic uncertainties have been added in quadrature.

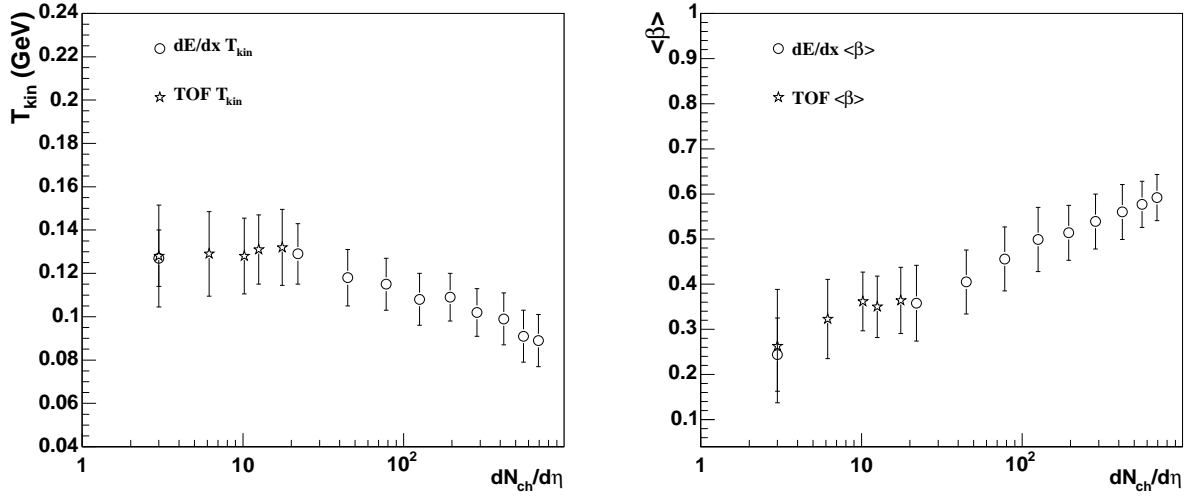


Figure 4.15: The kinetic freeze out temperature T_{kin} (left) and flow velocity $\langle\beta\rangle$ (right) from thermal fit as a function of charged particle multiplicity. The circled symbols are from [35] in p+p and Au+Au collisions. The star are our data points in p+p and d+Au collisions. Errors are systematic.

Chapter 5

Discussion

5.1 Cronin effect

The identified particle spectra in d+Au and p+p collisions not only provide the reference for those in Au+Au collisions at 200 GeV, but also provide a chance to see the mechanism of the Cronin effect itself clearly. Cronin effect was observed 30 years ago [28]. It is the enhancement of particle production at high p_T . The enhancement was explained by initial multiple parton scattering. Also the recent experimental results of Cronin effect on inclusive charged hadron are consistent with the predictions based on initial multiple parton scattering [30]. It suggests the suppression at intermediate p_T in Au+Au collisions is due to final state effects. However, the initial multiple parton scattering with the independent fragmentation function will result in the same Cronin effect for $p(\bar{p})$ and for pions, while experimentally the Cronin effect for $p(\bar{p})$ is larger than that for π . That's to say the initial multiple scattering with the independent fragmentation function can't account for the Cronin effect observed. Maybe in the initial multiple parton scattering, the broadening for gluon and for quark/antiquark are not the same [88]. Or maybe the fragmentation processes in p+A collisions are not the same as those in p+p collisions [89]. Whether the Cronin effect is initial state effect or final state effect will be discussed below.

5.1.1 Model comparison: initial state effect?

The initial multiple parton scattering model predicts that the Cronin effect on deuteron beam outgoing side is larger than that on Au beam outgoing side since the deuteron traverses a much larger nucleus [87]. Figure 5.1 (left) shows the predictions for the Cronin effect at different rapidity range. The different curves correspond to the prediction results from different shadowings. The $y = 1$ is on the deuteron beam outgoing side. The $y = -1$ is on the Au beam outgoing side. The $y = 0$ is at mid-rapidity. We can see that the R_{dAu} on deuteron beam side ($y = 1$) increases faster than that on Au beam side ($y = -1$). If we take the ratio of R_{dAu} on Au beam side over R_{dAu} on deuteron beam side, it will result in a minimum value at $p_T \sim 3.5$ GeV/c, as shown in the curves on the right plot of Figure 5.1. The solid symbol on the right plot of Figure 5.1 represents the data points [90], which is the ratio of R_{dAu} on Au beam side at $-1 < \eta < -0.5$ over R_{dAu} on deuteron beam side at $0.5 < \eta < 1$. We observe the η asymmetry from experiment reaches a maximum value firstly and then decreases. This is different from the predictions. That means, the model based on initial multiple parton scattering only, can't reproduce the experimental results. Recently, Qiu and Vitev have come up with the idea of coherent multiple scattering and applied it to the RHIC experiments [91]. In this picture, the hard probe may interact coherently with many low x parton inside different nucleons inside the nucleus. As a result, this process will lead to the suppression of the total cross section. This coherent effect will play an important role in p+A collisions at forward rapidity. In the deuteron outgoing beam direction, the coherent effect is non-negligible since the Au nucleus is big while on the Au side, the coherent effect is not big since the deuteron is of a small size. This will result in bigger suppression on the deuteron side than on the Au side. It may qualitatively reproduce the data. This coherent multiple scattering is a final-state effect.

As we all known, in Au+Au collisions, the suppression at intermediate p_T can be reproduced by the initial multiple scattering and jet quenching qualitatively [8, 9]. However, the model based on the initial multiple scattering, jet quenching and independent fragmentation will result in the same suppression for baryons and mesons at intermediate p_T in Au+Au collisions. Experimentally R_{cp} for baryons are larger than

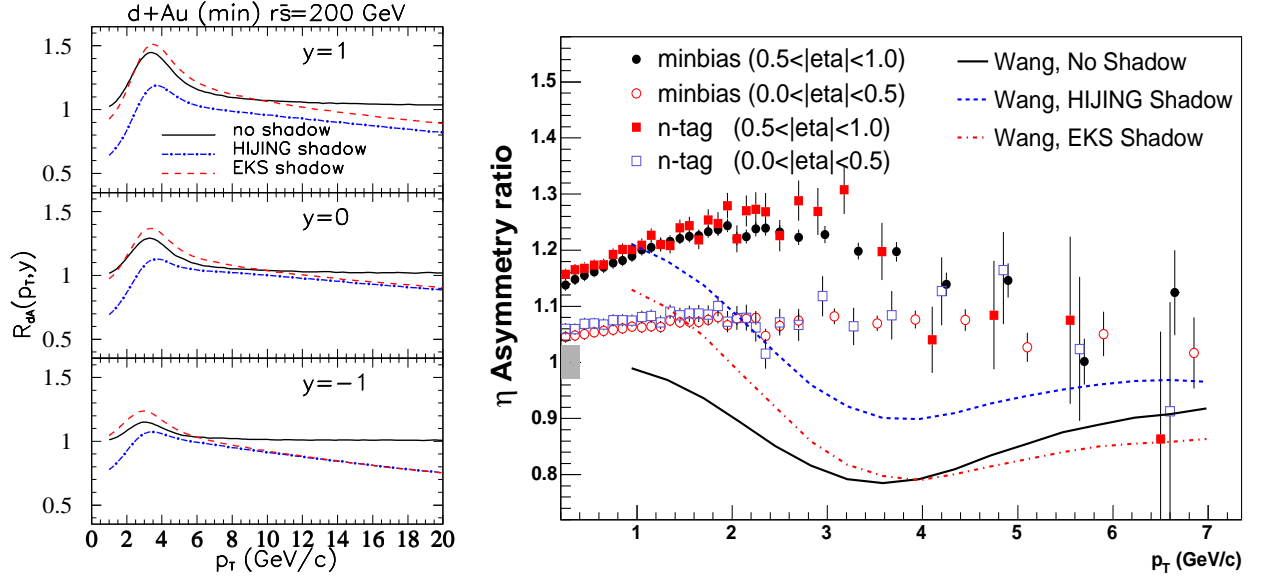


Figure 5.1: (left) The Cronin effect at different rapidity as a function of p_T . The different curve in each panel shows the different shadowing. This figure is from [87]. (right) The η asymmetry of the Cronin effect: the ratio of Cronin effect in Au beam outgoing direction over the Cronin effect in deuteron beam outgoing direction. This figure is from [90].

R_{cp} for mesons at intermediate p_T . This difference can be reproduced by coalescence or recombination models [21, 22, 23]. Recently the recombination model [92] has been applied to d+Au system to see whether it can reproduce the Cronin effect or not.

With the help of Prof. C.B. Yang [93], I also compare our pion and proton spectra in d+Au collisions with the recombination model [92]. In the following the recombination model [92] will be discussed and the comparison between the data and the model will be presented in detail.

5.1.2 Model comparison: recombination

The inclusive distribution for the production of pions can be written in the recombination model [92], when mass effects are negligible, in the invariant form

$$p \frac{dN_{\pi}}{dp} = \int \frac{dp_1}{p_1} \frac{dp_2}{p_2} F_{q\bar{q}}(p_1, p_2) R_{\pi}(p_1, p_2, p), \quad (5.1)$$

where $F_{q\bar{q}}(p_1, p_2)$ is the joint distribution of a q and \bar{q} at p_1 and p_2 , and $R_\pi(p_1, p_2, p)$ is the recombination function for forming a pion at p : $R_\pi(p_1, p_2, p) = (p_1 p_2 / p) \delta(p_1 + p_2 - p)$. $F_{q\bar{q}}$ depends on the colliding hadron/nuclei. In general, $F_{q\bar{q}}$ has four contributing components represented schematically by

$$F_{q\bar{q}} = \mathcal{T}\mathcal{T} + \mathcal{T}\mathcal{S} + (\mathcal{S}\mathcal{S})_1 + (\mathcal{S}\mathcal{S})_2 \quad (5.2)$$

where \mathcal{T} denotes thermal distribution and \mathcal{S} shower distribution. $(\mathcal{S}\mathcal{S})_1$ signifies two shower partons in the same hard-parton jet, while $(\mathcal{S}\mathcal{S})_2$ stands for two shower partons from two nearby jets [92].

For $p+A$ collisions it may not be appropriate to refer to any partons as thermal in the sense of a hot plasma as in heavy-ion collisions. Here in d+Au collisions, the symbol \mathcal{T} represents the soft parton distribution at low k_T . At low p_T the observed pion distribution is exponential; we identify it with the contribution of the $\mathcal{T}\mathcal{T}$ term [92].

$$\frac{dN_\pi^{\mathcal{T}\mathcal{T}}}{pd p} = \frac{C^2}{6} \exp(-p/T) \quad (5.3)$$

where T is the inverse slope. We shall determine C and T by fitting the d+Au data at low p_T . The pion spectra for different centralities can be calculated from thermal-thermal ($pion_{tt}$), thermal-shower ($pion_{ts}$) and shower-shower ($pion_{ss}$) contributions by using parameters C and N_{bin} : $dN/p_T dp_T = C \times C \times pion_{tt} + 2.5 \times C \times N_{bin} \times pion_{ts} + 2.5 \times N_{bin} \times pion_{ss}$, where C is determined by fitting the d+Au data at $0.4 < p_T < 1.0$ GeV/c, and N_{bin} is the number of binary collisions. The data points of $pion_{tt}$, $pion_{ts}$ and $pion_{ss}$ are from Prof. C.B. Yang [93]. The C values for minimum-bias, 0-20%, 20-40% and 40-~100% d+Au collisions are 8.85, 13.08, 10.96 and 6.84 individually. The T value of 0.21 GeV is used in the low p_T fit. Figure 5.2 shows the π^+ spectra in d+Au collisions as well as those from recombination model. This figure shows that the recombination model can reproduce the spectra of pion in minimum-bias and centrality selected d+Au collisions.

The invariant inclusive distribution for proton formation at midrapidity in the recombination model [92]

$$p^0 \frac{dN_p}{dp} = \int \frac{dp_1}{p_1} \frac{dp_2}{p_2} F(p_1, p_2, p_3) R_p(p_1, p_2, p_3, p) \quad (5.4)$$

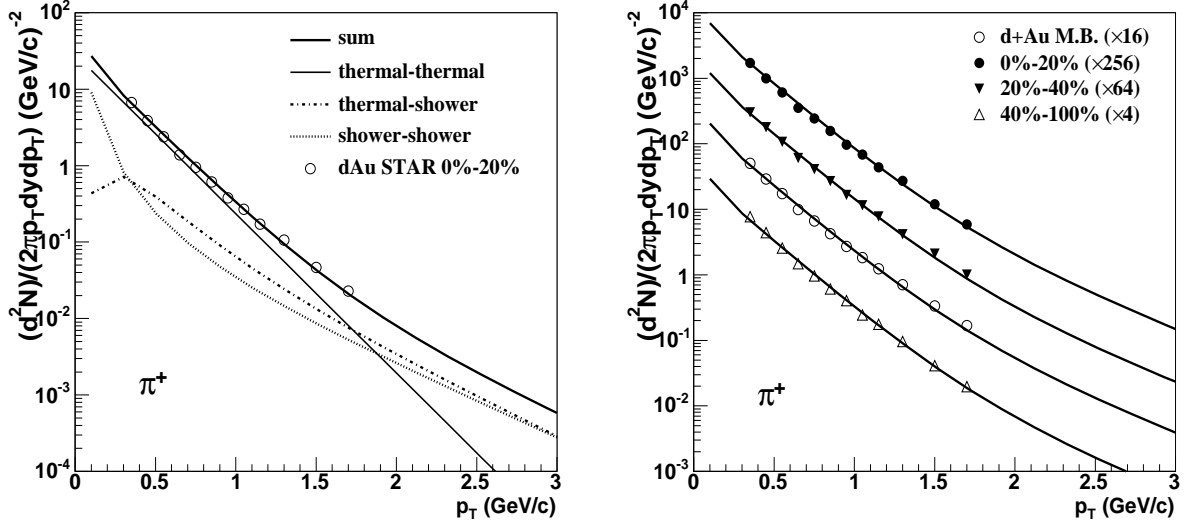


Figure 5.2: (left) The invariant yield for π^+ at 0%-20% d+Au collisions as a function of p_T . The open circles are our data points. The curves are the calculation results from recombination model. Sum represents the total contribution from recombination model. Thermal-thermal represents the soft contribution. The thermal-shower represents the contribution from the interplay between soft and hard components. The shower-shower represents the hard contribution. (right) The invariant yields for π^+ in minimum-bias and centrality selected d+Au collisions as a function of p_T . The symbols represent our data points. The curves on the top of the symbols are the corresponding calculation results from recombination model.

where all momentum variables p_i and p are transverse momenta, and p^0 denotes the energy of the proton. $F(p_1, p_2, p_3)$ is the joint distribution of u, u , and d quarks at p_1, p_2 and p_3 , respectively. $R_p(p_1, p_2, p_3, p)$ is the recombination function for a proton with momentum p . We write schematically

$$F = TTT + TTS + TSS + SSS \quad (5.5)$$

where all the shower partons \mathcal{S} are from one hard parton jet. Shower partons from different jets are ignored here for RHIC energies. In d+Au collisions, \mathcal{T} denotes the soft partons that are not associated with the shower components of a hard parton. The SSS term is regarded as the fragmentation of a hard parton into a proton. The TTT term comes entirely from the soft partons, while TTS and TSS accounts for

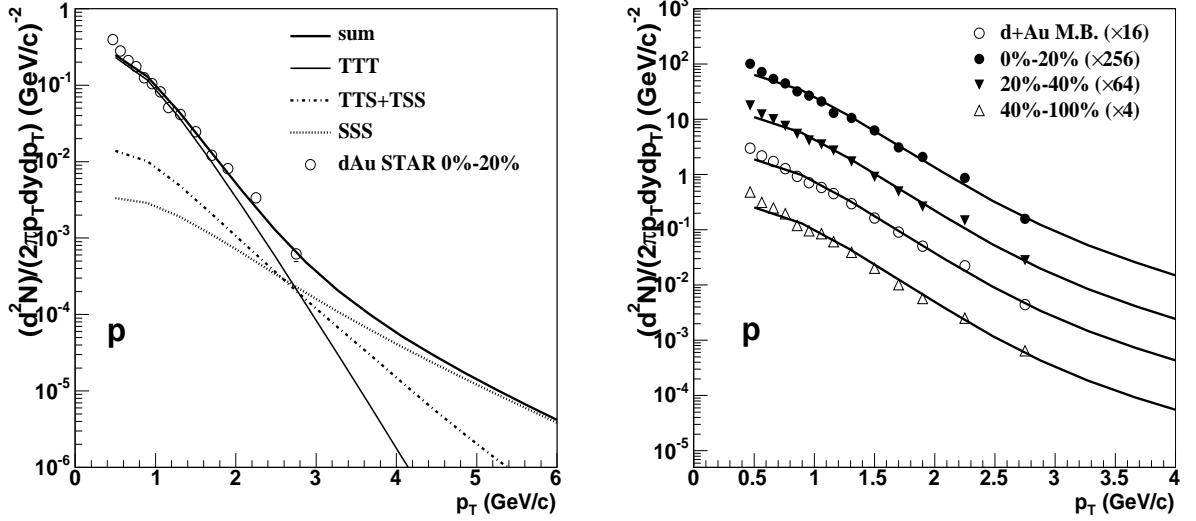


Figure 5.3: (left) The invariant yield for p at 0%-20% d+Au collisions as a function of p_T . The open circles are our data points. The curves are the calculation results from recombination model. Sum represents the total contribution from recombination model. TTT represents the soft contribution. The TTS+TSS represents the contribution from the interplay between soft and hard components. The SSS represents the hard contribution. (right) The invariant yields for p in minimum-bias and centrality selected d+Au collisions as a function of p_T . The symbols represent our data points. The curves on the top of the symbols are the corresponding calculation results from recombination model.

the interplay between the soft and shower partons. The soft contribution to the proton spectrum arising from \mathcal{TTT} recombination is

$$\frac{dN_{proton}^{th}}{p dp} = \frac{C^3}{6} \frac{p^2}{p^0} e^{-p/T} \frac{B(\alpha+2, \gamma+2)B(\alpha+2, \alpha+\gamma+4)}{B(\alpha+1, \gamma+1)B(\alpha+1, \alpha+\gamma+2)} \quad (5.6)$$

. Where C and T are determined by fitting the proton spectra at low p_T , the α is equal to 1.75, γ is equal to 1.05, $B(x, y)$ is the beta function [92]. For the invariant yield of proton, there are 4 different contributions: soft-soft-soft ($proton_{ttt}$), soft-soft-shower ($proton_{tts}$), soft-shower-shower ($proton_{tss}$), and shower-shower-shower ($proton_{sss}$). The total contributions are $dN/p_T dp_T = C \times C \times C \times proton_{ttt} + C \times C \times N_{bin} \times proton_{tts} + C \times N_{bin} \times proton_{tss} + N_{bin} \times proton_{sss}$, where C is determined by fitting the d+Au data at $0.5 < p_T < 1.5$ GeV/c , and N_{bin} is the number of binary collisions. The data

points of $proton_{ttt}$, $proton_{tts}$, $proton_{tss}$ and $proton_{sss}$ are from Prof. C.B. Yang [93]. The C values for minimum-bias, 0-20%, 20-40% and 40-~100% d+Au collisions are 9.67, 12.34, 10.92 and 7.91 individually. The T value of 0.21 GeV is used in the low p_T fit. Figure 5.3 shows the proton spectra in d+Au collisions as well as those from recombination model. This figure shows that the recombination model can reproduce the spectra of proton in minimum-bias and centrality selected d+Au collisions. From the comparison between our data and the calculation results from the recombination model, we know that the recombination model actually can reproduce both the proton and pion spectra in d+Au collisions, while as we have mentioned above, the initial multiple parton scattering model [30] with independent fragmentation can't reproduce the difference of Cronin effect between proton and pion. Besides, the initial multiple parton scattering model with independent fragmentation can't reproduce the η asymmetry of the Cronin effect. In the recombination model [92], the number of such soft partons on the Au outgoing side is larger than that on the deuteron outgoing side. This will result in the Cronin effect on the Au side larger than that on the deuteron side [92]. Qualitatively the recombination model can reproduce the η asymmetry of the Cronin effect. As we know, the recombination model is a final-state effect model. These all seem to indicate that the Cronin effect is not initial-state effect only. The final-state effect plays an important role too. To directly confirm the Cronin effect is initial or final state effect, it's necessary for us to compare the Cronin effect of Drell-Yan process with those of pion, kaon and proton. I will come to this later.

5.1.3 Integral yield R_{dAu} : shadowing effect?

The initial multiple elastic scattering only changes the p_T distribution while the total cross section should not change. Thus we can look at the integral yield dN/dy R_{dAu} , which are measured through comparison to the integral yield dN/dy in p+p collisions, scaled by the number of binary collisions N_{bin} . Figure 5.4 shows that integral yield R_{dAu} of pion, kaon and proton as a function of $dN/d\eta$ in minimum-bias and centrality selected d+Au collisions at mid-rapidity. The integral yield R_{dAu} of pion and kaon are less than 1 while that of proton is close to 1. This may be the indication of

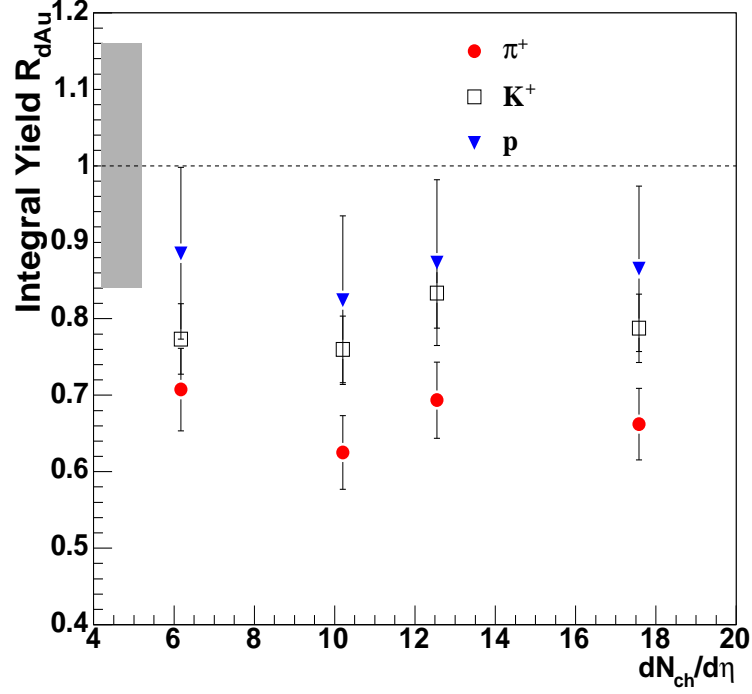


Figure 5.4: Integral yield R_{dAu} as a function of $dN/d\eta$ in minimum-bias and centrality selected d+Au collisions at mid-rapidity. Statistic errors and systematic uncertainties have been added in quadrature. The shadowing represents the normalization uncertainty.

shadowing effect at 200 GeV. The integral yield R_{dAu} for proton is larger than that for kaon and a little bit more larger than that for pion. This may be the indication that the shadowing effect is mass dependent at 200 GeV.

5.1.4 Initial or final state effect: Drell-Yan process

In order to see the Cronin effect is initial or final state effect, we may look into the Drell-Yan process since there is little final state effect in Drell-Yan process. If there is no enhancement at high p_T for Drell-Yan process, the enhancement for π, K, p is due to final-state effect. Figure 5.5 shows the integral yield Cronin ratio as a function of atomic weight at p-A fixed target experiment [95]. The proton incident energy is

800 GeV. We can see there is no enhancement for Drell-Yan process. However, this is the total cross section while what we want to compare is Cronin ratio as a function of p_T . It will be better if we have the p_T dependence of Cronin ratio of Drell-Yan process. However, at the same p_T range with the same proton incident energy, the Cronin ratio of Drell-Yan is not available in p+A collisions. It's hard to compare the Cronin ratio of Drell-Yan process with those of π, K, p .

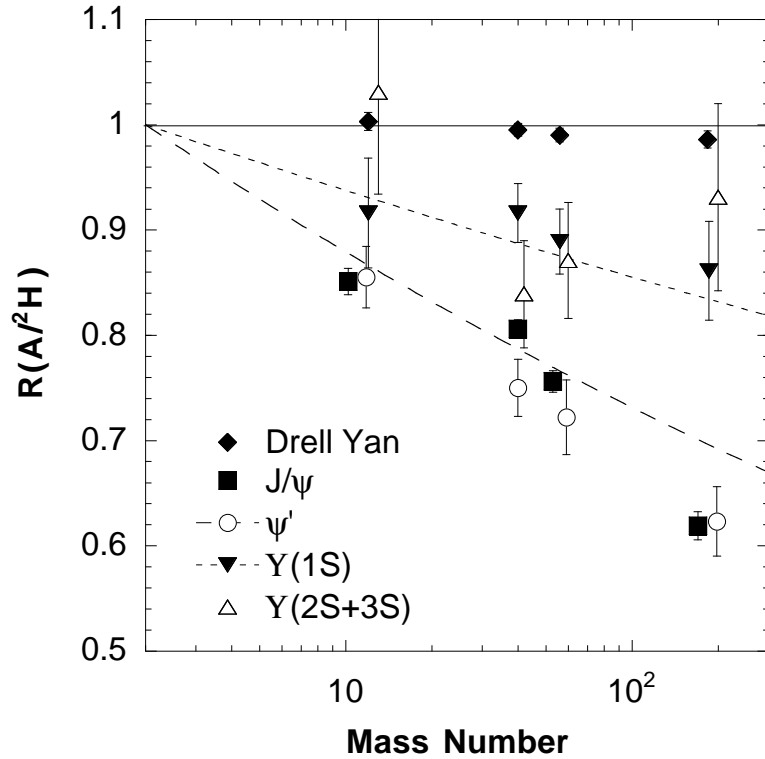


Figure 5.5: Integral yield Cronin ratio as a function of atomic weight in p+A fixed target experiment for Drell-Yan process, etc. This figure is from [95].

5.2 Baryon excess in Au+Au collisions

Now let's come to another important physics from d+Au collisions. We know that the $(p + \bar{p})/h$ ratio from minimum-bias Au+Au collisions [18] at a similar energy is about a factor of 2 higher than that in d+Au and p+p collisions for $p_T \gtrsim 2.0$ GeV/c.

This enhancement is most likely due to final-state effects in Au+Au collisions. There are many models trying to explain this baryon excess in Au+Au collisions [9, 24, 19, 20, 22, 23]. In the following baryon production mechanism will be discussed.

5.2.1 \bar{p}/p ratio vs p_T

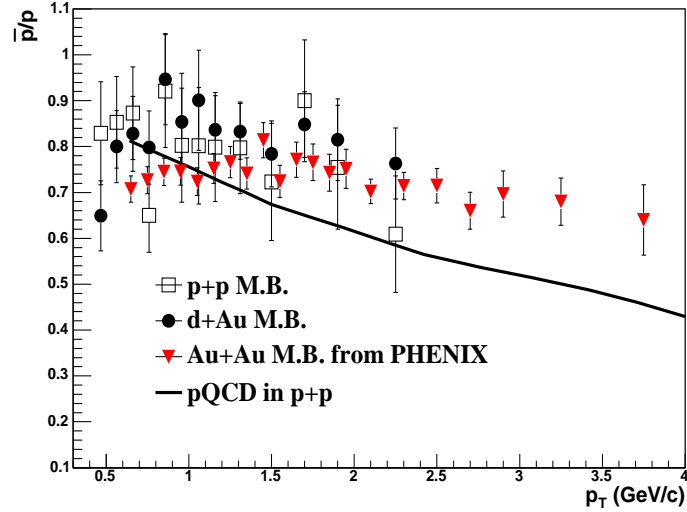


Figure 5.6: \bar{p}/p ratio as a function of p_T in d+Au and p+p minimum-bias collisions. The open squared symbols are for p+p collisions and the solid circled symbols for d+Au collisions. The triangled symbols represent the result from Au+Au minimum-bias collision [14]. The curve is the pQCD calculation results from [24] in p+p collisions. Errors are statistical.

In 200 GeV Au+Au collisions, \bar{p}/p ratio was observed to be flat with p_T till intermediate p_T range [14], as shown in Figure 5.6. The baryon junction model [24] tried to explain it by using junction anti-junction production with jet quenching, on the basis of pQCD calculation [24] where the \bar{p}/p ratio decreases with p_T in p+p collisions. The curve from pQCD calculation [24] is also shown in Figure 5.6. However, \bar{p}/p ratios in d+Au and p+p collisions in our data show to be flat with p_T within errors. Anyway, the precise measurement with more statistics in p+p and d+Au collisions is needed to address this issue.

5.2.2 Baryon production at RHIC: multi-gluon dynamics?

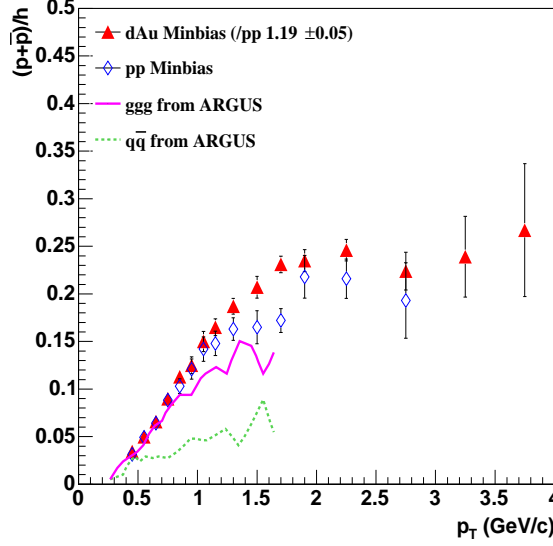


Figure 5.7: Minimum-bias ratios of $(p + \bar{p})$ over charged hadrons at $-0.5 < \eta < 0.0$ from $\sqrt{s_{NN}} = 200$ GeV p+p (open diamonds) and d+Au (filled triangles) collisions. Also shown are the $(p + \bar{p})/h$ ratios in e^+e^- collisions at ARGUS [96]. The solid line represents the $(p + \bar{p})/h$ ratio from three gluon hadronization while the dashed line for the ratio from quark and antiquark fragmentation [96]. Errors are statistical.

Let's compare the $(p + \bar{p})/h$ ratio in p+p, d+Au and Au+Au collisions at RHIC energy 200 GeV with the ratio in e^+e^- collisions at ARGUS [96]. Using the ARGUS detector at the e^+e^- storage ring DORIS II, the inclusive production of pion, kaon and proton in multihadron events at 9.98 GeV and in direct decays of the $\Upsilon(1S)$ meson were investigated [96]. Multihadron final states in e^+e^- annihilation are produced via quark and antiquark fragmentation, and those from direct $\Upsilon(1S)$ decays originate from the hadronization of three gluons [96]. Figure 5.7 shows the $(p + \bar{p})/h$ ratio in 200 GeV p+p collisions together with the ratio in e^+e^- collisions at ARGUS [96]. The plot shows that the $(p + \bar{p})/h$ ratio from three gluon hadronization is a factor of 3 higher than that from quark and antiquark fragmentation at ARGUS. Our data from 200 GeV p+p collisions is close to $(p + \bar{p})/h$ ratio from 3 gluon hadronization. This may be the indication that in the heavy ion collisions at RHIC energy, multi-gluon

hadronization plays an important role for the particle production.

Chapter 6

Conclusion and Outlook

6.1 Conclusion

In summary, we have reported the identified particle spectra of pions, kaons, protons and anti-protons at mid-rapidity from 200 GeV minimum-bias, centrality selected d+Au collisions and NSD p+p collisions. The time-of-flight detector, based on novel multi-gap resistive plate chamber technology, was used for particle identification. This is the first time that MRPC detector was installed to take data as a time-of-flight detector in the collider experiment. The calibration method was set up in the STAR experiment for the first time and has been applied to the data taken later successfully. The intrinsic timing resolution of the MRPC was 85 ps after the calibration. In 2003 run, the pion/kaon can be separated up to transverse momentum 1.6 GeV/c while proton can be identified up to 3.0 GeV/c.

The spectra of π^\pm , K^\pm , p and \bar{p} in d+Au and p+p collisions provide an important reference for those in Au+Au collisions. The initial state in d+Au collisions is similar to that in Au+Au collisions, and, it's believed that the quark-gluon plasma doesn't exist in d+Au collisions. These results from d+Au collisions are very important for us to judge whether the quark-gluon plasma exists in Au+Au collisions or not and to understand the property of the dense matter created in Au+Au collisions. We observe that the spectra of π^\pm , K^\pm , p and \bar{p} are considerably harder in d+Au than those in p+p collisions. In $\sqrt{s_{NN}} = 200$ GeV d+Au collisions, the R_{dAu} of protons rise faster

than R_{dAu} of pions and kaons. The R_{dAu} of proton is larger than 1 at intermediate p_T while the proton production follows binary scaling at the same p_T range in 200 GeV Au+Au collisions. These results further prove that the suppression observed in Au+Au collisions at intermediate and high p_T is due to final state interactions in a dense and dissipative medium produced during the collision and not due to the initial state wave function of the Au nucleus. Additionally, the particle-species dependence of the Cronin effect is found to be significantly smaller than that from lower energy p+A collisions. In $\sqrt{s_{NN}} = 200$ GeV d+Au collisions, the ratio of the nuclear modification factor R_{dAu} between $(p + \bar{p})$ and charged hadrons (h) in the p_T range $1.2 < p_T < 3.0$ GeV/c was measured to be $1.19 \pm 0.05(\text{stat}) \pm 0.03(\text{syst})$ in minimum-bias collisions. Both the R_{dAu} values and $(p + \bar{p})/h$ ratios show little centrality dependence, in contrast to previous measurements in Au+Au collisions at $\sqrt{s_{NN}} = 130$ and 200 GeV. The ratios of protons over charged hadrons in d+Au and p+p collisions are found to be about a factor of 2 lower than that from Au+Au collisions, indicating that the relative baryon enhancement observed in heavy ion collisions at RHIC is due to the final state effects in Au+Au collisions.

The identified particle spectra in d+Au and p+p collisions not only provide the reference for those in Au+Au collisions, but also provide a chance to see the mechanism of the Cronin effect itself clearly. Usually the Cronin effect has been explained to be the initial state effect only since 1970s [30]. However, we compare our pion and proton spectra in minimum-bias and centrality-selected d+Au collisions with the recombination model [92]. The recombination model can reproduce both the pion spectra and proton spectra. This recombination model is built on the hadronization process, which is a final-state effect, while the initial multiple parton scattering model [30] can't reproduce the difference of the Cronin effect between pions and protons. From these comparisons, we conclude that the Cronin effect in $\sqrt{s_{NN}} = 200$ GeV d+Au collisions is not the initial state effect only, and that final state effect plays an important role.

The integral yield dN/dy and $\langle p_T \rangle$ in p+p and d+Au collisions were estimated from the power law fit and thermal model fit. The integral yield R_{dAu} of π^\pm , K^\pm , p and \bar{p} are observed to be smaller than 1 while those of p and \bar{p} are close to 1. The

π^-/π^+ , K^-/K^+ and \bar{p}/p ratios as a function of p_T are observed to be flat with p_T within the errors in d+Au and p+p minimum-bias collisions and show little centrality dependence in d+Au collisions. The integral yield ratios of K^-/π^- and \bar{p}/π^- as a function of $dN/d\eta$ were also presented in p+p and d+Au collisions.

6.2 Outlook

For the outlook, I will discuss whether the Cronin effect is mass dependent or baryon/meson dependent at 200 GeV. What other physics topic have we done from MRPC-TOF in d+Au and p+p collisions in 2003 run? If we have the full time-of-flight (Full-TOF) coverage, what can we do? Also I will discuss a little bit about the low energy 63 GeV Au+Au run.

6.2.1 Cronin effect at 200 GeV: Mass dependent or baryon/meson dependent?

We know that recombination model can reproduce the spectra of pions and protons in d+Au collisions. Also the R_{CP} of identified particles in Au+Au collisions suggest that the degree of suppression depends on particle species(baryon/meson) at intermediate p_T . Does the Cronin effect in 200 GeV d+Au collisions depend on the particle species (baryon/meson) or depend on the particle mass? From our data, it shows the Cronin effect for proton is bigger than those for pion and kaon. And the Cronin effect of pion shows little difference from that of kaon at $p_T < 1.5$ GeV/c. In order to see the Cronin effect is baryon/meson dependent or mass dependent, we can compare the Cronin effect of proton with those of K^* and ϕ since the mass of K^* and ϕ are close to that of proton while K^* and ϕ are mesons and proton is a baryon. The preliminary results show that the Cronin effect of K^* and ϕ [97] are similar to that of pion and different from that of proton. However, the final results from K^* and ϕ are needed to confirm this issue.

6.2.2 Electron PID from MRPC-TOFr

The production and spectra of hadrons with heavy flavor are sensitive to initial conditions and the later stage dynamical evolution in high energy nuclear collisions, and may be less affected by the non-perturbative complication in theoretical calculations [100]. Charm production has been proposed as a sensitive measurement of parton distribution function in nucleon and the nuclear shadowing effect by systematically studying p+p, and p+A collisions [101]. The relatively reduced energy loss of heavy quark traversing a quark-gluon plasma will help us distinguish the medium in which the jet loses its energy [102]. A possible enhancement of charmonia (J/Ψ) production can be present at RHIC energies [103] due to the coalescence of the copiously produced charm quarks [99].

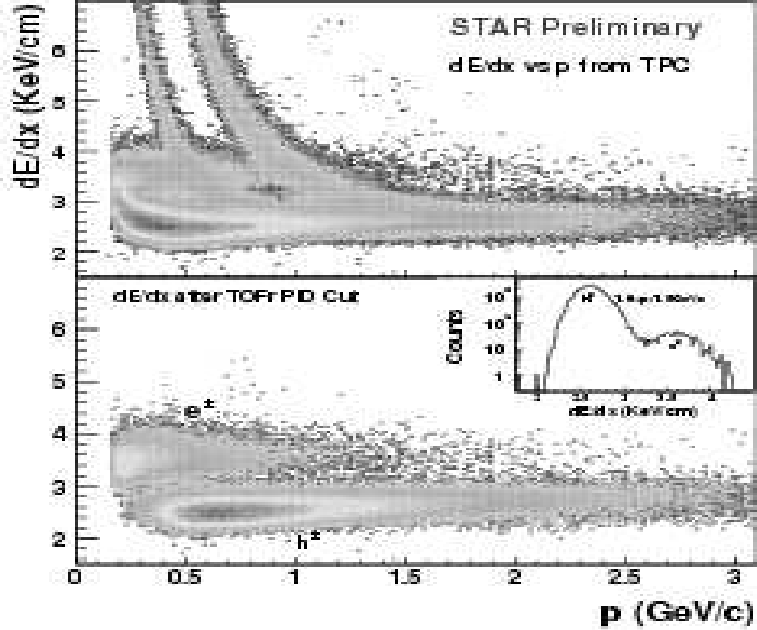


Figure 6.1: dE/dx in TPC versus p without (the upper panel) or with (the lower panel) the TOFr velocity cut $|1/\beta - 1| \leq 0.03$. The insert shows dE/dx distribution for $1 \leq p \leq 1.5$ GeV/c.

The recent STAR results on the absolute open charm cross section measurements from direct charmed hadron D^0 reconstruction [81] in d+Au collisions and electrons from charm semileptonic decay in both p+p and d+Au collisions at 200 GeV were

presented [99]. Based on the capability of hadron identification [98] from the MRPC-TOFr tray in 2003, electrons could be identified at low momentum ($p_T \leq 3$ GeV/c) by the combination of velocity (β) from TOFr [39] and the particle ionization energy loss (dE/dx) from TPC [38]. Figure 6.1 shows that the electrons are clearly identified as a separate band in the dE/dx versus momentum (p) with a selection on β at $|1/\beta - 1| \leq 0.03$ in d+Au collisions. At higher p_T (2–4 GeV/c), negative electrons were also identified directly by TPC since hadrons have lower dE/dx due to the relativistic rise of electron dE/dx . Based on the clear electron identification, the open-charm-decayed electron spectra was derived [99]. Combined with D^0 measurement from TPC, the total charm cross section was obtained [99] in d+Au collisions.

6.2.3 Full-TOF Physics

Based on the hadron PID and electron PID of MRPC-TOFr in 2003, we can imagine how many physics we can do if we have full time-of-flight coverage based on MRPC technology. The proposal [74] for large area time-of-flight system for STAR has been proposed. Since the pion/kaon can be separated up to transverse momentum 1.6 GeV/c and proton can be identified up to 3.0 GeV/c from time-of-flight system. The resonance spectra measured from hadronic decay will be extended to much higher p_T . The direct open charm spectra from its hadronic decay channel will reach higher p_T with much more precise measurement. Since the electron can be clearly identified up to transverse momentum 3~4 GeV/c by the combination of velocity (β) from TOFr [39] and the particle ionization energy loss (dE/dx) from TPC [38], the electron spectra from charm-semi-leptonic decay will be measured precisely. As we know that the measurement of the di-leptonic decays of vector mesons are very difficult since the branch ratios are too small and it's really hard to subtract the background. But with TOF upgrading together with the SVT and micro-vertex detector upgrading, the di-leptonic decays of vector mesons will be measured much more easily, which will bring the direct information of QGP since the electron is a lepton and the cross section of interaction between electrons and hadrons is little. Thus we can see directly the property of quark-gluon plasma such as the temperature and the chiral symmetry

restoration. This will be the most interesting and meaningful thing for the QGP search [94]. Besides, there are many other physics topics [74] such as identified particle correlation and fluctuation, particle composition of jet fragmentation, and anti-nuclei etc.

6.2.4 63 GeV Au+Au collisions at RHIC

The bulk properties such as elliptic flow v_2 and particle production show smooth trend from AGS, SPS to RHIC energy. One energy point $\sqrt{s_{NN}} = 63$ GeV, which is between SPS and full RHIC energy, was selected since high quality charged-particle and π^0 inclusive spectra have been measured in p+p collisions at 63 GeV at Intersecting Storage Rings (ISR) and will serve as the reference spectra for computing the nuclear modification factor for Au+Au collisions measured at the same energy. The v_2 and particle production at 63 GeV will be studied at RHIC. Besides, the nuclear modification factor as a function of p_T will also be studied in this collision system in which the hard scattering component has been significantly reduced. The results from 63 GeV Au+Au collisions will be helpful for us to understand the property of dense medium created in 200 GeV Au+Au collisions.

Appendix A

Tables of the Invariant Yields

p_T	p_T width	M.B.	0%-20%
3.50e-01	1.00e-01	$3.14e+00 \pm 3.65e-02 \pm 2.51e-01$	$6.70e+00 \pm 9.69e-02 \pm 5.36e-01$
4.50e-01	1.00e-01	$1.82e+00 \pm 2.45e-02 \pm 1.45e-01$	$3.88e+00 \pm 6.51e-02 \pm 3.10e-01$
5.50e-01	1.00e-01	$1.08e+00 \pm 1.73e-02 \pm 8.67e-02$	$2.38e+00 \pm 4.68e-02 \pm 1.90e-01$
6.50e-01	1.00e-01	$6.18e-01 \pm 1.22e-02 \pm 4.94e-02$	$1.38e+00 \pm 3.28e-02 \pm 1.10e-01$
7.50e-01	1.00e-01	$4.13e-01 \pm 9.15e-03 \pm 3.31e-02$	$9.53e-01 \pm 2.56e-02 \pm 7.63e-02$
8.50e-01	1.00e-01	$2.66e-01 \pm 6.98e-03 \pm 2.13e-02$	$6.11e-01 \pm 1.93e-02 \pm 4.88e-02$
9.50e-01	1.00e-01	$1.70e-01 \pm 5.36e-03 \pm 1.36e-02$	$3.79e-01 \pm 1.44e-02 \pm 3.03e-02$
1.05e+00	1.00e-01	$1.14e-01 \pm 4.07e-03 \pm 9.09e-03$	$2.68e-01 \pm 1.15e-02 \pm 2.14e-02$
1.15e+00	1.00e-01	$7.70e-02 \pm 3.27e-03 \pm 6.16e-03$	$1.71e-01 \pm 8.82e-03 \pm 1.37e-02$
1.30e+00	2.00e-01	$4.43e-02 \pm 1.66e-03 \pm 3.55e-03$	$1.06e-01 \pm 4.71e-03 \pm 8.45e-03$
1.50e+00	2.00e-01	$2.10e-02 \pm 1.07e-03 \pm 1.68e-03$	$4.65e-02 \pm 2.96e-03 \pm 3.72e-03$
1.70e+00	2.00e-01	$1.05e-02 \pm 7.19e-04 \pm 8.40e-04$	$2.29e-02 \pm 1.92e-03 \pm 1.83e-03$

Table A.1: π^+ spectra in minimum-bias and 0-20% d+Au collisions. The unit of p_T and p_T width is GeV/c .

p_T	p_T width	20%-40%	40%-100%
3.50e-01	1.00e-01	$4.73e+00 \pm 6.94e-02 \pm 3.78e-01$	$1.93e+00 \pm 2.85e-02 \pm 1.55e-01$
4.50e-01	1.00e-01	$2.80e+00 \pm 4.73e-02 \pm 2.24e-01$	$1.10e+00 \pm 1.89e-02 \pm 8.81e-02$
5.50e-01	1.00e-01	$1.68e+00 \pm 3.36e-02 \pm 1.34e-01$	$6.43e-01 \pm 1.31e-02 \pm 5.14e-02$
6.50e-01	1.00e-01	$9.50e-01 \pm 2.30e-02 \pm 7.60e-02$	$3.68e-01 \pm 9.03e-03 \pm 2.94e-02$
7.50e-01	1.00e-01	$6.41e-01 \pm 1.76e-02 \pm 5.13e-02$	$2.40e-01 \pm 6.80e-03 \pm 1.92e-02$
8.50e-01	1.00e-01	$4.20e-01 \pm 1.36e-02 \pm 3.36e-02$	$1.52e-01 \pm 5.09e-03 \pm 1.22e-02$
9.50e-01	1.00e-01	$2.58e-01 \pm 1.00e-02 \pm 2.07e-02$	$1.01e-01 \pm 3.97e-03 \pm 8.05e-03$
1.05e+00	1.00e-01	$1.80e-01 \pm 7.92e-03 \pm 1.44e-02$	$6.10e-02 \pm 2.84e-03 \pm 4.88e-03$
1.15e+00	1.00e-01	$1.21e-01 \pm 6.35e-03 \pm 9.72e-03$	$4.38e-02 \pm 2.37e-03 \pm 3.50e-03$
1.30e+00	2.00e-01	$6.49e-02 \pm 3.02e-03 \pm 5.19e-03$	$2.40e-02 \pm 1.16e-03 \pm 1.92e-03$
1.50e+00	2.00e-01	$3.28e-02 \pm 2.05e-03 \pm 2.63e-03$	$1.03e-02 \pm 7.12e-04 \pm 8.27e-04$
1.70e+00	2.00e-01	$1.57e-02 \pm 1.31e-03 \pm 1.26e-03$	$4.92e-03 \pm 4.49e-04 \pm 3.94e-04$

Table A.2: π^+ spectra in 20-40% and 40-100% d+Au collisions. The unit of p_T and p_T width is GeV/c .

p_T	p_T width	p+p
3.50e-01	1.00e-01	$9.71e-01 \pm 1.21e-02 \pm 7.76e-02$
4.50e-01	1.00e-01	$5.32e-01 \pm 7.84e-03 \pm 4.26e-02$
5.50e-01	1.00e-01	$3.14e-01 \pm 5.46e-03 \pm 2.51e-02$
6.50e-01	1.00e-01	$1.74e-01 \pm 3.72e-03 \pm 1.40e-02$
7.50e-01	1.00e-01	$1.08e-01 \pm 2.65e-03 \pm 8.64e-03$
8.50e-01	1.00e-01	$6.42e-02 \pm 1.89e-03 \pm 5.14e-03$
9.50e-01	1.00e-01	$4.03e-02 \pm 1.42e-03 \pm 3.22e-03$
1.05e+00	1.00e-01	$2.40e-02 \pm 9.94e-04 \pm 1.92e-03$
1.15e+00	1.00e-01	$1.55e-02 \pm 7.71e-04 \pm 1.24e-03$
1.30e+00	2.00e-01	$8.19e-03 \pm 3.86e-04 \pm 6.55e-04$
1.50e+00	2.00e-01	$3.77e-03 \pm 2.46e-04 \pm 3.02e-04$
1.70e+00	2.00e-01	$1.84e-03 \pm 1.96e-04 \pm 1.47e-04$

Table A.3: π^+ spectra in p+p collisions. The unit of p_T and p_T width is GeV/c .

p_T	p_T width	M.B.	0%-20%
3.50e-01	1.00e-01	$3.20e+00 \pm 3.73e-02 \pm 2.56e-01$	$6.77e+00 \pm 9.88e-02 \pm 5.42e-01$
4.50e-01	1.00e-01	$1.82e+00 \pm 2.46e-02 \pm 1.45e-01$	$3.92e+00 \pm 6.60e-02 \pm 3.13e-01$
5.50e-01	1.00e-01	$1.08e+00 \pm 1.72e-02 \pm 8.60e-02$	$2.42e+00 \pm 4.71e-02 \pm 1.94e-01$
6.50e-01	1.00e-01	$6.70e-01 \pm 1.30e-02 \pm 5.36e-02$	$1.49e+00 \pm 3.51e-02 \pm 1.20e-01$
7.50e-01	1.00e-01	$4.05e-01 \pm 9.06e-03 \pm 3.24e-02$	$9.22e-01 \pm 2.50e-02 \pm 7.38e-02$
8.50e-01	1.00e-01	$2.59e-01 \pm 6.89e-03 \pm 2.07e-02$	$6.13e-01 \pm 1.96e-02 \pm 4.91e-02$
9.50e-01	1.00e-01	$1.68e-01 \pm 5.38e-03 \pm 1.34e-02$	$3.85e-01 \pm 1.48e-02 \pm 3.08e-02$
1.05e+00	1.00e-01	$1.16e-01 \pm 4.23e-03 \pm 9.29e-03$	$2.70e-01 \pm 1.18e-02 \pm 2.16e-02$
1.15e+00	1.00e-01	$7.63e-02 \pm 3.28e-03 \pm 6.11e-03$	$1.71e-01 \pm 8.83e-03 \pm 1.37e-02$
1.30e+00	2.00e-01	$4.36e-02 \pm 1.66e-03 \pm 3.49e-03$	$9.67e-02 \pm 4.45e-03 \pm 7.73e-03$
1.50e+00	2.00e-01	$2.04e-02 \pm 1.07e-03 \pm 1.63e-03$	$4.94e-02 \pm 3.06e-03 \pm 3.96e-03$
1.70e+00	2.00e-01	$1.03e-02 \pm 7.23e-04 \pm 8.26e-04$	$2.54e-02 \pm 2.07e-03 \pm 2.03e-03$

Table A.4: π^- spectra in minimum-bias and 0-20% d+Au collisions. The unit of p_T and p_T width is GeV/c .

p_T	p_T width	20%-40%	40%-100%
3.50e-01	1.00e-01	$4.81e+00 \pm 7.11e-02 \pm 3.85e-01$	$2.00e+00 \pm 2.95e-02 \pm 1.60e-01$
4.50e-01	1.00e-01	$2.76e+00 \pm 4.73e-02 \pm 2.21e-01$	$1.12e+00 \pm 1.93e-02 \pm 8.95e-02$
5.50e-01	1.00e-01	$1.65e+00 \pm 3.28e-02 \pm 1.32e-01$	$6.43e-01 \pm 1.31e-02 \pm 5.14e-02$
6.50e-01	1.00e-01	$1.03e+00 \pm 2.47e-02 \pm 8.23e-02$	$4.04e-01 \pm 9.83e-03 \pm 3.23e-02$
7.50e-01	1.00e-01	$6.15e-01 \pm 1.71e-02 \pm 4.92e-02$	$2.40e-01 \pm 6.80e-03 \pm 1.92e-02$
8.50e-01	1.00e-01	$3.92e-01 \pm 1.30e-02 \pm 3.13e-02$	$1.51e-01 \pm 5.10e-03 \pm 1.21e-02$
9.50e-01	1.00e-01	$2.61e-01 \pm 1.03e-02 \pm 2.09e-02$	$9.62e-02 \pm 3.91e-03 \pm 7.70e-03$
1.05e+00	1.00e-01	$1.81e-01 \pm 8.11e-03 \pm 1.45e-02$	$6.65e-02 \pm 3.07e-03 \pm 5.32e-03$
1.15e+00	1.00e-01	$1.20e-01 \pm 6.26e-03 \pm 9.58e-03$	$4.23e-02 \pm 2.31e-03 \pm 3.38e-03$
1.30e+00	2.00e-01	$6.82e-02 \pm 3.18e-03 \pm 5.46e-03$	$2.42e-02 \pm 1.18e-03 \pm 1.93e-03$
1.50e+00	2.00e-01	$3.24e-02 \pm 2.13e-03 \pm 2.59e-03$	$1.05e-02 \pm 7.69e-04 \pm 8.42e-04$
1.70e+00	2.00e-01	$1.55e-02 \pm 1.34e-03 \pm 1.24e-03$	$5.02e-03 \pm 1.06e-03 \pm 4.01e-04$

Table A.5: π^- spectra in 20-40% and 40-100% d+Au collisions. The unit of p_T and p_T width is GeV/c .

p_T	p_T width	p+p
3.50e-01	1.00e-01	$9.71e-01 \pm 1.22e-02 \pm 7.76e-02$
4.50e-01	1.00e-01	$5.47e-01 \pm 8.02e-03 \pm 4.37e-02$
5.50e-01	1.00e-01	$3.09e-01 \pm 5.38e-03 \pm 2.47e-02$
6.50e-01	1.00e-01	$1.84e-01 \pm 3.89e-03 \pm 1.47e-02$
7.50e-01	1.00e-01	$1.00e-01 \pm 2.50e-03 \pm 8.01e-03$
8.50e-01	1.00e-01	$6.36e-02 \pm 1.89e-03 \pm 5.09e-03$
9.50e-01	1.00e-01	$3.80e-02 \pm 1.38e-03 \pm 3.04e-03$
1.05e+00	1.00e-01	$2.44e-02 \pm 1.03e-03 \pm 1.95e-03$
1.15e+00	1.00e-01	$1.57e-02 \pm 7.87e-04 \pm 1.25e-03$
1.30e+00	2.00e-01	$8.70e-03 \pm 4.02e-04 \pm 6.96e-04$
1.50e+00	2.00e-01	$3.62e-03 \pm 2.45e-04 \pm 2.90e-04$
1.70e+00	2.00e-01	$1.69e-03 \pm 1.76e-04 \pm 1.35e-04$

Table A.6: π^- spectra in p+p collisions. The unit of p_T and p_T width is GeV/c .

p_T	p_T width	M.B.	0%-20%
4.57e-01	1.00e-01	$2.41e-01 \pm 9.47e-03 \pm 1.93e-02$	$4.83e-01 \pm 2.75e-02 \pm 3.86e-02$
5.56e-01	1.00e-01	$1.87e-01 \pm 7.53e-03 \pm 1.49e-02$	$3.87e-01 \pm 2.14e-02 \pm 3.10e-02$
6.55e-01	1.00e-01	$1.33e-01 \pm 5.14e-03 \pm 1.07e-02$	$2.81e-01 \pm 1.53e-02 \pm 2.25e-02$
7.54e-01	1.00e-01	$1.01e-01 \pm 3.18e-03 \pm 8.07e-03$	$2.14e-01 \pm 1.09e-02 \pm 1.72e-02$
8.54e-01	1.00e-01	$6.97e-02 \pm 2.48e-03 \pm 5.57e-03$	$1.58e-01 \pm 8.74e-03 \pm 1.27e-02$
9.54e-01	1.00e-01	$5.01e-02 \pm 1.95e-03 \pm 4.01e-03$	$9.95e-02 \pm 6.30e-03 \pm 7.96e-03$
1.05e+00	1.00e-01	$3.77e-02 \pm 1.65e-03 \pm 3.02e-03$	$8.92e-02 \pm 5.83e-03 \pm 7.14e-03$
1.15e+00	1.00e-01	$2.73e-02 \pm 1.31e-03 \pm 2.18e-03$	$5.61e-02 \pm 4.30e-03 \pm 4.49e-03$
1.30e+00	2.00e-01	$1.78e-02 \pm 7.25e-04 \pm 1.42e-03$	$4.00e-02 \pm 2.49e-03 \pm 3.20e-03$
1.50e+00	2.00e-01	$9.12e-03 \pm 5.25e-04 \pm 7.30e-04$	$1.95e-02 \pm 1.89e-03 \pm 1.56e-03$
1.70e+00	2.00e-01	$4.68e-03 \pm 3.96e-04 \pm 3.75e-04$	— — —

Table A.7: K^+ spectra in minimum-bias and 0-20% d+Au collisions. The unit of p_T and p_T width is GeV/c .

p_T	p_T width	20%-40%	40%-100%
4.57e-01	1.00e-01	$3.63e-01 \pm 2.06e-02 \pm 2.91e-02$	$1.27e-01 \pm 7.70e-03 \pm 1.02e-02$
5.56e-01	1.00e-01	$2.74e-01 \pm 1.54e-02 \pm 2.19e-02$	$1.07e-01 \pm 6.16e-03 \pm 8.60e-03$
6.55e-01	1.00e-01	$2.01e-01 \pm 1.11e-02 \pm 1.60e-02$	$7.37e-02 \pm 4.26e-03 \pm 5.89e-03$
7.54e-01	1.00e-01	$1.58e-01 \pm 8.18e-03 \pm 1.27e-02$	$5.25e-02 \pm 2.99e-03 \pm 4.20e-03$
8.54e-01	1.00e-01	$1.01e-01 \pm 6.16e-03 \pm 8.06e-03$	$3.73e-02 \pm 2.35e-03 \pm 2.98e-03$
9.54e-01	1.00e-01	$7.97e-02 \pm 4.89e-03 \pm 6.37e-03$	$2.80e-02 \pm 1.86e-03 \pm 2.24e-03$
1.05e+00	1.00e-01	$5.34e-02 \pm 3.83e-03 \pm 4.27e-03$	$1.91e-02 \pm 1.47e-03 \pm 1.52e-03$
1.15e+00	1.00e-01	$3.91e-02 \pm 3.12e-03 \pm 3.13e-03$	$1.36e-02 \pm 1.18e-03 \pm 1.09e-03$
1.30e+00	2.00e-01	$2.51e-02 \pm 1.67e-03 \pm 2.01e-03$	$8.65e-03 \pm 6.83e-04 \pm 6.92e-04$
1.50e+00	2.00e-01	$1.32e-02 \pm 1.19e-03 \pm 1.05e-03$	$4.69e-03 \pm 5.07e-04 \pm 3.75e-04$

Table A.8: K^+ spectra in 20-40% and 40-100% d+Au collisions. The unit of p_T and p_T width is GeV/c .

p_T	p_T width	p+p
4.57e-01	1.00e-01	$6.47e-02 \pm 3.01e-03 \pm 5.18e-03$
5.56e-01	1.00e-01	$4.32e-02 \pm 2.10e-03 \pm 3.45e-03$
6.55e-01	1.00e-01	$3.18e-02 \pm 1.51e-03 \pm 2.54e-03$
7.54e-01	1.00e-01	$2.18e-02 \pm 9.70e-04 \pm 1.74e-03$
8.54e-01	1.00e-01	$1.57e-02 \pm 7.69e-04 \pm 1.25e-03$
9.54e-01	1.00e-01	$9.92e-03 \pm 5.60e-04 \pm 7.93e-04$
1.05e+00	1.00e-01	$7.17e-03 \pm 4.74e-04 \pm 5.74e-04$
1.15e+00	1.00e-01	$5.60e-03 \pm 4.18e-04 \pm 4.48e-04$
1.30e+00	2.00e-01	$3.73e-03 \pm 2.72e-04 \pm 2.98e-04$
1.50e+00	2.00e-01	$1.81e-03 \pm 1.18e-04 \pm 1.45e-04$

Table A.9: K^+ spectra in p+p collisions. The unit of p_T and p_T width is GeV/c .

p_T	p_T width	M.B.	0%-20%
4.57e-01	1.00e-01	$2.34e-01 \pm 9.47e-03 \pm 1.87e-02$	$4.87e-01 \pm 2.81e-02 \pm 3.90e-02$
5.56e-01	1.00e-01	$1.92e-01 \pm 7.98e-03 \pm 1.54e-02$	$4.01e-01 \pm 2.28e-02 \pm 3.21e-02$
6.55e-01	1.00e-01	$1.39e-01 \pm 5.81e-03 \pm 1.12e-02$	$2.91e-01 \pm 1.69e-02 \pm 2.33e-02$
7.54e-01	1.00e-01	$9.21e-02 \pm 3.10e-03 \pm 7.37e-03$	$1.90e-01 \pm 1.04e-02 \pm 1.52e-02$
8.54e-01	1.00e-01	$7.11e-02 \pm 2.61e-03 \pm 5.69e-03$	$1.45e-01 \pm 8.76e-03 \pm 1.16e-02$
9.54e-01	1.00e-01	$4.70e-02 \pm 1.94e-03 \pm 3.76e-03$	$9.49e-02 \pm 6.34e-03 \pm 7.59e-03$
1.05e+00	1.00e-01	$3.11e-02 \pm 1.49e-03 \pm 2.48e-03$	$6.56e-02 \pm 5.07e-03 \pm 5.25e-03$
1.15e+00	1.00e-01	$2.28e-02 \pm 1.21e-03 \pm 1.82e-03$	$4.74e-02 \pm 4.00e-03 \pm 3.79e-03$
1.30e+00	2.00e-01	$1.61e-02 \pm 7.10e-04 \pm 1.29e-03$	$3.70e-02 \pm 2.41e-03 \pm 2.96e-03$
1.50e+00	2.00e-01	$9.47e-03 \pm 5.54e-04 \pm 7.58e-04$	$2.01e-02 \pm 1.78e-03 \pm 1.61e-03$
1.70e+00	2.00e-01	$4.44e-03 \pm 4.19e-04 \pm 3.55e-04$	— — —

Table A.10: K^- spectra in minimum-bias and 0-20% d+Au collisions. The unit of p_T and p_T width is GeV/c .

p_T	p_T width	20%-40%	40%-100%
4.57e-01	1.00e-01	$3.24e-01 \pm 1.95e-02 \pm 2.59e-02$	$1.39e-01 \pm 8.25e-03 \pm 1.11e-02$
5.56e-01	1.00e-01	$2.66e-01 \pm 1.58e-02 \pm 2.13e-02$	$1.13e-01 \pm 6.63e-03 \pm 9.03e-03$
6.55e-01	1.00e-01	$1.99e-01 \pm 1.18e-02 \pm 1.59e-02$	$7.50e-02 \pm 4.61e-03 \pm 6.00e-03$
7.54e-01	1.00e-01	$1.36e-01 \pm 7.60e-03 \pm 1.08e-02$	$5.62e-02 \pm 3.16e-03 \pm 4.50e-03$
8.54e-01	1.00e-01	$1.13e-01 \pm 6.64e-03 \pm 9.04e-03$	$3.78e-02 \pm 2.47e-03 \pm 3.03e-03$
9.54e-01	1.00e-01	$7.35e-02 \pm 4.83e-03 \pm 5.88e-03$	$2.55e-02 \pm 1.82e-03 \pm 2.04e-03$
1.05e+00	1.00e-01	$4.51e-02 \pm 3.57e-03 \pm 3.61e-03$	$1.93e-02 \pm 1.51e-03 \pm 1.54e-03$
1.15e+00	1.00e-01	$3.03e-02 \pm 2.74e-03 \pm 2.43e-03$	$1.36e-02 \pm 1.20e-03 \pm 1.09e-03$
1.30e+00	2.00e-01	$2.35e-02 \pm 1.66e-03 \pm 1.88e-03$	$7.84e-03 \pm 6.41e-04 \pm 6.27e-04$
1.50e+00	2.00e-01	$1.05e-02 \pm 1.20e-03 \pm 8.36e-04$	$5.10e-03 \pm 5.72e-04 \pm 4.08e-04$

Table A.11: K^- spectra in 20-40% and 40-100% d+Au collisions. The unit of p_T and p_T width is GeV/c .

p_T	p_T width	p+p
4.57e-01	1.00e-01	$5.99e-02 \pm 2.91e-03 \pm 4.79e-03$
5.56e-01	1.00e-01	$4.79e-02 \pm 2.35e-03 \pm 3.83e-03$
6.55e-01	1.00e-01	$3.06e-02 \pm 1.58e-03 \pm 2.45e-03$
7.54e-01	1.00e-01	$2.15e-02 \pm 9.81e-04 \pm 1.72e-03$
8.54e-01	1.00e-01	$1.46e-02 \pm 7.67e-04 \pm 1.17e-03$
9.54e-01	1.00e-01	$1.01e-02 \pm 5.86e-04 \pm 8.09e-04$
1.05e+00	1.00e-01	$7.87e-03 \pm 5.22e-04 \pm 6.30e-04$
1.15e+00	1.00e-01	$5.25e-03 \pm 4.27e-04 \pm 4.20e-04$
1.30e+00	2.00e-01	$3.42e-03 \pm 2.57e-04 \pm 2.74e-04$
1.50e+00	2.00e-01	$1.75e-03 \pm 1.61e-04 \pm 1.40e-04$

Table A.12: K^- spectra in p+p collisions. The unit of p_T and p_T width is GeV/c .

p_T	p_T width	M.B.	0%-20%
4.68e-01	1.00e-01	$1.88e-01 \pm 1.87e-02 \pm 2.44e-02$	$3.96e-01 \pm 4.51e-02 \pm 5.15e-02$
5.63e-01	1.00e-01	$1.35e-01 \pm 1.11e-02 \pm 1.75e-02$	$2.80e-01 \pm 2.67e-02 \pm 3.64e-02$
6.61e-01	1.00e-01	$1.07e-01 \pm 8.89e-03 \pm 1.39e-02$	$2.10e-01 \pm 2.01e-02 \pm 2.73e-02$
7.59e-01	1.00e-01	$8.02e-02 \pm 6.78e-03 \pm 1.04e-02$	$1.74e-01 \pm 1.67e-02 \pm 2.27e-02$
8.58e-01	1.00e-01	$5.82e-02 \pm 5.20e-03 \pm 7.57e-03$	$1.25e-01 \pm 1.27e-02 \pm 1.63e-02$
9.57e-01	1.00e-01	$4.45e-02 \pm 4.85e-03 \pm 5.78e-03$	$1.05e-01 \pm 1.25e-02 \pm 1.37e-02$
1.06e+00	1.00e-01	$3.63e-02 \pm 4.11e-03 \pm 2.90e-03$	$8.16e-02 \pm 1.02e-02 \pm 6.53e-03$
1.16e+00	1.00e-01	$2.82e-02 \pm 2.11e-03 \pm 2.26e-03$	$5.08e-02 \pm 5.11e-03 \pm 4.06e-03$
1.31e+00	2.00e-01	$1.86e-02 \pm 1.14e-03 \pm 1.49e-03$	$4.14e-02 \pm 3.21e-03 \pm 3.31e-03$
1.50e+00	2.00e-01	$1.02e-02 \pm 7.85e-04 \pm 8.14e-04$	$2.46e-02 \pm 2.34e-03 \pm 1.97e-03$
1.70e+00	2.00e-01	$5.64e-03 \pm 3.24e-04 \pm 4.51e-04$	$1.21e-02 \pm 1.03e-03 \pm 9.66e-04$
1.90e+00	2.00e-01	$3.14e-03 \pm 2.33e-04 \pm 2.51e-04$	$8.08e-03 \pm 8.38e-04 \pm 6.46e-04$
2.25e+00	5.00e-01	$1.39e-03 \pm 9.47e-05 \pm 1.12e-04$	$3.37e-03 \pm 3.21e-04 \pm 2.70e-04$
2.75e+00	5.00e-01	$2.75e-04 \pm 3.88e-05 \pm 2.20e-05$	$6.19e-04 \pm 1.26e-04 \pm 4.95e-05$
3.50e+00	1.00e+00	$8.13e-05 \pm 1.37e-05 \pm 6.50e-06$	---

Table A.13: p spectra in minimum-bias and 0-20% d+Au collisions. The unit of p_T and p_T width is GeV/c .

p_T	p_T width	20%-40%	40%-100%
4.68e-01	1.00e-01	$2.78e-01 \pm 3.24e-02 \pm 3.61e-02$	$1.21e-01 \pm 1.40e-02 \pm 1.57e-02$
5.63e-01	1.00e-01	$1.90e-01 \pm 1.84e-02 \pm 2.48e-02$	$7.84e-02 \pm 7.61e-03 \pm 1.02e-02$
6.61e-01	1.00e-01	$1.56e-01 \pm 1.49e-02 \pm 2.03e-02$	$6.18e-02 \pm 5.96e-03 \pm 8.03e-03$
7.59e-01	1.00e-01	$1.18e-01 \pm 1.14e-02 \pm 1.53e-02$	$4.84e-02 \pm 4.71e-03 \pm 6.29e-03$
8.58e-01	1.00e-01	$8.54e-02 \pm 8.68e-03 \pm 1.11e-02$	$2.98e-02 \pm 3.12e-03 \pm 3.87e-03$
9.57e-01	1.00e-01	$6.45e-02 \pm 7.77e-03 \pm 8.38e-03$	$2.39e-02 \pm 2.93e-03 \pm 3.11e-03$
1.06e+00	1.00e-01	$5.48e-02 \pm 6.88e-03 \pm 4.38e-03$	$2.12e-02 \pm 2.69e-03 \pm 1.69e-03$
1.16e+00	1.00e-01	$4.21e-02 \pm 3.97e-03 \pm 3.37e-03$	$1.52e-02 \pm 1.49e-03 \pm 1.22e-03$
1.31e+00	2.00e-01	$2.68e-02 \pm 2.09e-03 \pm 2.15e-03$	$9.80e-03 \pm 7.91e-04 \pm 7.84e-04$
1.50e+00	2.00e-01	$1.41e-02 \pm 1.38e-03 \pm 1.13e-03$	$5.05e-03 \pm 5.17e-04 \pm 4.04e-04$
1.70e+00	2.00e-01	$7.69e-03 \pm 7.02e-04 \pm 6.15e-04$	$2.54e-03 \pm 2.55e-04 \pm 2.03e-04$
1.90e+00	2.00e-01	$4.12e-03 \pm 5.31e-04 \pm 3.30e-04$	$1.43e-03 \pm 2.03e-04 \pm 1.15e-04$
2.25e+00	5.00e-01	$2.30e-03 \pm 2.28e-04 \pm 1.84e-04$	$6.31e-04 \pm 7.57e-05 \pm 5.05e-05$
2.75e+00	5.00e-01	$4.36e-04 \pm 1.13e-04 \pm 3.49e-05$	$1.62e-04 \pm 4.14e-05 \pm 1.29e-05$

Table A.14: p spectra in 20-40% and 40-100% d+Au collisions. The unit of p_T and p_T width is GeV/c .

p_T	p_T width	p+p
4.68e-01	1.00e-01	$4.51e-02 \pm 5.24e-03 \pm 5.86e-03$
5.63e-01	1.00e-01	$3.33e-02 \pm 3.29e-03 \pm 4.33e-03$
6.61e-01	1.00e-01	$2.60e-02 \pm 2.57e-03 \pm 3.38e-03$
7.59e-01	1.00e-01	$2.03e-02 \pm 2.12e-03 \pm 2.64e-03$
8.58e-01	1.00e-01	$1.14e-02 \pm 1.30e-03 \pm 1.49e-03$
9.57e-01	1.00e-01	$8.93e-03 \pm 1.20e-03 \pm 1.16e-03$
1.06e+00	1.00e-01	$6.98e-03 \pm 1.00e-03 \pm 5.59e-04$
1.16e+00	1.00e-01	$4.68e-03 \pm 5.95e-04 \pm 3.75e-04$
1.31e+00	2.00e-01	$2.90e-03 \pm 3.14e-04 \pm 2.32e-04$
1.50e+00	2.00e-01	$1.34e-03 \pm 2.04e-04 \pm 1.07e-04$
1.70e+00	2.00e-01	$6.61e-04 \pm 6.44e-05 \pm 5.29e-05$
1.90e+00	2.00e-01	$4.73e-04 \pm 5.58e-05 \pm 3.78e-05$
2.25e+00	5.00e-01	$1.84e-04 \pm 2.23e-05 \pm 1.47e-05$
2.75e+00	5.00e-01	$3.06e-05 \pm 7.26e-06 \pm 2.45e-06$

Table A.15: p spectra in p+p collisions. The unit of p_T and p_T width is GeV/c .

p_T	p_T width	M.B.	0%-20%
4.68e-01	1.00e-01	$1.22e-01 \pm 7.62e-03 \pm 1.59e-02$	$2.57e-01 \pm 2.17e-02 \pm 3.34e-02$
5.63e-01	1.00e-01	$1.08e-01 \pm 5.87e-03 \pm 1.40e-02$	$2.26e-01 \pm 1.62e-02 \pm 2.94e-02$
6.61e-01	1.00e-01	$8.86e-02 \pm 4.69e-03 \pm 1.15e-02$	$1.73e-01 \pm 1.23e-02 \pm 2.25e-02$
7.59e-01	1.00e-01	$6.40e-02 \pm 3.47e-03 \pm 8.32e-03$	$1.39e-01 \pm 9.76e-03 \pm 1.81e-02$
8.58e-01	1.00e-01	$5.51e-02 \pm 3.04e-03 \pm 7.16e-03$	$1.19e-01 \pm 8.58e-03 \pm 1.54e-02$
9.57e-01	1.00e-01	$3.80e-02 \pm 2.30e-03 \pm 4.94e-03$	$8.99e-02 \pm 6.92e-03 \pm 1.17e-02$
1.06e+00	1.00e-01	$3.27e-02 \pm 1.41e-03 \pm 2.62e-03$	$7.36e-02 \pm 5.01e-03 \pm 5.89e-03$
1.16e+00	1.00e-01	$2.36e-02 \pm 1.12e-03 \pm 1.89e-03$	$4.24e-02 \pm 3.50e-03 \pm 3.39e-03$
1.31e+00	2.00e-01	$1.55e-02 \pm 6.16e-04 \pm 1.24e-03$	$3.48e-02 \pm 2.14e-03 \pm 2.78e-03$
1.50e+00	2.00e-01	$8.00e-03 \pm 4.04e-04 \pm 6.40e-04$	$1.93e-02 \pm 1.46e-03 \pm 1.54e-03$
1.70e+00	2.00e-01	$4.78e-03 \pm 2.97e-04 \pm 3.82e-04$	$1.01e-02 \pm 9.74e-04 \pm 8.11e-04$
1.90e+00	2.00e-01	$2.56e-03 \pm 2.04e-04 \pm 2.05e-04$	$4.99e-03 \pm 6.54e-04 \pm 3.99e-04$
2.25e+00	5.00e-01	$1.06e-03 \pm 7.97e-05 \pm 8.49e-05$	$2.69e-03 \pm 2.85e-04 \pm 2.15e-04$
2.75e+00	5.00e-01	$3.32e-04 \pm 4.61e-05 \pm 2.66e-05$	$5.86e-04 \pm 1.35e-04 \pm 4.69e-05$
3.50e+00	1.00e+00	$7.89e-05 \pm 1.53e-05 \pm 6.31e-06$	---

Table A.16: \bar{p} spectra in minimum-bias and 0-20% d+Au collisions. The unit of p_T and p_T width is GeV/c .

p_T	p_T width	20%-40%	40%-100%
4.68e-01	1.00e-01	$1.63e-01 \pm 1.45e-02 \pm 2.12e-02$	$7.50e-02 \pm 6.44e-03 \pm 9.75e-03$
5.63e-01	1.00e-01	$1.65e-01 \pm 1.20e-02 \pm 2.14e-02$	$6.04e-02 \pm 4.55e-03 \pm 7.85e-03$
6.61e-01	1.00e-01	$1.24e-01 \pm 8.94e-03 \pm 1.62e-02$	$5.51e-02 \pm 3.89e-03 \pm 7.16e-03$
7.59e-01	1.00e-01	$9.35e-02 \pm 6.78e-03 \pm 1.22e-02$	$3.61e-02 \pm 2.68e-03 \pm 4.69e-03$
8.58e-01	1.00e-01	$7.98e-02 \pm 5.96e-03 \pm 1.04e-02$	$2.85e-02 \pm 2.22e-03 \pm 3.70e-03$
9.57e-01	1.00e-01	$5.22e-02 \pm 4.33e-03 \pm 6.78e-03$	$1.95e-02 \pm 1.68e-03 \pm 2.54e-03$
1.06e+00	1.00e-01	$4.14e-02 \pm 3.20e-03 \pm 3.31e-03$	$1.82e-02 \pm 1.37e-03 \pm 1.45e-03$
1.16e+00	1.00e-01	$3.61e-02 \pm 2.82e-03 \pm 2.89e-03$	$1.22e-02 \pm 1.04e-03 \pm 9.73e-04$
1.31e+00	2.00e-01	$2.32e-02 \pm 1.50e-03 \pm 1.85e-03$	$7.64e-03 \pm 5.47e-04 \pm 6.11e-04$
1.50e+00	2.00e-01	$1.13e-02 \pm 9.51e-04 \pm 9.04e-04$	$3.51e-03 \pm 3.35e-04 \pm 2.81e-04$
1.70e+00	2.00e-01	$6.41e-03 \pm 6.63e-04 \pm 5.13e-04$	$2.21e-03 \pm 2.48e-04 \pm 1.77e-04$
1.90e+00	2.00e-01	$4.64e-03 \pm 5.37e-04 \pm 3.71e-04$	$9.80e-04 \pm 1.70e-04 \pm 7.84e-05$
2.25e+00	5.00e-01	$1.46e-03 \pm 1.78e-04 \pm 1.17e-04$	$5.66e-04 \pm 7.10e-05 \pm 4.53e-05$
2.75e+00	5.00e-01	$4.43e-04 \pm 1.38e-04 \pm 3.54e-05$	$1.29e-04 \pm 4.62e-05 \pm 1.03e-05$

Table A.17: \bar{p} spectra in 20-40% and 40-100% d+Au collisions. The unit of p_T and p_T width is GeV/c .

p_T	p_T width	p+p
4.68e-01	1.00e-01	$3.74e-02 \pm 2.60e-03 \pm 4.86e-03$
5.63e-01	1.00e-01	$2.84e-02 \pm 1.77e-03 \pm 3.70e-03$
6.61e-01	1.00e-01	$2.27e-02 \pm 1.38e-03 \pm 2.96e-03$
7.59e-01	1.00e-01	$1.32e-02 \pm 8.65e-04 \pm 1.71e-03$
8.58e-01	1.00e-01	$1.05e-02 \pm 7.20e-04 \pm 1.37e-03$
9.57e-01	1.00e-01	$7.17e-03 \pm 5.40e-04 \pm 9.32e-04$
1.06e+00	1.00e-01	$5.60e-03 \pm 3.77e-04 \pm 4.48e-04$
1.16e+00	1.00e-01	$3.74e-03 \pm 2.86e-04 \pm 2.99e-04$
1.31e+00	2.00e-01	$2.31e-03 \pm 1.49e-04 \pm 1.84e-04$
1.50e+00	2.00e-01	$9.69e-04 \pm 8.84e-05 \pm 7.75e-05$
1.70e+00	2.00e-01	$5.95e-04 \pm 6.65e-05 \pm 4.76e-05$
1.90e+00	2.00e-01	$3.57e-04 \pm 4.79e-05 \pm 2.86e-05$
2.25e+00	5.00e-01	$1.12e-04 \pm 1.90e-05 \pm 8.93e-06$
2.75e+00	5.00e-01	$3.87e-05 \pm 1.07e-05 \pm 3.10e-06$

Table A.18: \bar{p} spectra in p+p collisions. The unit of p_T and p_T width is GeV/c .

Appendix B

How to make MRPC

This appendix is based on the procedure of the MRPC production in USTC. I will introduce the material preparations and then the chamber installation.

B.1 Preparations

B.1.1 Glass

(1) Check the glass very carefully by eye. The glass with scrapes is not accepted. (2) Measure the size of the glass with the digital vernier caliper. The errors of the length and width are required to be within 0.1 mm. Measure the thickness in several different places. The precision of the thickness is required to be 0.01 mm for each glass. (3) Use the micrometer to measure the flatness, which is required to be less than 0.01 mm. Use the mirror and observe the stripes of interference. (4) Grind the edge and the corner of the glass, and clean it. The size of outer glass is $78(\text{width}) \times 206(\text{length}) \times 1.1(\text{height}) \text{ mm}^3$ and the size of inner glass is $61 \times 200 \times 0.54 \text{ mm}^3$.

B.1.2 Graphite Layer

(1) Stick the layer in the middle of the outer glass. Squeeze the air out. (2) Stick a small copper tape, which is for high voltage (HV) applying, on to the graphite layer,

which is in the middle of the long side, and 0~0.5 mm away from the edge of the glass. The size of the graphite layer is $74 \times 202 \text{ mm}^2$. The size of the copper tape (the rectangle with the round angle) is $6 \times 10 \text{ mm}^2$.

B.1.3 Mylar layer

Cut the mylar layer, and see if there is any tiny holes or scrapes. If yes, don't use it. The size of mylar is $84 \times 212 \times 0.35 \text{ mm}^3$.

B.1.4 Honeycomb board

Measure the size and flatness. The error of the length and width is required to be within 0.2 mm, the error of the thickness is required to be within 0.05 mm. The flatness is required to be within 0.1 mm. The size of honeycomb board is $84 \times 208 \times 4 \text{ mm}^3$.

B.1.5 The printed circuit board (PCB)

(1) Check the surface of the metal which is used as read-out strips carefully, and see the position of the HV-holes is right or not. Check the size of the metal holes, whose diameters are required to be larger than 0.9 mm. (2) Use double side tape to stick the PCB board with the Mylar. The size of the double side tape is the same as the PCB board. The length of the mylar is 1 mm longer than that of the PCB board. (3) Use sealing ion to open a ϕ 3 mm hole, the center of the hole is in the middle of the HV holes. The size of PCB is $94 \times 210 \times 1.5 \text{ mm}^3$. The size of metal holes are ϕ 1 mm.

B.1.6 Lucite cylinder

Use digital vernier caliper to measure the length of the Lucite cylinder. Clean it and stick a double side tape on one side. The size is ϕ 3 mm and $3.87 < \text{length} < 3.93$ mm.

B.1.7 Other stuff

Besides, we also need pins, fish line and little plastic cannula. The size of the pin is 2-2.1 cm long. The fish line is ϕ 0.22 mm. The plastic cannula is ϕ 1 mm. One kind of the cannula is 7 mm long, and the other is 5.6 mm long. Table B.1 lists the main materials for 1 MRPC.

B.2 Installation

B.2.1 The outer glass and mylar and PCB

(1) stick the outer glass on to the center of the mylar. (2) Use the sealing ion to connect the HV conductive line with the copper tape. Apply the HV to measure the noise rate and dark current. (3) Between the mylar and outer glass edge, on each side, use silica gel to seal. Attention: keep the surface clean and smooth. Attention: If one side is done, wait till the silica gel becomes solid. (4) Stick pins. Seal the pins which are used for the fish line coiling, into the metal holes of the PCB board. (5) Use the inner glass to fix on the position of Lucite cylinders, and keep them away from the pins for fish line. Then stick the 8~10 Lucite cylinders onto the outer glass.

B.2.2 Inner glass and fish-line coiling

(1) Pre-install. Don't use fish-line. Pay attention to adjust the position of the pins. (2) This is now the real installation and fish line coiling. Clean the outer glass and inner glass carefully, coil a loop of fish line, add a piece of glass, then coil another loop of fish line, add another piece of glass, and so on and so forth. Attention: clean the fish line before it coils, and blow the surface of glass to protect it from the dirt with nitrogen jet. (3) Another time for pre-installation. Pay attention to the position of the upper and lower electrodes and adjust the position of pins. (4) Paste 3140 RTV coating onto the surface of Lucite cylinders. (5) Connect the two electrodes. Make sure all the pins connect right into the metal holes. Then lay the whole flat, and put on a block which is 4 kilogram weight. (6) After 2 hours, stick the honeycomb. (7)

material	type	character	number	source
outer glass	window glass	1.1 mm thick, VR: 8.7×10^{12} ohm.cm	2	Shanghai
inner glass	window glass	0.54 mm thick, VR: 8.5×10^{12} ohm.cm	5	USA
graphite layer	T9149	0.13 mm thick, SR : 2M ohm/square	2	Japan
Mylar	M0	0.35 mm thick	2	Dupont Corp.
honeycomb		4 mm thick	2	Shanghai
PCB	gold	1.58 mm thick	2	Shenzhen
copper tape		0.08 mm thick	2	3M Comp.
LC	Lucite	ϕ 3 mm, 3.9 mm long	8-10	processing
pins (single)	metal pin	21.5 mm long	14	
pins (pair)	metal pin	21.5 mm long	12	
cannula	F-plastic	ϕ 1.4 mm	38	
fish line	top line	ϕ 0.22 mm		Switzerland
DST	9690	0.13 mm thick		3M Comp.
silica gel	CAF4	high-voltage insulation		Switzerland

Table B.1: The material for 1 MRPC model. VR is the volume resistivity and SR is the surface resistivity. LC is the Lucite cylinder. DST is the double side tape.

Measure the thickness of the whole. Make sure the precision is within 0.05 mm. (8)
Connect the conductive-line for the read-out strips, and then put the whole into a bag. Attention: the conductive-line should not be broken.

Appendix C

List of Publications

1. *Pion, kaon, proton and anti-proton transverse momentum distributions from $p+p$ and $d+Au$ collisions at $\sqrt{s_{NN}} = 200$ GeV*, STAR Collaboration, e-Print Archives (nu-ex/0309012), submitted.
2. *Open Charm Yields in 200 GeV $p+p$ and $d+Au$ Collisions at RHIC*, Lijuan Ruan (for the STAR Collaboration), Journal of Physics G, 30 (2004) S1197-S1200, contributed to 17th International Conference on Ultra Relativistic Nucleus-Nucleus Collisions (Quark Matter 2004).
3. *A Monte Carlo Simulation of Multi-gap Resistive Plate Chamber and comparison with Experimental Results*, RUAN Li-Juan, SHAO Ming, CHEN Hong-Fang, *et al.*, HEP and NP, Vol. 27, No. 8 (2003) 712-715.
4. *Monte Carlo Study of the Property of Multi-gap Resistive Plate Chambers*, Shao Ming, Ruan Lijuan, Chen Hongfang, *et al.*, HEP and NP, Vol. 27, No. 1 (2003) 67-71, (in Chinese).
5. *Study on Light Collection and its Uniformity of Long Lead Tungstate crystal by Monte Carlo Method*, Ruan Lijuan, Shao Ming, Xu Tong, *et al.*, Chinese Journal of Computational Physics, Vol. 19, No. 5 (2002) 453-458, (in Chinese).
6. *Beam test results of two kinds of multi-gap resistive plate chambers*, M. Shao, L. J. Ruan, H. F. Chen, J. Wu, , C. Li, Z. Z. Xu, X. L. Wang, S.L. Huang, Z. M. Wang and Z. P. Zhang, Nucl. Instr. and Meth. A 492 (2002) 344-350.
7. *The Study of the Resistive Property of the Electrode Material of MRPC*, Ruan

Lijuan, Wang Xiaolian, Li Cheng , *et al.*, to be published in Journal of University of Science and Technology of China (in Chinese).

8. *The Calibration Method of TOFr in the STAR Experiment*, RUAN Lijuan, WU Jian, DONG Xin , *et al.*, to be published in HEP and NP (in Chinese).

9. *Spectra of π K p K^* ϕ from Au+Au Collisions at 62.4 GeV*, Lijuan Ruan (for the STAR Collaboration), to be published in Journal of Physics G, Contributed to 8th International Conference on Strangeness in Quark Matter (SQM 2004).

10. *Pseudorapidity Asymmetry and Centrality Dependence of Charged Hadron Spectra in d+Au Collisions at $\sqrt{s_{NN}} = 200$ GeV*, STAR Collaboration: e-Print Archives (nu-ex/0408016), submitted.

11. *Transverse momentum correlations and minijet dissipation in Au-Au collisions at $\sqrt{s_{NN}} = 130$ GeV*, STAR Collaboration, e-Print Archives (nu-ex/0408012), submitted.

12. *Azimuthal anisotropy and correlations at large transverse momenta in p+p and Au+Au collisions at $\sqrt{s_{NN}} = 200$ GeV*, STAR Collaboration, e-Print Archives (nu-ex/0407007), submitted.

13. *Open charm yields in d+Au collisions at $\sqrt{s_{NN}} = 200$ GeV*, STAR Collaboration, e-Print Archives (nu-ex/0407006), submitted.

14. *Measurements of transverse energy distributions in Au+Au collisions at $\sqrt{s_{NN}} = 200$ GeV*, STAR Collaboration, e-Print Archives (nu-ex/0407003), submitted.

15. *Transverse-momentum dependent modification of dynamic texture in central Au+Au collisions at $\sqrt{s_{NN}} = 200$ GeV*, STAR Collaboration, e-Print Archives (nu-ex/0407001), submitted.

16. *Hadronization geometry and charge-dependent number autocorrelations on axial momentum space in Au-Au collisions at $\sqrt{s_{NN}} = 130$ GeV*, STAR Collaboration, e-Print Archives(nu-ex/0406035), submitted.

17. *Phi meson production in Au+Au and p+p collisions at $\sqrt{s}=200$ GeV*, STAR Collaboration, e-Print Archives (nu-ex/0406003), submitted.

18. *Centrality and pseudorapidity dependence of charged hadron production at intermediate p_T in Au+Au collisions at $\sqrt{s_{NN}} = 130$ GeV*, STAR Collaboration, e-Print Archives (nu-ex/0404020), to be published in Physical Review C.

19. *Production of $e+e-$ Pairs Accompanied by Nuclear Dissociation in Ultra-Peripheral Heavy Ion Collision*, STAR Collaboration, e-Print Archives (nu-ex/0404012), to be published in Physical Review C.
20. *Photon and neutral pion production in Au+Au collisions at $\sqrt{s_{NN}} = 130$ GeV*, STAR Collaboration, e-Print Archives (nu-ex/0401008), to be published in Physical Review C.
21. *Azimuthally sensitive HBT in Au+Au collisions at $\sqrt{s_{NN}} = 200$ GeV*, STAR Collaboration, Phys. Rev. Lett. 93, 012301 (2004).
22. *Production of Charged Pions and Hadrons in Au+Au Collisions at $\sqrt{s_{NN}}=130$ GeV*, STAR Collaboration, e-Print Archives (nu-ex/0311017), submitted.
23. *Azimuthal anisotropy at RHIC: the first and fourth harmonics*, STAR Collaboration, Phys. Rev. Lett. 92, 062301 (2004).
24. *Cross Sections and Transverse Single-Spin Asymmetries in Forward Neutral Pion Production from Proton Collisions at $\sqrt{s} = 200$ GeV*, STAR Collaboration, Phys. Rev. Lett. 92, 171801 (2004).
25. *Identified particle distributions in pp and Au+Au collisions at $\sqrt{s_{NN}}=200$ GeV*, STAR Collaboration, Phys. Rev. Lett. 92, 112301 (2004).
26. *Event-by-Event (pt) fluctuations in Au-Au collisions at $\sqrt{s_{NN}} = 130$ GeV*, STAR Collaboration, e-Print Archives (nu-ex/0308033), submitted.
27. *Multi-strange baryon production in Au-Au collisions at $\sqrt{s_{NN}} = 130$ GeV*, STAR Collaboration, Phys. Rev. Lett. 92, 182301 (2004).
28. *Pion-Kaon Correlations in Central Au+Au Collisions at $\sqrt{s_{NN}} = 130$ GeV*, STAR Collaboration, Phys. Rev. Lett. 91, 262302 (2003).
29. *ρ -0 Production and Possible Modification in Au+Au and p+p Collisions at $\sqrt{s_{NN}} = 200$ GeV*, STAR Collaboration, Phys. Rev. Lett. 92, 092301 (2004).
30. *Net charge fluctuations in Au+Au collisions at $\sqrt{s_{NN}} = 130$ GeV*, STAR Collaboration, Phys. Rev. C 68, 044905 (2003).
31. *Rapidity and Centrality Dependence of Proton and Anti-proton Production from Au+Au Collisions at $\sqrt{s_{NN}} = 130$ GeV*, STAR Collaboration, e-Print Archives (nu-ex/0306029), submitted.

32. *Three-Pion Hanbury Brown-Twiss Correlations in Relativistic Heavy-Ion Collisions from the STAR Experiment*, STAR Collaboration, Phys. Rev. Lett. 91, 262301 (2003).
33. *Evidence from d+Au measurements for final-state suppression of high pT hadrons in Au+Au collisions at RHIC*, STAR Collaboration, Phys. Rev. Lett. 91, 072304 (2003).
34. *Particle-type dependence of azimuthal anisotropy and nuclear modification of particle production in Au+Au collisions at $\sqrt{s_{NN}} = 200$ GeV*, STAR Collaboration, Phys. Rev. Lett. 92, 052302 (2004).
35. *Transverse momentum and collision energy dependence of high pT hadron suppression in Au+Au collisions at ultrarelativistic energies*, STAR Collaboration, Phys. Rev. Lett. 91, 172302 (2003).

Appendix D

STAR Collaboration

- J. Adams,³ M.M. Aggarwal,²⁹ Z. Ahammed,⁴³ J. Amonett,²⁰ B.D. Anderson,²⁰ D. Arkhipkin,¹³ G.S. Averichev,¹² S.K. Badyal,¹⁹ Y. Bai,²⁷ J. Balewski,¹⁷ O. Barannikova,³² L.S. Barnby,³ J. Baudot,¹⁸ S. Bekele,²⁸ V.V. Belaga,¹² R. Bellwied,⁴⁶ J. Berger,¹⁴ B.I. Bezverkhny,⁴⁸ S. Bharadwaj,³³ A. Bhasin,¹⁹ A.K. Bhati,²⁹ V.S. Bhatia,²⁹ H. Bichsel,⁴⁵ J. Bielcik,⁴⁸ J. Bielcikova,⁴⁸ A. Billmeier,⁴⁶ L.C. Bland,⁴ C.O. Blyth,³ B.E. Bonner,³⁴ M. Botje,²⁷ A. Boucham,³⁸ A.V. Brandin,²⁵ A. Bravar,⁴ M. Bystersky,¹¹ R.V. Cadman,¹ X.Z. Cai,³⁷ H. Caines,⁴⁸ M. Calderón de la Barca Sánchez,¹⁷ J. Castillo,²¹ O. Catu,⁴⁸ D. Cebra,⁷ Z. Chajecki,⁴⁴ P. Chaloupka,¹¹ S. Chattopadhyay,⁴³ H.F. Chen,³⁶ Y. Chen,⁸ J. Cheng,⁴¹ M. Cherney,¹⁰ A. Chikanian,⁴⁸ W. Christie,⁴ J.P. Coffin,¹⁸ T.M. Cormier,⁴⁶ J.G. Cramer,⁴⁵ H.J. Crawford,⁶ D. Das,⁴³ S. Das,⁴³ M.M. de Moura,³⁵ A.A. Derevschikov,³¹ L. Didenko,⁴ T. Dietel,¹⁴ S.M. Dogra,¹⁹ W.J. Dong,⁸ X. Dong,³⁶ J.E. Draper,⁷ F. Du,⁴⁸ A.K. Dubey,¹⁵ V.B. Dunin,¹² J.C. Dunlop,⁴ M.R. Dutta Mazumdar,⁴³ V. Eckardt,²³ W.R. Edwards,²¹ L.G. Efimov,¹² V. Emelianov,²⁵ J. Engelage,⁶ G. Eppley,³⁴ B. Erasmus,³⁸ M. Estienne,³⁸ P. Fachini,⁴ J. Faivre,¹⁸ R. Fatemi,¹⁷ J. Fedorisin,¹² K. Filimonov,²¹ P. Filip,¹¹ E. Finch,⁴⁸ V. Fine,⁴ Y. Fisyak,⁴ K. Fomenko,¹² J. Fu,⁴¹ C.A. Gagliardi,³⁹ L. Gaillard,³ J. Gans,⁴⁸ M.S. Ganti,⁴³ L. Gaudichet,³⁸ F. Geurts,³⁴ V. Ghazikhanian,⁸ P. Ghosh,⁴³ J.E. Gonzalez,⁸ O. Grachov,⁴⁶ O. Grebenyuk,²⁷ D. Grosnick,⁴² S.M. Guertin,⁸ Y. Guo,⁴⁶ A. Gupta,¹⁹ T.D. Gutierrez,⁷ T.J. Hallman,⁴ A. Hamed,⁴⁶ D. Hardtke,²¹ J.W. Harris,⁴⁸ M. Heinz,² T.W. Henry,³⁹ S. Hepplemann,³⁰ B. Hippolyte,¹⁸ A. Hirsch,³² E. Hjort,²¹ G.W. Hoffmann,⁴⁰ H.Z. Huang,⁸ S.L. Huang,³⁶ E.W. Hughes,⁵ T.J. Humanic,²⁸ G. Igo,⁸ A. Ishihara,⁴⁰ P. Jacobs,²¹ W.W. Jacobs,¹⁷ M. Janik,⁴⁴ H. Jiang,⁸ P.G. Jones,³ E.G. Judd,⁶ S. Kabana,² K. Kang,⁴¹ M. Kaplan,⁹ D. Keane,²⁰ V.Yu. Khodyrev,³¹ J. Kiryluk,²² A. Kisiel,⁴⁴ E.M. Kislov,¹² J. Klay,²¹ S.R. Klein,²¹ D.D. Koetke,⁴² T. Kollegger,¹⁴ M. Kopytine,²⁰ L. Kotchenda,²⁵ M. Kramer,²⁶ P. Kravtsov,²⁵ V.I. Kravtsov,³¹ K. Krueger,¹ C. Kuhn,¹⁸ A.I. Kulikov,¹² A. Kumar,²⁹ R.Kh. Kutuev,¹³ A.A. Kuznetsov,¹² M.A.C. Lamont,⁴⁸ J.M. Landgraf,⁴ S. Lange,¹⁴ F. Laue,⁴ J. Lauret,⁴ A. Lebedev,⁴ R. Lednicky,¹² S. Lehocka,¹² M.J. LeVine,⁴ C. Li,³⁶ Q. Li,⁴⁶ Y. Li,⁴¹ G. Lin,⁴⁸ S.J. Lindenbaum,²⁶ M.A. Lisa,²⁸ F. Liu,⁴⁷ L. Liu,⁴⁷ Q.J. Liu,⁴⁵ Z. Liu,⁴⁷ T. Ljubicic,⁴ W.J. Llope,³⁴ H. Long,⁸ R.S. Longacre,⁴ M. Lopez-Noriega,²⁸ W.A. Love,⁴ Y. Lu,⁴⁷ T. Ludlam,⁴ D. Lynn,⁴ G.L. Ma,³⁷ J.G. Ma,⁸ Y.G. Ma,³⁷ D. Magestro,²⁸ S. Mahajan,¹⁹ D.P. Mahapatra,¹⁵ R. Majka,⁴⁸ L.K. Mangotra,¹⁹ R. Manweiler,⁴² S. Margetis,²⁰ C. Markert,²⁰ L. Martin,³⁸ J.N. Marx,²¹ H.S. Matis,²¹ Yu.A. Matulenko,³¹ C.J. McClain,¹ T.S. McShane,¹⁰ F. Meissner,²¹ Yu. Melnick,³¹ A. Meschanin,³¹ M.L. Miller,²² N.G. Minaev,³¹ C. Mironov,²⁰ A. Mischke,²⁷ D.K. Mishra,¹⁵ J. Mitchell,³⁴ B. Mohanty,⁴³ L. Molnar,³² C.F. Moore,⁴⁰ D.A. Morozov,³¹ M.G. Munhoz,³⁵ B.K. Nandi,⁴³ S.K. Nayak,¹⁹ T.K. Nayak,⁴³ J.M. Nelson,³ P.K. Netrakanti,⁴³ V.A. Nikitin,¹³ L.V. Nogach,³¹ S.B. Nurushev,³¹ G. Odyniec,²¹ A. Ogawa,⁴ V. Okorokov,²⁵ M. Oldenburg,²¹ D. Olson,²¹ S.K. Pal,⁴³ Y. Panebratsev,¹² S.Y. Panitkin,⁴ A.I. Pavlinov,⁴⁶ T. Pawlak,⁴⁴ T. Peitzmann,²⁷ V. Perevoztchikov,⁴ C. Perkins,⁶ W. Peryt,⁴⁴ V.A. Petrov,¹³ S.C. Phatak,¹⁵ R. Picha,⁷ M. Planinic,⁴⁹ J. Pluta,⁴⁴ N. Porile,³² J. Porter,⁴⁵ A.M. Poskanzer,²¹ M. Potekhin,⁴ E. Potrebenikova,¹² B.V.K.S. Potukuchi,¹⁹ D. Prindle,⁴⁵ C. Pruneau,⁴⁶ J. Putschke,²³ G. Rakness,³⁰ R. Raniwala,³³ S. Raniwala,³³ O. Ravel,³⁸ R.L. Ray,⁴⁰ S.V. Razin,¹² D. Reichhold,³² J.G. Reid,⁴⁵ G. Renault,³⁸ F. Retiere,²¹ A. Ridiger,²⁵ H.G. Ritter,²¹ J.B. Roberts,³⁴ O.V. Rogachevskiy,¹² J.L. Romero,⁷ A. Rose,⁴⁶ C. Roy,³⁸ L. Ruan,³⁶ R. Sahoo,¹⁵ I. Sakrejda,²¹ S. Salur,⁴⁸ J. Sandweiss,⁴⁸ M. Sarsour,¹⁷ I. Savin,¹³ P.S. Sazhin,¹² J. Schambach,⁴⁰ R.P. Scharenberg,³² N. Schmitz,²³ K. Schweda,²¹ J. Seger,¹⁰ P. Seyboth,²³ E. Shahaliev,¹² M. Shao,³⁶ W. Shao,⁵ M. Sharma,²⁹ W.Q. Shen,³⁷ K.E. Shestermanov,³¹ S.S. Shimanskiy,¹² E. Sichtermann,²¹ F. Simon,²³ R.N. Singaraju,⁴³ G. Skoro,¹² N. Smirnov,⁴⁸ R. Snellings,²⁷ G. Sood,⁴² P. Sorensen,²¹ J. Sowinski,¹⁷ J. Speltz,¹⁸ H.M. Spinka,¹ B. Srivastava,³² A. Stadnik,¹² T.D.S. Stanislaus,⁴² R. Stock,¹⁴ A. Stolpovsky,⁴⁶ M. Strikhanov,²⁵ B. Stringfellow,³² A.A.P. Suaide,³⁵ E. Sugarbaker,²⁸ C. Suire,⁴ M. Sumbera,¹¹ B. Surrow,²² T.J.M. Symons,²¹ A. Szanto de Toledo,³⁵ P. Szarwas,⁴⁴ A. Tai,⁸ J. Takahashi,³⁵ A.H. Tang,²⁷ T. Tarnowsky,³² D. Thein,⁸ J.H. Thomas,²¹ S. Timoshenko,²⁵ M. Tokarev,¹² T.A. Trainor,⁴⁵ S. Trentalange,⁸ R.E. Tribble,³⁹ O.D. Tsai,⁸ J. Ulery,³² T. Ullrich,⁴ D.G. Underwood,¹ A. Urkinbaev,¹² G. Van Buren,⁴ M. van Leeuwen,²¹ A.M. Vander Molen,²⁴ R. Varma,¹⁶ I.M. Vasilevski,¹³ A.N. Vasiliev,³¹ R. Vernet,¹⁸ S.E. Vigdor,¹⁷ Y.P. Viyogi,⁴³ S. Vokal,¹² S.A. Voloshin,⁴⁶ M. Vznuzdaev,²⁵ W.T. Waggoner,¹⁰ F. Wang,³² G. Wang,²⁰ G. Wang,⁵ X.L. Wang,³⁶ Y. Wang,⁴⁰ Y. Wang,⁴¹ Z.M. Wang,³⁶ H. Ward,⁴⁰ J.W. Watson,²⁰ J.C. Webb,¹⁷ R. Wells,²⁸ G.D. Westfall,²⁴ A. Wetzler,²¹ C. Whitten Jr.,⁸ H. Wieman,²¹ S.W. Wissink,¹⁷ R. Witt,² J. Wood,⁸ J. Wu,³⁶ N. Xu,²¹ Z. Xu,⁴ Z.Z. Xu,³⁶ E. Yamamoto,²¹ P. Yepes,³⁴ V.I. Yurevich,¹² Y.V. Zanevsky,¹² H. Zhang,⁴ W.M. Zhang,²⁰ Z.P. Zhang,³⁶ R. Zoulkarneeva,¹³ and A.N. Zubarev¹²

¹Argonne National Laboratory, Argonne, Illinois 60439²University of Bern, 3012 Bern, Switzerland

- ³University of Birmingham, Birmingham, United Kingdom
- ⁴Brookhaven National Laboratory, Upton, New York 11973
- ⁵California Institute of Technology, Pasadena, California 91125
- ⁶University of California, Berkeley, California 94720
- ⁷University of California, Davis, California 95616
- ⁸University of California, Los Angeles, California 90095
- ⁹Carnegie Mellon University, Pittsburgh, Pennsylvania 15213
- ¹⁰Creighton University, Omaha, Nebraska 68178
- ¹¹Nuclear Physics Institute AS CR, 250 68 Řež/Prague, Czech Republic
- ¹²Laboratory for High Energy (JINR), Dubna, Russia
- ¹³Particle Physics Laboratory (JINR), Dubna, Russia
- ¹⁴University of Frankfurt, Frankfurt, Germany
- ¹⁵Institute of Physics, Bhubaneswar 751005, India
- ¹⁶Indian Institute of Technology, Mumbai, India
- ¹⁷Indiana University, Bloomington, Indiana 47408
- ¹⁸Institut de Recherches Subatomiques, Strasbourg, France
- ¹⁹University of Jammu, Jammu 180001, India
- ²⁰Kent State University, Kent, Ohio 44242
- ²¹Lawrence Berkeley National Laboratory, Berkeley, California 94720
- ²²Massachusetts Institute of Technology, Cambridge, MA 02139-4307
- ²³Max-Planck-Institut für Physik, Munich, Germany
- ²⁴Michigan State University, East Lansing, Michigan 48824
- ²⁵Moscow Engineering Physics Institute, Moscow Russia
- ²⁶City College of New York, New York City, New York 10031
- ²⁷NIKHEF, Amsterdam, The Netherlands
- ²⁸Ohio State University, Columbus, Ohio 43210
- ²⁹Panjab University, Chandigarh 160014, India
- ³⁰Pennsylvania State University, University Park, Pennsylvania 16802
- ³¹Institute of High Energy Physics, Protvino, Russia
- ³²Purdue University, West Lafayette, Indiana 47907
- ³³University of Rajasthan, Jaipur 302004, India
- ³⁴Rice University, Houston, Texas 77251
- ³⁵Universidade de Sao Paulo, Sao Paulo, Brazil
- ³⁶University of Science & Technology of China, Anhui 230027, China
- ³⁷Shanghai Institute of Applied Physics, Shanghai 201800, China
- ³⁸SUBATECH, Nantes, France
- ³⁹Texas A&M University, College Station, Texas 77843
- ⁴⁰University of Texas, Austin, Texas 78712
- ⁴¹Tsinghua University, Beijing 100084, China
- ⁴²Valparaiso University, Valparaiso, Indiana 46383
- ⁴³Variable Energy Cyclotron Centre, Kolkata 700064, India
- ⁴⁴Warsaw University of Technology, Warsaw, Poland
- ⁴⁵University of Washington, Seattle, Washington 98195
- ⁴⁶Wayne State University, Detroit, Michigan 48201
- ⁴⁷Institute of Particle Physics, CCNU (HZNU), Wuhan 430079, China
- ⁴⁸Yale University, New Haven, Connecticut 06520
- ⁴⁹University of Zagreb, Zagreb, HR-10002, Croatia

Bibliography

- [1] Cheuk-Yin Wong, Introduction to the High-Energy Heavy-Ion Collisions.
- [2] J. Harris, three lectures given at the Lake Louise Winter Institute on Quantum Chromodynamics, 15-21 February, 1998, Lake Louise, Alberta, Canada, pulished in World Scientific, 1998.
- [3] P. Braun-Munzinger, Nucl. Phys. A **681** 119-123 (2001).
- [4] Z. Fodor and S. D. Katz, JHEP 0404 (2004) 050, hep-lat/0402006; G. I. Egri, Z. Fodor, S. D. Katz, K. K. Szabo and A. I. Toth, Prog. Theor. Phys. Suppl. 153 (2004) 93-105, hep-lat/0401022; M. Gyulassy, Journal of Physics G, 30 (2004) S911-S918, contributed to 17th International Conference on Ultra Relativistic Nucleus-Nucleus Collisions (Quark Matter 2004), nucl-th/0403032.
- [5] P. Huovinen, P.F. Kolb, U. Heinz, P. V. Ruuskanen, and S. A. Voloshin, Phys. Lett. B **503**, 58(2001).
- [6] STAR Collaboration, J. Adams *et al.*, Phys. Rev. Lett. **92**, 052302 (2004).
- [7] STAR Collaboration, J. Adams *et al.*, Phys. Rev. Lett. **92**, 062301 (2004).
- [8] STAR Collaboration, J. Adams *et al.*, Phys. Rev. Lett. **91**, 172302 (2003).
- [9] M. Gyulassy *et al.*, Review for: Quark Gluon Plasma 3, Editors: R.C. Hwa and X.N. Wang, World Scientific, Singapore, nucl-th/0302077; X.N. Wang, Phys. Rev. C **61**, 064910 (2000).

- [10] A.H. Tang (for the STAR Collaboration), Journal of Physics G, 30 (2004) S1235-S1238, contributed to 17th International Conference on Ultra Relativistic Nucleus-Nucleus Collisions (Quark Matter 2004).
- [11] F. Wang (for the STAR Collaboration), Journal of Physics G, 30 (2004) S1299-S1304, contributed to 17th International Conference on Ultra Relativistic Nucleus-Nucleus Collisions (Quark Matter 2004).
- [12] K. Schweda (for the STAR Collaboration), Journal of Physics G, 30 (2004) S693-S700, contributed to 17th International Conference on Ultra Relativistic Nucleus-Nucleus Collisions (Quark Matter 2004).
- [13] STAR White Paper, nucl-ex/0501009, submitted to Nucl. Phys. A.
- [14] PHENIX Collaboration, S.S. Adler *et al.*, Phys. Rev. C **69**, 034909 (2004);
- [15] B. Alper *et al.*, Nucl. Phys. B **100**, 237 (1975).
- [16] DELPHI Collaboration, P. Abreu *et al.* Eur. Phys. J. **C17**, 207 (2000).
- [17] PHENIX Collaboration, S.S. Adler *et al.*, Phys. Rev. Lett. **91**, 072301 (2003);
PHENIX collaboration, S.S. Adler *et al.*, Phys. Rev. Lett. **91**, 241803 (2003).
- [18] PHENIX Collaboration, K. Adcox *et al.*, Phys. Lett. B **561**, 82 (2003); PHENIX
Collaboration, S.S. Adler *et al.*, Phys. Rev. Lett. **91**, 172301 (2003).
- [19] D. Teaney *et al.*, nucl-th/0110037; D. Teaney *et al.*, Phys. Rev. Lett. **86**, 4783 (2001).
- [20] P. Huovinen, Nucl. Phys. A **715**, 299c (2003).
- [21] R.C. Hwa *et al.*, Phys. Rev. C **67**, 034902 (2003).
- [22] R.J. Fries *et al.*, Phys. Rev. C **68**, 044902 (2003).
- [23] V. Greco *et al.*, Phys. Rev. Lett. **90**, 202302 (2003).
- [24] I. Vitev and M. Gyulassy, Phys. Rev. C **65**, 041902 (2002).

- [25] K.P. Das and R.C. Hwa, Phys. Lett. B **68**, 459 (1977); Erratum ibid. **73**, 504 (1978); R.G. Roberts, R.C. Hwa and S. Matsuda, J. Phys. G **5**, 1043 (1979).
- [26] C. Gupt *et al.*, Nuovo Cimento **75**, 408 (1983); T. Tchiai, Prog. Theor. Phys **75**, 1184 (1986); T.S. Biro *et al.*, Phys. Lett. B **347**, 6 (1995); T.S. Biro *et al.*, J. Phys. G **28**, 1561 (2002).
- [27] B. Müller, nucl-th/0404015.
- [28] J.W. Cronin *et al.*, Phys. Rev. Lett. **31**, 1426 (1973); J.W. Cronin *et al.*, Phys. Rev. D **11**, 3105 (1975); D. Antreasyan *et al.*, Phys. Rev. D **19**, 764 (1979); P.B. Straub *et al.*, Phys. Rev. Lett. **68**, 452 (1992).
- [29] M. Lev and B. Petersson, Z. Phys. C **21**, 155(1983).
- [30] A. Accardi, Contribution to the CERN Yellow report on Hard Probes in Heavy Ion Collisions at the LHC, hep-ph/0212148, (2002); X.N. Wang, Phys. Rev. C **61**, 064910 (2000).
- [31] I. Vitev, Phys. Lett. B **562**, 36 (2003).
- [32] T. Alexopoulos *et al.*, Phys. Lett. B **435**, 453 (1998).
- [33] D. Kharzeev *et al.*, Phys. Lett. B **561**, 93 (2003); J. Jalilian-Marian *et al.*, Phys. Lett. B **577**, 54 (2003); J.L. Albacete *et al.*, Phys. Rev. Lett. **92**, 082001 (2004); D. Kharzeev *et al.*, Phys. Rev. D **68**, 094013 (2003); R. Baier *et al.*, Phys. Rev. D **68**, 054009 (2003).
- [34] E. Schnedermann, J. Sollfrank, and U. Heinz, Phys. Rev. C **48**, 2462 (1993).
- [35] STAR Collaboration, J. Adams *et al.*, Phys. Rev. Lett. **92**, 112301 (2004).
- [36] STAR Collaboration, J. Adams *et al.*, Phys. Rev. Lett. **91**, 072304 (2003).
- [37] PHENIX Collaboration, S.S. Adler *et al.*, Phys. Rev. Lett. **91**, 072303 (2003); PHOBOS Collaboration, B.B. Back *et al.*, Phys. Rev. Lett. **91**, 072302 (2003); BRAHMS Collaboration, I. Arsene *et al.*, Phys. Rev. Lett. **91**, 072305 (2003).

- [38] M. Anderson *et al.*, Nucl. Instr. Meth. A **499**, 659 (2003).
- [39] B. Bonner *et al.*, Nucl. Instr. Meth. A **508**, 181 (2003); M. Shao *et al.*, Nucl. Instr. Meth. A **492**, 344 (2002).
- [40] P. Sorenson, Ph.D. thesis, UCLA, 2003.
- [41] <http://www.rhic.bnl.gov/>.
- [42] T. Roser, Nuclear Physics A 688, 23c-28c, 2002.
- [43] J. Harris *et al.*, Nucl. Instrum. Meth. A **499**, 624 (2003).
- [44] ‘Conceptual Design Report for the Solenoidal Tracker At RHIC’, The STAR Collaboration, PUB-5347 (1992); J.W. Harris *et al.*, Nucl. Phys. A 566, 277c (1994).
- [45] R.L. Brown *et al.*, Proc. 1997 IEEE Particle Accelerator Conf., 3230 (1998)
and F. Bergsma *et al.*, ‘The STAR Detector Magnet Subsystem’, Nucl. Instrum. Meth. A499, 629 (2003).
- [46] D. Lynn *et al.*, Nucl. Instrum. Meth. A447, 264 (2000)
and R. Bellwied *et al.*, ‘The STAR Silicon Vertex Tracker’, Nucl. Instrum. Meth. A499, 636 (2003).
- [47] L. Arnold *et al.*, ‘The STAR Silicon Strip Detector’, Nucl. Instrum. Meth. A499, 648 (2003).
- [48] H. Wieman *et al.*, IEEE Trans. Nucl. Sci. 44, 671 (1997).
- [49] S. Klein *et al.*, IEEE Trans. Nucl. Sci. 43, 1768 (1996)
and M. Anderson *et al.*, ‘A Readout System for the STAR Time Projection Chamber’, Nucl. Instrum. Meth. A499, 675 (2003).
- [50] A. Schuttauf *et al.*, Nuc. Phys. A661, 677c (1999)
and K.H. Ackerman *et al.*, ‘The Forward Time Projection Chamber in STAR’, Nucl. Instrum. Meth. A499, 709 (2003).

- [51] ‘A Ring Imaging Cherenkov Detector for STAR’, STARnote 349, STAR/ALICE RICH Collaboration (1998); ALICE Collaboration, Technical Design and Report, Detector for High Momentum PID, CERN/LHCC 98-19.
- [52] M. Beddo et al., ‘The STAR Barrell Electromagnetic Calorimeter’, Nucl. Instrum. Meth. A499, 721 (2003).
- [53] C.E. Allgower et al., ‘The STAR Endcap Electromagnetic Calorimeter’, Nucl. Instrum. Meth. A499, 736 (2003).
- [54] L. Kotchenda et al., “The STAR TPC Gas System”, Nucl. Instrum. Meth. A499 (2003).
- [55] STAR software for the event reconstruction.
- [56] E. Cerron Zeballos *et al.*, Nucl. Instr. Meth. A **374**, 132 (1996); M.C.S. Williams *et al.*, Nucl. Instr. Meth. A **478**, 183 (2002).
- [57] R. Santonico, R.Cardarelli, Nucl. Instr. And Meth. 187 (1981) 377-380.
- [58] E. Cerron Zeballos, I. Cotty, D. Hatzifotiadou, J.Lamas Valverde, S. Neupane, M.C.S. Williams and A. Zichichi, Nucl. Instr. Meth. A374(1996) 132.
- [59] M. Abbrescia et al., Nucl. Instr. and Meth. A 398 (1997) 173-179.
- [60] M. Abbrescia et al., Nucl. Instr. and Meth. A 409 (1998) 1-5.
- [61] M. Abbrescia et al., Nucl. Instr. and Meth. A 431 (1999) 413-427.
- [62] SHAO Ming, RUAN Lijuan, CHEN Hongfang, et al., HEP and NP, Vol. 27, No. 1 (2003) 67-71, (in Chinese); RUAN Li-Juan, SHAO Ming, CHEN Hong-Fang, et al., HEP and NP, Vol. 27, No. 8 (2003) 712-715.
- [63] H. Genz, Nucl. Instr. and Meth. 112 (1973) 83-90.
- [64] E. Gatti et al., Nucl. Instr. and Meth. 193 (1982) 651.

- [65] I. Smimov, HEED, Program to Compute Energy Loss of Fast Particles in Gases, Version 1.01 CERN W5060.
- [66] S. Biagi, Nucl. Instr. and Meth. A283 (1989) 716.
- [67] S. Biagi, Nucl. Instr. and Meth. A421 (1999) 234-240.
- [68] P. Camarri, R. Cardarelli, A. Di Ciaccio, R.Santonico, Nucl. Instr. and Meth. A414 (1998) 317-324.
- [69] LI Cheng, CHEN Hongfang, SHAO Ming, et al., HEP and NP, 2002, 26 (5):455-461 (in Chinese).
- [70] LI Cheng, WU Jian, CHEN Hong-Fang, et al., HEP and NP, 2001,25(9): 933-936) (in English).
- [71] CHEN Hongfang, LI Cheng, WANG Xiaolian, et al., HEP and NP, 2002, 26(3):201-206(in Chinese).
- [72] LI Cheng, WU Jian, Wang Xiaolian, et al., Nuclear Science and Techniques, 2002, Vol.13, No.1: 6-10(in English).
- [73] W.J. Llope *et al.*, Nucl. Instr. Meth. A **522**, 252 (2004).
- [74] STAR Collaboration, “proposal for a large area time of flight system for STAR”.
- [75] Ruan Lijuan *et al.*, “The Study of the Resistive Property of the Electrode Material of MRPC”, to be published in Journal of University of Science and Technology of China (in Chinese).
- [76] T. Sjöstrand, P. Eden, C. Friberg *et al.*, Comput. Phys. Commun. **135**, 238 (2001).
- [77] X.N. Wang and M. Gyulassy, Phys. Rev. D **44**, 3501 (1991).
- [78] K.H. Ackermann *et al.*, Nucl. Instr. Meth. A **499**, 713 (2003).
- [79] STAR Collaboration, C. Adler *et al.*, Phys. Rev. Lett. **87**, 262302 (2001).

- [80] T. Alexopoulos *et al.*, Phys. Rev. D **48**, 984 (1993).
- [81] H. Zhang, Ph.D. thesis, Yale University, 2003.
- [82] H. Long, Ph.D. thesis, UCLA, 2002.
- [83] A. Tang, Ph.D. thesis, Kent University, 2001.
- [84] CERN RD44 Project at <http://wwwinfo.cern.ch/asd/geant/geant4public/G4UsersDocuments/Welcome/IntroductionToGeant4/html/introductionToGeant4.html>.
- [85] P. Nevski, <http://www.star.bnl.gov/STARAFS/comp/simu/gstar/gstar.html>.
- [86] Particle Data Group, Phys. Rev. D **45** (1992).
- [87] X.N. Wang, Phys. Lett. B **565**, 116 (2003).
- [88] X.N. Wang, Private Conversation (2004).
- [89] J.W. Qiu, Private Conversation (2004).
- [90] STAR Collaboration, J. Adams *et al.*, Phys. Rev. C **70**, 064907 (2004).
- [91] J. W. Qiu and I. Vitev, Phys. Rev. Lett. **93**, 262301 (2004); J. W. Qiu and I. Vitev, hep-ph/0405068.
- [92] R.C. Hwa and C.B. Yang, Phys. Rev. Lett. **93**, 082302 (2004); R.C. Hwa and C.B. Yang, Phys. Rev. C **70**, 037901 (2004).
- [93] C.B. Yang, Private Communication (2004).
- [94] Z. Xu, Presentation inside STAR (2004).
- [95] P.L. McGaughey, J.M. Moss, and J.C. Peng, hep-ph/9905409; D.M. Alde, *et al.*, Phys. Rev. Lett. **64**, 2479 (1990).
- [96] ARGUS Collaboration, H. Albrecht *et al.*, Z. Phys. C - Particles and Fields **44**, 547-555 (1989).

- [97] L.J. Ruan, Presentation inside STAR (2004); X.Z. Cai (for the STAR Collaboration), in Proceedings of SQM2004.
- [98] STAR Collaboration, J. Adams *et al.*, nucl-ex/0309012.
- [99] STAR Collaboration, J. Adams *et al.*, Phys. Rev. Lett. **94**, 062301 (2005), nucl-ex/0407006; L. Ruan (for the STAR Collaboration), Journal of Physics G, 30 (2004) S1197-S1200, contributed to 17th International Conference on Ultra Relativistic Nucleus-Nucleus Collisions (Quark Matter 2004), nucl-ex/0403054.
- [100] P.L. McGaughey, *et al.*, Int. J. Mod. Phys., **A 10**, 2999 (1995).
- [101] Z. Lin and M. Gyulassy, Phys. Rev. Lett. **77**, 1222 (1996).
- [102] Y.L. Dokshitzer and D.E. Kharzeev, Phys. Lett. **B 519**, 199 (2001).
- [103] A. Andronic, P. Braun-Munzinger, *et al.*, Phys. Lett. **B 571**, 36 (2003); R.L. Thews, M. Schroedter, J. Rafelski, Phys. Rev. **C 63**, 054905 (2001); L. Grandchamp, R. Rapp, Nucl. Phys. **A 709**, 415 (2002), and references therein.